Super-resolved Optical Imaging, Reconstruction, and Spatial Analysis of Whole Mouse Glomeruli

Adilijiang Ali

A dissertation
submitted in partial fulfillment of the
requirements for the degree of

Doctor of Philosophy

University of Washington
2025

Reading Committee:
Joshua Charles Vaughan, Chair
Ashleigh Theberge
Robert Synovec

Program Authorized to Offer Degree:
Chemistry

University of Washington

Abstract

Super-resolved Optical Imaging, Reconstruction, and Spatial Analysis of Whole Mouse Glomeruli

Adilijiang Ali

Chair of the Supervisory Committee:

Joshua Charles Vaughan

Chemistry

The glomerulus plays a crucial role in blood filtration and is made up of several key components that function collaboratively. Traditionally, optical microscopy has provided insights into general physiology and molecular distributions, and electron microscopy has been used to reveal ultrastructural details of the glomerular structures. While past studies have extensively examined local changes in glomerular diseases and aging, the global relationships and coordination among glomerular structures remain poorly understood due to the limitations of two-dimensional and partial analyses. To address these limitations, I present a novel pipeline that

employs super-resolution fluorescence microscopy to achieve holistic three-dimensional imaging, reconstruction, and analysis of whole mouse glomeruli at 100 nm resolution. This workflow integrates advanced tissue labeling techniques and super-resolution imaging to capture entire mouse glomeruli, and combines manual segmentation with machine learning methods to reconstruct all glomerular compartments in 3D. I further demonstrate the versatility of this approach by applying it to various glomerular types, including cortical and juxtamedullary, as well as different conditions such as aging and focal segmental glomerulosclerosis. I also show that the detailed spatial analyses of the resulting models reveal new insights into the spatial correlations among glomerular components in both aged and diseased mice. Once published, the unique datasets generated by this approach will serve as a valuable resource for the nephrology community.

Table of Contents

List of Figures

List of Tables

List of Movies

Acknowledgments

First of all, I would like to thank my advisor, Prof. Joshua Vaughan, for his meticulous support throughout my time at the Vaughan lab. This thesis could not be completed without the support of Prof. Vaughan. Before joining the group, I was perplexed and didn't know what I could do due to my lack of scientific research experience. He welcomed me into the group and provided me with tremendous help starting from the first day. We had many inspiring and encouraging discussions every week, which slowly equipped me well with the skills and knowledge to become a rigorous researcher. He provided me with a lot of opportunities for both developing my skills and working as a qualified team member. Had it not been for the professor Vaughan's help, I would not have been admitted to the PhD degree in chemistry at UW and make it through. I would like to give a special thanks to our post-doc, Dr. Chetan Poudel, for helping me extensively throughout my thesis work here. He helped me get started to get with my work by providing valuable scientific knowledge and technical skills, which greatly impacted me in developing a scientific mindset. He was always so patient with me when I had questions and encountered problems. I would also like to thank all the other members of the Vaughan group, especially Ziyu Guo and Madeline Wong for being supportive not only as coworkers but also close friends who help in every part of my life. I want to send my sincerest appreciation to my family, both the ones back in China and the furry ones that accompany me here in the States. It has been 11 years since I came to the United States. My parents have never stopped giving me their utmost support during this time. They made me feel that they are always mentally by my side, even though we are physically thousands of miles away. Their encouragement supported

me in living and struggling in this foreign country while pursuing my dream of becoming a scientist. Finally, I want to thank my furry family, my cats Ginger and Shadow, and my dog Yoyo. When I was in a bad mood, when I felt lost about my future, and when I missed my family, they were always there by my side and gave me emotional support, helping me get through difficult day. A lot has happened during my PhD journey. Ginger left me because of an accident. Shadow was seriously sick and needed surgery but thankfully, has recovered well. Ginger's passing and Shadow's surgery have made me realize that accidents can happen at any moment, and you never know which will come first, an accident or tomorrow. It taught me to cherish and enjoy every minute of every day of life.

I'm very grateful to every person and every little furry friend who has appeared in my life over the past five years and offered me help. I wouldn't be where I am today without you. I hope the road ahead will be smooth sailing. Thank you all!

Chapter 1

Introduction

1.1 Kidney

Kidneys are essential organs that play a critical role in regulating blood pressure, maintaining the balance between water, salt, and minerals, and, most importantly, the filtration of waste products from the blood[1]. They filter about 110-140 liters of blood daily (for humans), removing waste products like toxins while producing 1-2 liters of urine[2]. Impaired kidney functions can lead to various kidney diseases, both acute (sudden failure of kidney function) and chronic (CKD (chronic kidney disease), or gradual loss of kidney function over time).

In the United States, kidney diseases pose a significant public health challenge. Approximately 37 million people, or about 1 in 7 adults, are affected by CKD, with many individuals being undiagnosed due to the asymptomatic nature of the alterations at early stages, and with kidney diseases collectively ranking as the ninth most common cause of death. Even in healthy aging, the functional unit of the kidney is progressively lost, leading to a substantial diminishment of filtration capacity[3]. Additionally, the annual cost of CKD exceeds $130 billion, underscoring the major economic burden of kidney disease.

The widespread prevalence and huge consequences of kidney diseases, together with a long history of research and significant ongoing effort in understanding kidney function and disease, underscore the urgency for new approaches to deepen our knowledge of the kidney and develop improved diagnostic and therapeutic strategies.

The kidney is a bean-shaped organ composed of two main layers, an outer cortex layer

and an inner medulla layer called the renal pyramisd. An artery bearing unfiltered blood flows into these layers through the renal pelvis (**Figure 1.1 A**) and branches into capillaries, which enter the basic functional unit of the kidney, the nephron (**Figure 1.1 B**). Each nephron consists of a renal corpuscle, a proximal convoluted tube (PCT), a loop of Henle, a distal convoluted tubule (DCT), and a collecting duct. Blood filtration starts as the glomerulus of the renal corpuscle passes water and small molecules to the PCT while retaining large molecules such as proteins and cells. As the filtered blood exits the renal corpuscle and enters the PCT, molecules with nutritional significance, such as glucose, amino acids, and small peptides, are reabsorbed by the renal tubule and transported to nearby capillaries. Additional reabsorption is continued in the loop of Henle, a U-shaped tubule that facilitates the recovery of water and sodium chloride from the urine. The DCT then connects and ascends to the cortex region while reabsorbing small molecules like water and ions. Eventually, the collecting ducts gather the filtrates from multiple nephrons and reabsorb more water, producing concentrated urine for excretion.

1.1.1 Filtration Machinery: Glomerulus

As the first step of the blood filtration system, the proper development and preservation of the glomeruli are crucial to the regular functioning of the kidney. A considerable number of kidney problems are caused by the structural and functional changes of the glomeruli [4–8]. The glomerulus is a network of capillaries called the glomerular tuft enclosed by a cup-like membranous structure called Bowman's capsule (**Figure 1.1C**). These capillaries consist of a thin fenestrated layer of glomerular endothelial cells (GEnCs) surrounded by three layers: the mesangium, the glomerular basement membrane (GBM), and podocytes. Unfiltered blood enters the glomerulus through the afferent arteriole, where it is filtered by the filtration barrier. The resulting filtrate passes through this barrier and collects in the Bowman's space before being

passed down the tubules of the nephron, where a series of reabsorption happens. The filtered blood then exits the glomerulus via the efferent arteriole.

1.1.1.1 The Mesangium

As the central stalk of the glomerulus, the **mesangium** consists of mesangial cells (MCs) embedded within the mesangial matrix, a specialized extracellular structure rich in collagen IV, laminin, and fibronectin that stabilizes the capillary loops[9,10]. In mature glomeruli, MCs directly connect with endothelial cells at the base of capillary beds and with the GBM at mesangial angles (**Figure 1.1C, D**). The mesangium plays diverse roles, including providing mechanical support to the capillaries, maintaining their structural integrity under filtration pressures, and acting as a dynamic regulator of glomerular blood flow[11]. MCs can also clear immune complexes[12], macromolecules[13], and apoptotic debris trapped in the filtration barrier through receptor-mediated endocytosis and lysosomal degradation[14]. Additionally, these cells exhibit contractile properties due to their cytoskeletal filaments resembling smooth muscle myosin. This allows them to adjust capillary surface area and diameter by contracting and relaxing in response to stimuli. When they contract, capillary diameter narrows, reducing blood flow and filtration surface area; when they relax, capillaries expand, allowing increased blood flow and filtration. These dynamic properties of the mesangial cells is a critical component in ensuring effective filtration [15–18].

1.1.1.2 The Glomerular Endothelium

Supported by the mesangium are the other critical components of the glomerulus, called the **glomerular endothelium**. Unlike other capillary endothelilum, the glomerular endothelium has unique dense fenestrations[19]. This fenestrated endothelium forms a layer of size-selecting sieve, preventing large macromolecules and cells (like red blood cells) from being filtered out. The luminal surface of the endothelium is covered by a thin, carbohydrate-rich, negatively charged layer called the glycocalyx. The glycocalyx serves several purposes. First, it provides a protective coat and reduces shear stress introduced by the bloodstream. Second, it is highly involved in molecular signaling and the regulation of blood. Lastly, it serves as the first layer of the glomerular filtration barrier, preventing negatively charged molecules from leaking into the urine.

1.1.1.3 Glomerular Basement Membrane

Unlike the glomerular endothelium, the GBM is the non-cellular layer located outside of the endothelium and the mesangium[10,20–22]. Like other basement membranes in the system, it is composed of matrix proteins like laminin, type IV collagen, nidogen, and heparan sulfate proteoglycans (HSPGs). The GBM is different from other basement membranes in both structural and functional perspectives. **Structurally**, the GBM contains unique isoforms of type IV collagen (α3, α4, α5 chains), and laminin-521, which are not typically present in other basement membranes[20,23]. These specialized components contribute to the unique functionality of the GBM. **Functionally**, while other basement membranes primarily provide structural support and compartmentalization, the GBM serves as a size- and charge-selective filtration barrier for

blood. The dense meshwork formed by the collagens and laminin prevents the passage of large molecules such as proteins while allowing small molecules like water and ions to pass through. Additionally, the uniformly distributed negative charges of the HSPG provide charge-selective permeability of the GBM, effectively repelling negatively charged molecules such as albumin from being filtered.

1.1.1.4 Podocytes

Lastly, podocytes are a highly specialized type of epithelial cell that plays a critical role in maintaining the filtration barrier of the glomerulus in the kidney. Located on the outer surface of the GBM, podocytes form intricate finger-like structures called foot processes that interdigitate to form narrow gaps known as filtration slits. These foot processes are bridged by a specialized protein-rich structure called the slit diaphragm **(Figure 1.1D),** forming densely packed pores together with the foot processes, which further prevents the filtration of large molecules.

Similar to the GBM, these cells are not only essential for providing structural integrity but also contribute to its selective permeability by regulating the passage of molecules based on size and charge. Many podocyte-related molecules such as podocalyxin, nephrin, and podocin are heavily glycosylated and contain negatively charged groups, such as sulfates, which repel negatively charged molecules and prevent their passage through the barrier. Damage or dysfunction of podocytes is a hallmark of many kidney diseases, often leading to proteinuria and impaired filtration, underscoring their vital role in kidney function.

The podocytes, along with the fenestrated endothelium and the GBM, collectively form

the glomerular filtration barrier (GFB), a three-layered filtration barrier (**Figure 1.1D**) that acts as a size-selecting sieve in which water and small solutes are freely permeable while retaining larger-sized proteins, macromolecules, and cells in the blood[24,25].

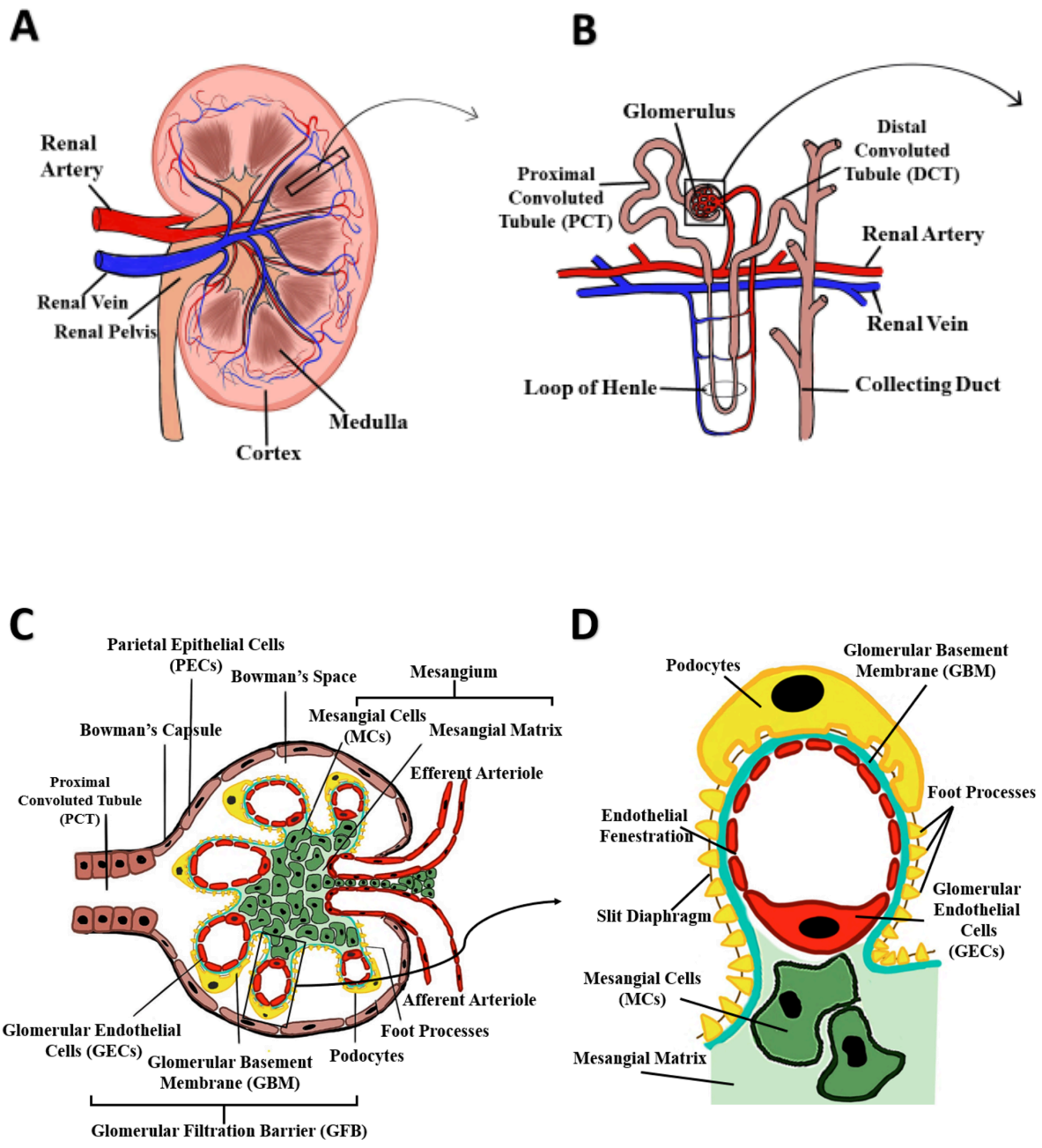

Figure 1.1. Basic anatomy of *(A) Kidney; (B) Nephron; (C) Glomerulus; (D) Glomerular filtration barrier (GFB).*

1.1.2 Reabsorption Center: Tubules

After the glomerulus filters the blood, the remaining filtrate enters the renal tubule (**Figure 1.2**), a specialized tubular structure responsible for reabsorbing key molecules, regulating electrolyte balance, and eliminating waste as urine[26]. The filtrate first travels through the proximal convoluted tubule (PCT), which has been shown to be further divided into three segments, S1, S2, and S3[27,28]. The S1 segment is primarily responsible for reabsorbing a large portion of water, sodium, and nutrients like glucose and small proteins while also secreting organic acids. In the S2 segment, reabsorption continues, particularly of amino acids and solutes, where pH is regulated. The S3 segment continues to reabsorb sodium and chloride, with additional pH regulation before the filtrate moves downstream to U-shaped tubules that dive deep into the medulla and return to the cortex, the loop of Henle (LOH).

Exiting from the PCT, the filtrate moves to the LOH, where crucial regulation in water and electrolyte balance occurs. In the descending limb of the LOH, water is reabsorbed passively due to osmotic gradients, concentrating the filtrate. As the filtrate moves into the ascending limb, ions such as sodium, potassium, and chloride are actively reabsorbed, diluting the filtrate as it ascends. This countercurrent mechanism helps establish a high osmolarity in the medulla, which is essential for concentrating urine. Finally, in the distal convoluted tubule (DCT), further regulation of other salt ions takes place before the filtrate moves into the collecting ducts, where the urine is collected and excreted.

Together, these three segments of the proximal tubule work in coordination to maintain homeostasis by efficiently reabsorbing important molecules that get filtered through the glomerulus and eliminating waste products. Any disruption in the tubules can lead to imbalances in these processes, resulting in issues such as electrolyte imbalance, proteinuria, and impaired waste elimination. Such changes can have significant effects on kidney function and overall renal health.

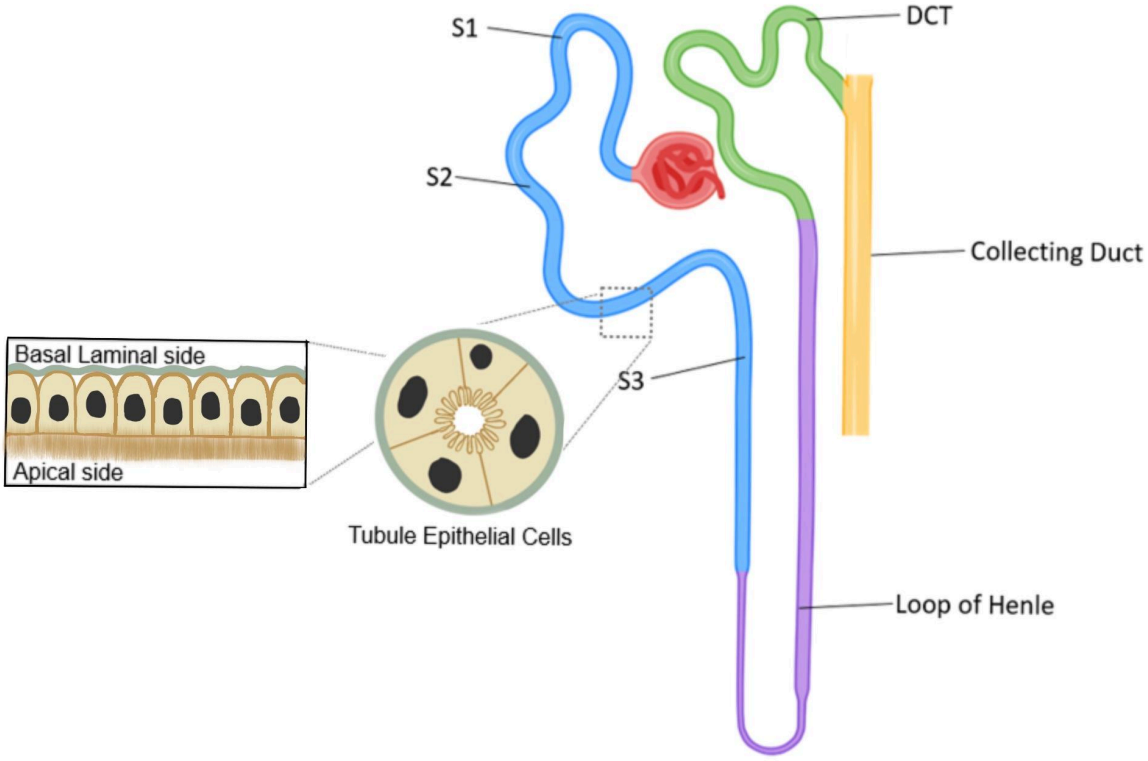

Figure 1.2. Demonstration of different nephron tubule sections. *Blue: proximal convoluted tubule. Purple: Loop of Henle. Green: Distal convoluted tubule. Yellow: collecting duct.*

1.1.3 Glomerular and Tubular Alterations: Pathways to Kidney Disease

Maintaining the structural integrity of the glomerulus and tubules is essential for proper kidney function, as even subtle disruptions at the nanoscale can lead to significant impairments in regular kidney function. When these glomerular compartments are compromised—whether due to aging, genetic disorders, or immune-mediated damage- progressive pathological changes can occur, ultimately leading to chronic kidney disease and loss of renal function.

1.1.3.1 Aging-Related Alterations

Kidney function gradually declines with age, and the risk of kidney diseases is remarkably high with aging, leading to an increased prevalence of chronic kidney disease (CKD) in older individuals[3,29–33]. These age-related alterations often disrupt the kidney's ability to effectively filter blood (within the glomerulus) and maintain homeostasis (within the tubules). Common changes include thickening of the GBM, podocyte loss, FP alterations[3], and glomerular endothelial fenestration effacement (**Figure 1.3A**). In addition, tubular atrophy and interstitial fibrosis (**Figure 1.3B**) further contribute to the progressive decline in renal function.

Given the significant impact of these changes on kidney health with aging, ongoing research is focused on understanding the molecular and cellular mechanisms driving aging-related alterations, with the ultimate goal of identifying potential therapeutic strategies to slow, stop, or even reverse these processes.

1.1.3.2 Pathological Alterations

While some changes within the kidney can occur gradually with aging, others can arise due to underlying diseases that accelerate glomerular damage and impair kidney function even at young ages. Chronic conditions such as hypertension and diabetes can accelerate these changes, leading to nephrosclerosis or diabetic nephropathy[34,35]. In diabetic nephropathy, for instance, persistent high blood sugar damages the glomerular capillaries, resulting in GBM thickening and ultimately proteinuria and kidney failure[36–39].

Another significant pathological alteration in the glomerulus is mesangial expansion (**Figure 1.3C, left**), often evident in some progressive kidney diseases like focal segmental glomerulosclerosis (FSGS) and IgA nephropathy[40]. As discussed earlier, mesangial cells provide structural support and many other functions for the glomerular capillaries, but excessive proliferation and accumulation of extracellular matrix can impair filtration. In some acute cases, such as crescentic glomerulonephritis[41], the glomerulus can develop crescents (**Figure 1.3C, middle**), or layers of proliferated epithelial cells in Bowman's space, which indicate severe injury and can lead to rapid loss of kidney function if untreated. These glomerular changes, along with accompanying tubular injury and interstitial inflammation, are hallmarks of many chronic kidney diseases that will ultimately progress to end-stage renal disease (ESRD). Understanding the mechanisms underlying these pathological alterations is hence crucial for developing targeted therapies to preserve kidney function and prevent disease progression.

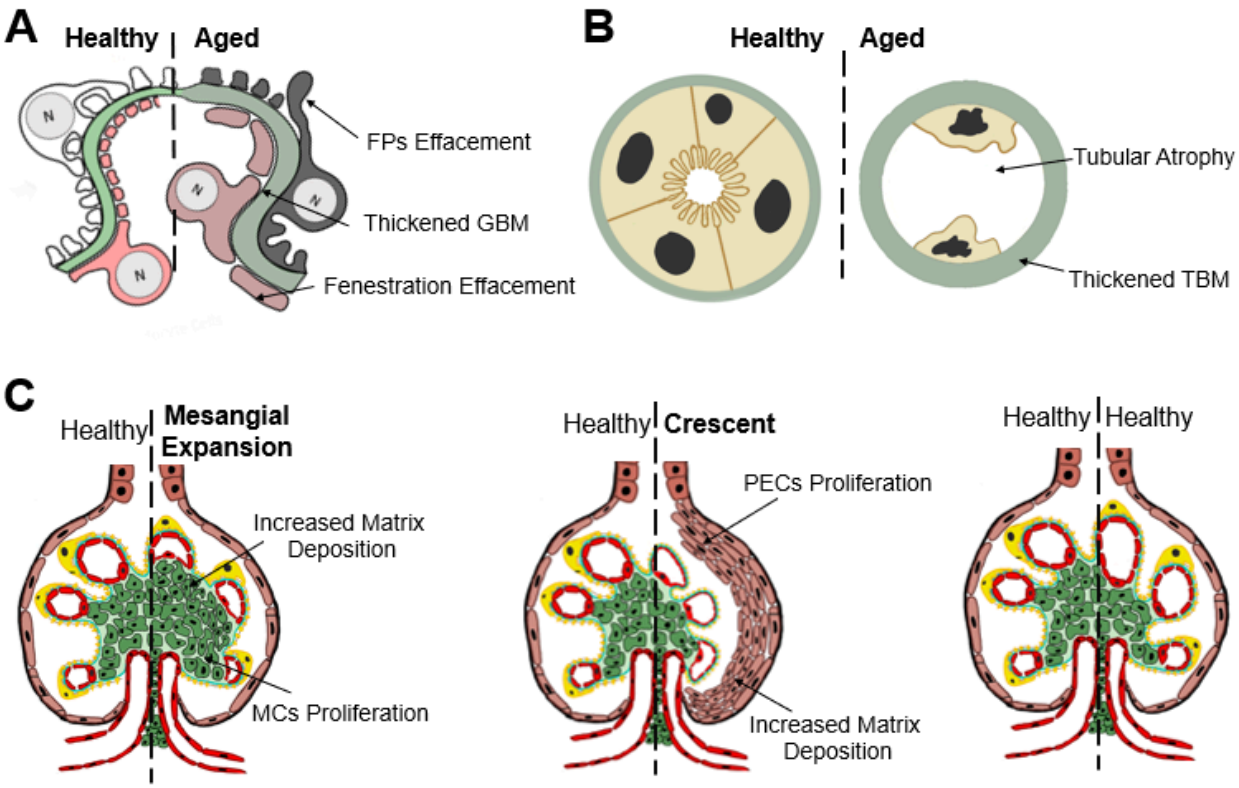

Figure 1.3. Several examples of common pathological alterations in the kidney. A) *Aging-associated changes in the glomerular filtration barrier and tubules.* ***B)*** *Mesangial expansion and crescent formation in the glomerulus, characteristic of progressive glomerular diseases such as FSGS.*

1.2 Imaging of Kidney

Understanding the structural and functional changes that occur in the kidney during health and disease requires detailed visualization at multiple scales. To fully appreciate these changes, nephrologists or renal pathologists typically study glomerular morphology using both light and electron microscopy to better understand or diagnose and treat the specific disease[42–44].

1.2.1 Light Microscopy

Light microscopy has long been commonly used for imaging overall physiology of the kidney, the localization, and the identification of key molecules with high specificity [45–49]**.** Standard histological stains, such as hematoxylin and eosin (H&E) or periodic acid-Schiff (PAS), reveal the overall organization of glomeruli and tubules, while immunofluorescence enables precise localization of protein complexes, such as nephrin in podocytes or collagen IV in the glomerular basement membrane. However, its utility, light microscopy, is limited by optical resolution and the inability to resolve structures smaller than ~200 nm due to the diffraction limit of light[50–53].

1.2.2 The Diffraction Limit of Light

While light microscopy is good for imaging large areas of biological samples, its spatial resolution is modest compared to other traditional techniques such as electron microscopy. Light, as a wave, when passing through an aperture, will diffract and create a radial pattern with alternating bright and dark bands due to the constructive/destructive interactions among light waves (**Figure 1.4A**). Light emitted from a point source (e.g., a fluorophore) on the sample passes through an objective and creates a similar 3-dimensional diffraction pattern called the

point spread function (PSF) with a central high peak surrounded by a series of descending peaks (**Figure 1.4B**). The size of the PSF is determined by both the wavelength (λ) of the light source and the numerical aperture (NA) of the objective lens, which are related to each other with **Equation [1]** describing the closest distance *d* between two point sources where the PSFs can be well separated from each other. Two objects can only be resolved if separated by a distance that is greater than the full-width-half-maximum (FWHM) of the PSF's central peak.

In 1873, Ernst Abbe first described the lateral spatial resolution of an optical microscope using the equation:

$$d = \lambda/2NA \qquad [1]$$

Theoretically, the larger the NA of an objective lens, the smaller the diffraction limit, and the better the resolution. However, in practice, the NA of an objective lens is constrained by the refractive index of the imaging medium and some physical limitation of the design, which limits the resolution of typical light microscopy to around 200-300 nm laterally.

Axial resolution, on the other hand, which refers to the ability to distinguish two objects along the z-axis, is described by a different equation:

$$d = 2\,\lambda/NA^2 \qquad [2]$$

Axial resolution is inherently worse than lateral resolution for typical single-objective lens microscopes, typically ranging between 500–800 nm for high-NA objectives. This anisotropy in resolution arises from the elongated PSF in the axial direction, forming an ellipsoid rather than a perfect sphere (**Figure 1.4B**). As with lateral resolution, a higher NA improves axial resolution, but the improvement is still limited by practical constraints.

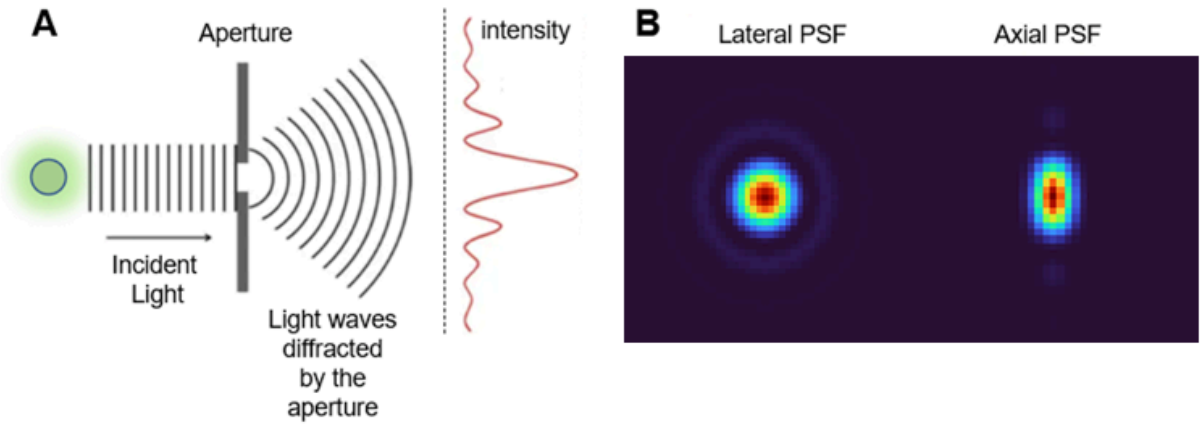

Figure 1.4. Diffraction of light and optical resolution. *A) An illustration of the diffraction of light when it passes through an aperture. B) An illustration of the lateral and axial point spread function as a result of diffraction of light.*

Due to the intrinsic diffraction limit of light, subcellular structures within the kidney, such as podocyte foot processes (FPs) and the fenestrated endothelium, which in mouse kidneys, have a repeat distance less than ~200 nm, are challenging to visualize using standard light microscopy. This limitation has hindered nephrologists and researchers across various disciplines from making fundamental biological discoveries at the nanoscale.

1.2.3. Super-Resolution Microscopy: Expansion Microscopy

In response to the fundamental challenge of the diffraction limit of light, significant efforts over the past decades have focused on surpassing the diffraction limit. Super-resolution methods such as stimulated emission depletion microscopy (STED, **Figure 1.5A**), which confines fluorescence emission using a depletion beam, and stochastic optical reconstruction

microscopy (STORM, **Figure 1.5B**), which relies on sequentially activating and localization of special fluorophores, both improve resolution by effectively reducing the size of the PSF. In contrast, structured illumination microscopy (SIM, **Figure 1.5C**) surpasses the diffraction limit by using patterned illumination to computationally reconstruct high-frequency spatial information, rather than directly modifying the PSF. However, these super-resolution methods often require highly specialized instruments, prolonged acquisition times, high laser power, and special fluorophores, which can limit their wider accessibility and applicability.

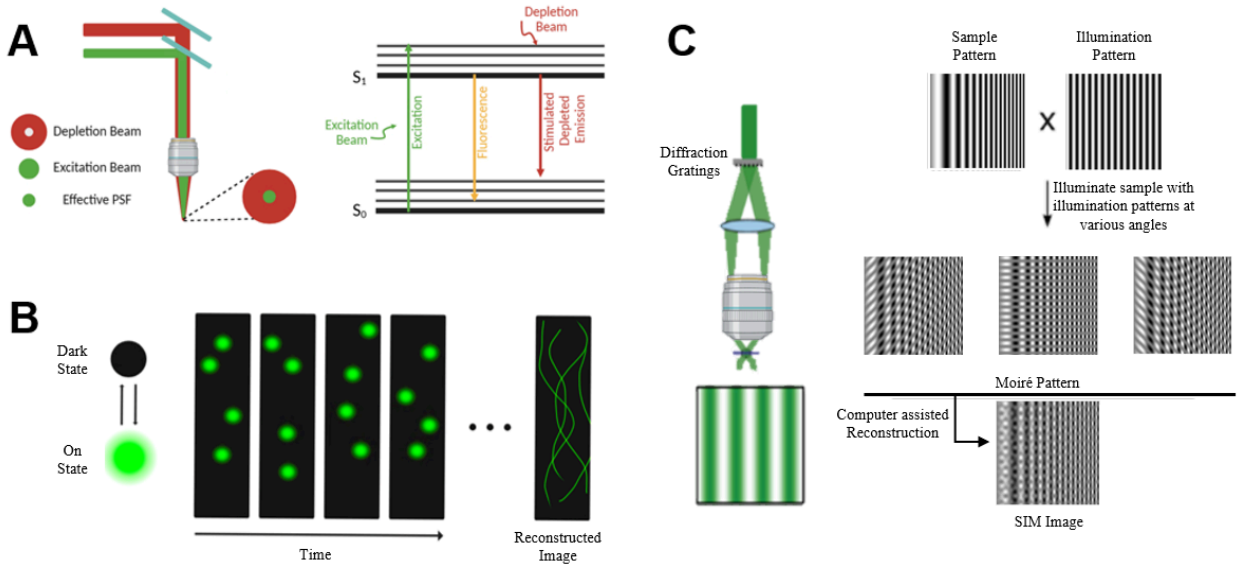

Figure 1.5. Principles of several super-resolution microscopy techniques. *A) Stimulated emission depletion (STED) uses a depletion beam to reduce the effective fluorescence PSF. B) Stochastic optical reconstruction microscopy (STORM) uses stochastic activation and localization of single molecules to improve resolution, C) Structured illumination microscopy (SIM) uses structured illumination patterns and computer-aided reconstruction to enhance spatial resolution.*

The more recent development of expansion microscopy (ExM) has allowed an alternative

approach that uses the physical expansion of the specimen to overcome the diffraction limit using traditional microscopes[54,55]. In ExM, the specimen is uniformly expanded in all directions, resulting in features closer than the diffraction limit that can be resolved after expansion because they are physically moved apart. As illustrated in **Figure 1.6**, the swellable hydrogel network is grown with and around the sample. The proteins, fluorophores, and the antibody are covalently linked to the polymer network via methacryloyl group-based linkers. Once the polymer networks have grown, the mechanical support within the sample is degraded using either enzymatic digestion (ExM)[56] or high-temperature detergent homogenization (MAP)[57]. Finally, the gel is immersed in deionized water. The high salt concentration in the unexpanded gel drives water influx into the gel, causing it to expand in three dimensions and achieving a spatial resolution of ~60 nm. Under proper conditions, the process can be performed with remarkably small distortions, ~2-5%, preserving the sample structural pattern while enhancing the resolution.

Unlike the other super-resolution methods mentioned earlier, ExM surpasses the diffraction limit using simple chemicals and procedures accessible by most laboratories while remaining compatible with standard diffraction-limited microscopes[56,58]. Additionally, unlike other methods, an expanded specimen becomes optically transparent with a uniform refractive index throughout, making it an excellent tool for imaging much thicker samples.

Due to these benefits of the ExM, it has been rapidly adopted by the biomedical research community to image the precise localization of key molecules and proteins that play important roles in pathological alterations in the kidney at high resolution, providing valuable insights into cellular and tissue architecture previously inaccessible with conventional microscopy techniques.

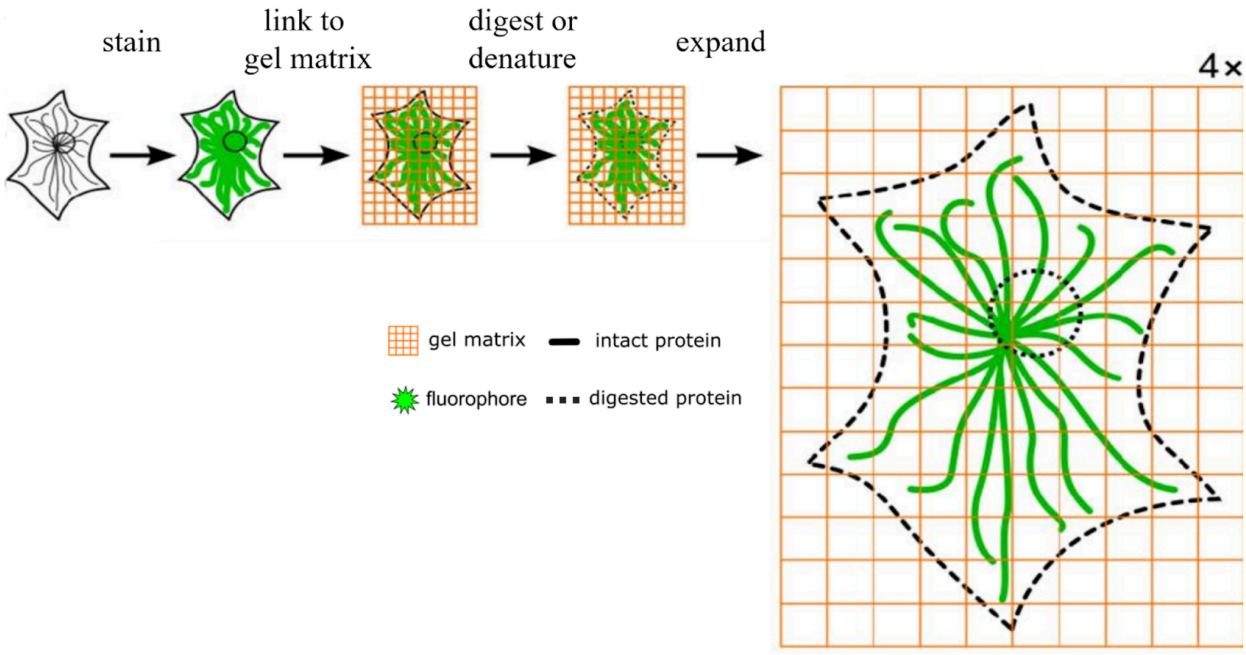

Figure 1.6. Illustration of the expansion microscopy concept. *The selected cell/tissue samples are first stained with fluorescently labeled antibodies. Then the sample is embedded in a swellable hydrogel network, and the fluorophore-conjugated fluorophores are linked to the hydrogel. The sample's mechanical support was degraded using either enzymatic digestion or high temperature and detergent denaturation. Finally, the hydrogel containing the sample is placed in deionized water to achieve ~4× isotropic volumetric expansion. The figure is adapted from Chozinski et al.*[58] *with permission.*

1.2.4. Electron Microscopy: The Ultrastructural Detailed Imaging

Many glomerular diseases exhibit morphological changes that can be easily observed using routine light microscopy, but some glomerular diseases involve more subtle alterations that require examination at the nanometer scale for accurate visualization and analysis. For example, minimal change disease (MCD) is among the most common causes of nephrotic syndrome. It is characterized by the effacement of podocyte foot processes in glomeruli and perturbations to the

glomerular basement membrane that cause proteins to leak through the GFB[59–61]. As the name MCD implies, these changes in foot processes are so subtle that they often appear to be normal under LM. Therefore, alternative approaches capable of detecting and visualizing these subtle changes are needed.

Electron microscopy (EM) is a long-established and powerful imaging technique that uses a beam of electrons instead of light to achieve nanoscale resolution (1–10 nm), far surpassing the diffraction limit of conventional optical microscopy and even super-resolution techniques. By leveraging the shorter wavelength of electrons, EM has been widely used to visualize subcellular ultrastructures with exceptional detail.

In kidney research, EM plays a crucial role in studying glomerular architecture, subtle changes in disease states, and the organization of key nanoscale components such as podocyte foot processes[43,44,49], glomerular basement membrane (GBM) protein organization[49], and endothelial fenestrations. There are several variants of EM: Transmission electron microscopy (TEM) is commonly used to examine the ultrastructures of the GBM and detect abnormalities in filtration barrier components in 2D, while serial block face scanning electron microscopy (SBF-SEM) provides detailed three-dimensional surface morphology of glomeruli and renal tubules[62,63]. These capabilities make EM an indispensable tool for understanding kidney physiology and pathology at the molecular level.

1.3 Illuminating the Kidney: Labeling Strategies and Techniques

To better understand the structure, composition, and function of the kidney glomerulus, it is essential to apply appropriate labeling methods. These techniques facilitate the visualization of

both specific and overall cellular and extracellular components within the glomerulus, offering critical insights into its normal physiology and pathological states. Routine LM of kidney tissue and glomeruli frequently uses histological stains[64,65] or the direct labeling of specific protein targets using immunostaining with antibodies[66,67].

1.3.1 Histology Stains

Histological stains are among the earliest and most widely used labeling techniques for labeling the glomerulus within the nephrology community. Hematoxylin and Eosin (H&E) staining is often regarded as the "gold standard" in medical histology[64,65]. Hematoxylin by itself does not stain the tissue; it is normally used along with some metals, often aluminum, which forms a positively charged complex that binds to the negatively charged DNA in nuclei, producing a purplish-blue color. Eosin, a negatively charged dye, labels the extracellular matrix and cytoplasm, with varying shades of pink depending on tissue composition. Other stains, such as Periodic Acid-Schiff (PAS), use hydrazide-aldehyde coupling to label glycoproteins and basement membranes that were oxidized by sodium periodate, making them invaluable for assessing glomerular architecture and detecting structural abnormalities. Additional common histological methods include Masson's Trichrome, which stains collagen and reveals fibrotic changes, and Feulgen Stain, used to visualize the nuclei[64]. Together, these staining methods provide foundational tools for understanding the structure and pathological alterations of the glomerulus.

However, despite their widespread application in the nephrology community, these methods are generally optimized for brightfield microscopy, making it challenging for

volumetric imaging due to the scatter of light through thicker samples, restricting their use primarily to thin tissue sections. Furthermore, stains like hematoxylin label their targets through affinity-based interactions, which limit their compatibility with advanced super-resolution techniques such as expansion microscopy.

1.3.2 Immunolabeling

Immunolabeling is a powerful technique that enables the specific visualization of proteins, cellular structures, and extracellular components in biological tissues, including the kidney glomerulus. This method relies on antibodies that bind with high specificity to their target antigens, providing a critical tool for understanding glomerular structure, function, and pathological changes with high specificity.

In kidney glomerulus studies, immunolabeling allows researchers to identify and localize key molecular markers associated with its distinct cellular and extracellular components. For example, podocyte-specific proteins such as nephrin and podocin can be labeled to study slit diaphragm integrity and measure the width of individual foot processes[45,68,69], while markers like type IV collagen and laminin are commonly used to study the organization of the glomerular basement membrane (GBM) composition[70].

Antibodies can be employed in two main ways to visualize specific targets, depending on the experimental requirements. Direct immunolabeling (**Figure 1.7, left**) uses primary antibodies conjugated directly to a fluorescent dye, offering a shorter staining protocol by eliminating the need for another round of staining with secondary antibodies. This approach is especially

advantageous for multi-target imaging, as it minimizes potential cross-reactivity between species and reduces background noise. However, direct labeling can be costly due to the need for fluorophore conjugation for each primary antibody if the fluorophore-antibody conjugate is not commercially available.

Indirect immunolabeling (**Figure 1.7, right**), on the other hand, involves an unlabeled primary antibody binding to the target antigen, followed by a secondary antibody conjugated to a fluorescent dye. This method provides significant signal amplification, as multiple secondary antibodies can bind to a single primary antibody, though at the cost of a longer experimental protocol.

In recent years, immunolabeling has been combined with advanced imaging techniques such as **super-resolution methods** (see **section 1.2**) to achieve high-resolution visualization of glomerular components. Additionally, immunostaining can be easily adapted for volumetric imaging, allowing for the visualization of three-dimensional structures with high specificity and resolution. Recent developments in highly-multiplexed immunolabeling (20-100 labels) have enabled the detection of multiple targets within the same sample[71–73], allowing comprehensive studies of the interactions between key glomerular compartments, however, it requires sufficient knowledge about computational analysis, complex mathematical algorithms, or special dyes.

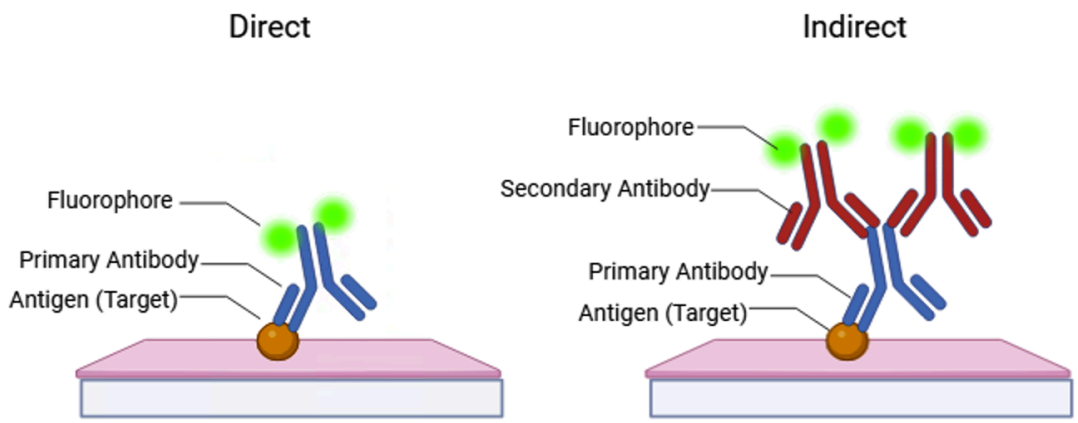

Figure 1.7. Illustration of direct and indirect immuno-labeling. *Direct labeling involves a primary antibody directly conjugated to a reporter molecule such as a fluorophore. Whereas in indirect labeling, unconjugated antibodies are used to first label the antigen, followed by a reporter-conjugated secondary antibody specific to that primary antibody.*

1.3.3 Fluorescent Labeling of Abundant Reactive Entities (FLARE)

While multiplexed immunolabeling has significantly expanded the field's ability to visualize multiple targets simultaneously, it remains technically challenging, especially for thick tissues. Moreover, despite the antibody's high specificity, immunolabeling can be time-consuming and expensive. These limitations underscore the need for a method that can provide a comprehensive view of kidney physiology and enable 3D imaging of whole tissue, facilitating a more integrated analysis of glomerular structure and function on a larger scale.

Fluorescent Labeling of Abundant Reactive Entities (FLARE)[74,75] is a simple chemical staining method that combines the advantages of both histology stains and fluorescence labeling, enabling easy volumetric imaging while revealing key glomerular features simultaneously.

FLARE enables the labeling of three main types of biological macromolecules: carbohydrates, proteins, and nucleic acids/DNA (**Figure 1.8**). The method works by first oxidizing carbohydrates in the specimen into aldehydes, which are then chemically linked to commercially available hydrazide-functionalized fluorescent dyes, similar to the classic histology PAS stain. Next, primary amines found in proteins are labeled with NHS-functionalized reactive dyes. Finally, DNA is labeled using standard DNA-binding fluorescent dyes, such as Hoechst or SYBR Green.

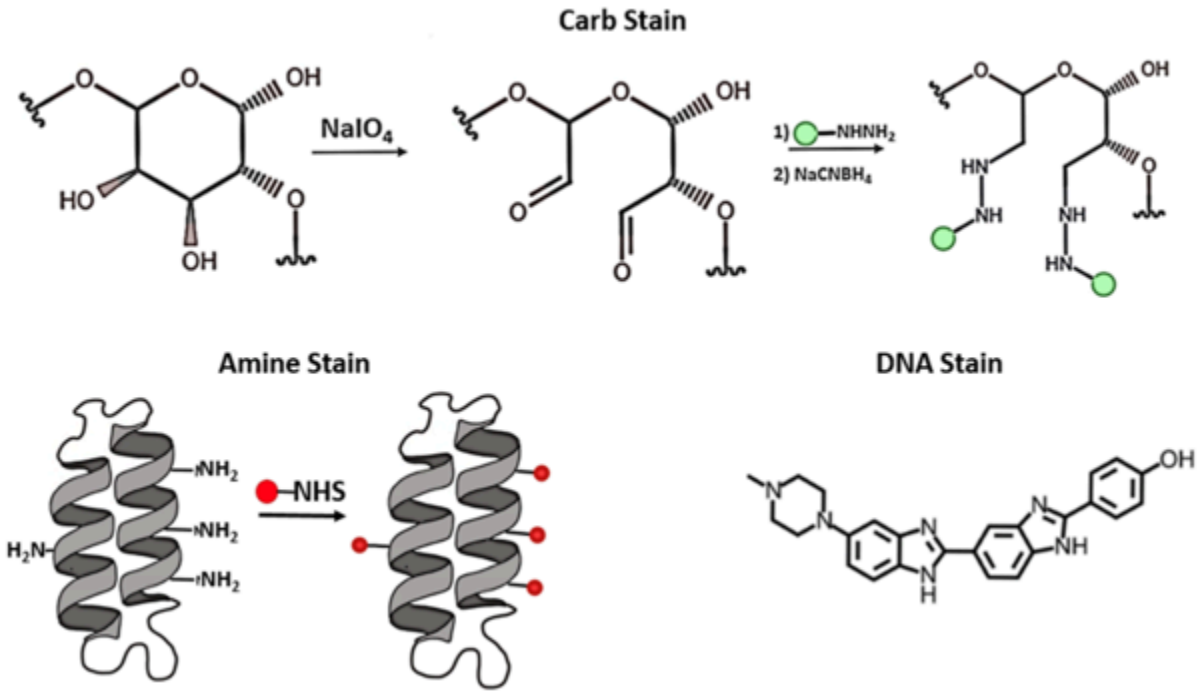

Figure 1.8. FLARE stain chemistry*. Vicinal diols of carbohydrates are oxidized to aldehydes with sodium periodate, which is then reacted with hydrazide-functionalized fluorophores and stabilized by reduction with sodium cyanoborohydride. Primary amine groups on proteins are labeled by reacting with NHS-functionalized fluorophores. DNA is labeled using conventional DNA dye (Hoechst or SYBR Green).*

1.4 Current Challenges and Knowledge Gaps in Kidney Research

The regular functioning of each component collectively contributes to the overall performance of the glomerulus. Despite significant advancements in labeling and imaging techniques, the study of glomerular structure and function still faces several critical limitations. Traditional methods primarily rely on two-dimensional (2D) thin sections, which pose challenges in capturing the full complexity of glomerular architecture. Many essential features, especially the ones that exhibit strong spatial characteristics, such as glomerular capillary connectivity[42] and spatial relationships between compartments, cannot be fully captured in 2D datasets. Additionally, our current knowledge of glomerular morphology and structure is often based on separate studies of individual substructures from different glomeruli, making it difficult to directly correlate these structures and potentially leading to conflicting interpretations. The above limitations have generally shaped the field's approach to analyzing the glomeruli's limited portion or features.

1.4.1 The Need for 3D Holistic Reconstruction in Glomerular Research

A growing body of research emphasizes the importance of three-dimensional (3D) analysis in uncovering spatial characteristics of glomerular structures that are otherwise hidden in 2D studies. Advanced techniques like NIPOKA[69] enabled detailed visualization of podocyte foot processes (FPs), yet they were only done on thin FFPE sections (5-10 μm), hence providing a limited perspective and not providing a holistic view of the entire glomerulus. Similarly, STED-based approaches, such as those demonstrated by Unnersjö et al.[46], offer high-quality FP imaging but lack insight into broader compartmental interactions. In contrast, Burghardt et al. reconstructed complete podocytes and their environments, revealing that slit diaphragms are not formed within the foot processes of the same podocyte and that podocyte foot processes exhibit extensive cell-to-cell contacts[76]. These findings, which are unattainable in traditional 2D partial analyses, underscore the necessity of comprehensively studying glomerular structures in 3D.

However, current imaging techniques are limited in their ability to provide a detailed 3D reconstruction of multiple glomerular compartments simultaneously. This limitation has hindered the comprehensive exploration of spatial coordination among various compartments. Therefore, a method capable of integrating detailed 3D reconstruction of all glomerular compartments is critical to gaining a holistic understanding of glomerular morphology and function.

1.4.2 Toward a More Comprehensive Understanding of Glomerular Function

The glomerulus functions as an intricate machine, where local structural changes may have broader implications across the entire unit. Previous research has extensively examined

localized alterations in glomerular disease, yet it remains unclear whether these changes drive global adaptations within the glomerulus or affect distant structures in ways that are not easily detectable in conventional assays. The field has largely overlooked the broader structural coordination within the glomerulus, which could offer crucial insights into the progression of kidney diseases.

There is an urgent need for an approach that can label complex structures, images, and quantify the glomerulus as an integrated, functioning unit to achieve a more comprehensive understanding of its structural and pathological changes. Expanding 3D imaging techniques and integrating them with nanoscale molecular analyses will help bridge the gap between localized structural alterations and global glomerular function, potentially revealing novel aspects of disease progression that remain unexplored.

1.5 Summary

The kidney is an important organ that, if compromised, can lead to significant health concerns. Advancements in volumetric imaging and labeling techniques have enhanced our understanding of glomerular morphology and function. However, current methods often focus on thin sections or individual compartments, lacking the capability to image and reconstruct multiple glomerular compartments simultaneously. This limitation has hindered a comprehensive understanding of glomerular function. In the following chapter, this thesis introduces a novel super-resolution fluorescence microscopy pipeline designed for holistic three-dimensional imaging of entire mouse glomeruli at 100 nm resolution. The chapter will further demonstrate the scalability and versatility of this method in various experimental contexts.

1.6 References

1. Your Kidneys & How They Work | NIDDK. National Institute of Diabetes and Digestive and Kidney Diseases. Accessed May 8, 2022. https://www.niddk.nih.gov/health-information/kidney-disease/kidneys-how-they-work
2. The Urinary Tract & How It Works - NIDDK. National Institute of Diabetes and Digestive and Kidney Diseases. Accessed November 22, 2024. https://www.niddk.nih.gov/health-information/urologic-diseases/urinary-tract-how-it-works
3. Shankland S, Wang Y, Shaw A, Vaughan J, Pippin J, Wessely O. Podocyte Aging: Why and How Getting Old Matters. *JASN*. Published online September 21, 2021. doi:10.1681/ASN.2021-05-0614
4. Anderson S, Brenner BM. Effects of aging on the renal glomerulus. *The American Journal of Medicine*. 1986;80(3):435-442. doi:10.1016/0002-9343(86)90718-7
5. Quaggin SE, Kreidberg JA. Development of the renal glomerulus: good neighbors and good fences. *Development*. 2008;135(4):609-620. doi:10.1242/dev.001081
6. Fu J, Lee K, Chuang PY, Liu Z, He JC. Glomerular endothelial cell injury and cross talk in diabetic kidney disease. *American Journal of Physiology-Renal Physiology*. 2015;308(4):F287-F297. doi:10.1152/ajprenal.00533.2014
7. Fu J, Akat KM, Sun Z, et al. Single-Cell RNA Profiling of Glomerular Cells Shows Dynamic Changes in Experimental Diabetic Kidney Disease. *JASN*. 2019;30(4):533-545. doi:10.1681/ASN.2018090896
8. Wiggins RC. The spectrum of podocytopathies: a unifying view of glomerular diseases. *Kidney international*. 2007;71(12):1205-1214.
9. Mason RM, Wahab NA. Extracellular Matrix Metabolism in Diabetic Nephropathy. *JASN*. 2003;14(5):1358-1373. doi:10.1097/01.ASN.0000065640.77499.D7
10. Schlondorff D, Banas B. The Mesangial Cell Revisited: No Cell Is an Island. *Journal of the American Society of Nephrology*. 2009;20(6):1179-1187. doi:10.1681/ASN.2008050549

11. The glomerular mesangial cell: an expanding role for a specialized pericyte. Accessed December 6, 2024. https://faseb.onlinelibrary.wiley.com/doi/epdf/10.1096/fasebj.1.4.3308611
12. Novak J, Vu HL, Novak L, Julian BA, Mestecky J, Tomana M. Interactions of human mesangial cells with IgA and IgA-containing immune complexes1. *Kidney International*. 2002;62(2):465-475. doi:10.1046/j.1523-1755.2002.00477.x
13. Farquhar MG, Palade GE. FUNCTIONAL EVIDENCE FOR THE EXISTENCE OF A THIRD CELL TYPE IN THE RENAL GLOMERULUS : Phagocytosis of Filtration Residues by a Distinctive "Third" Cell. *Journal of Cell Biology*. 1962;13(1):55-87. doi:10.1083/jcb.13.1.55
14. Savill J, Smith J, Sarraf C, Ren Yi, Abbott F, Rees A. Glomerular mesangial cells and inflammatory macrophages ingest neutrophils undergoing apoptosis. *Kidney International*. 1992;42(4):924-936. doi:10.1038/ki.1992.369
15. Ebefors K, Bergwall L, Nyström J. The Glomerulus According to the Mesangium. *Front Med*. 2022;8. doi:10.3389/fmed.2021.740527
16. Ausiello DA, Kreisberg JI, Roy C, Karnovsky MJ. Contraction of Cultured Rat Glomerular Cells of Apparent Mesangial Origin after Stimulation with Angiotensin II and Arginine Vasopressin. *J Clin Invest*. 1980;65(3):754-760.
17. Bianchi C, Gutkowska J, Thibault G, Garcia R, Genest J, Cantin M. Distinct localization of atrial natriuretic factor and angiotensin II binding sites in the glomerulus. *Am J Physiol*. 1986;251(4 Pt 2):F594-602. doi:10.1152/ajprenal.1986.251.4.F594
18. Shultz PJ, Schorer AE, Raij L. Effects of endothelium-derived relaxing factor and nitric oxide on rat mesangial cells. *American Journal of Physiology-Renal Physiology*. 1990;258(1):F162-F167. doi:10.1152/ajprenal.1990.258.1.F162
19. Haraldsson B, Nyström J. The glomerular endothelium: new insights on function and structure. *Current Opinion in Nephrology and Hypertension*. 2012;21(3):258. doi:10.1097/MNH.0b013e3283522e7a
20. Miner JH. The glomerular basement membrane. *Experimental Cell Research*. 2012;318(9):973-978.

doi:10.1016/j.yexcr.2012.02.031

21. Pollak MR, Quaggin SE, Hoenig MP, Dworkin LD. The Glomerulus: The Sphere of Influence. *CJASN*. 2014;9(8):1461-1469. doi:10.2215/CJN.09400913
22. Suh JH, Miner JH. The glomerular basement membrane as a barrier to albumin. *Nat Rev Nephrol*. 2013;9(8):470-477. doi:10.1038/nrneph.2013.109
23. Naylor RW, Morais MRPT, Lennon R. Complexities of the glomerular basement membrane. *Nat Rev Nephrol*. 2021;17(2):112-127. doi:10.1038/s41581-020-0329-y
24. Menon MC, Chuang PY, He CJ. The glomerular filtration barrier: components and crosstalk. *Int J Nephrol*. 2012;2012:749010. doi:10.1155/2012/749010
25. Reiser J, Altintas MM. Podocytes. *F1000Res*. 2016;5:F1000 Faculty Rev-114. doi:10.12688/f1000research.7255.1
26. Lawrence EA, Doherty D, Dhanda R. Function of the nephron and the formation of urine. *Anaesthesia & Intensive Care Medicine*. 2018;19(5):249-253. doi:10.1016/j.mpaic.2018.03.001
27. Faivre A, Bugarski M, Rinaldi A, et al. Spatiotemporal Landscape of Kidney Tubular Responses to Glomerular Proteinuria. *Journal of the American Society of Nephrology*. 2024;35(7):854. doi:10.1681/ASN.0000000000000357
28. Polesel M, Kaminska M, Haenni D, et al. Spatiotemporal organisation of protein processing in the kidney. *Nat Commun*. 2022;13(1):5732. doi:10.1038/s41467-022-33469-5
29. Brown L. ClinicalKey. *J Med Libr Assoc*. 2013;101(4):342-343. doi:10.3163/1536-5050.101.4.023
30. Glassock RJ, Rule AD. The implications of anatomical and functional changes of the aging kidney: with an emphasis on the glomeruli. *Kidney International*. 2012;82(3):270-277. doi:10.1038/ki.2012.65
31. Hemmelgarn BR, Zhang J, Manns BJ, et al. Progression of kidney dysfunction in the community-dwelling elderly. *Kidney International*. 2006;69(12):2155-2161. doi:10.1038/sj.ki.5000270
32. Zhang QL, Rothenbacher D. Prevalence of chronic kidney disease in population-based studies:

Systematic review. *BMC Public Health*. 2008;8(1):117. doi:10.1186/1471-2458-8-117

33. Weinstein JR, Anderson S. The Aging Kidney: Physiological Changes. *Advances in Chronic Kidney Disease*. 2010;17(4):302-307. doi:10.1053/j.ackd.2010.05.002
34. Fogo AB. Glomerular hypertension, abnormal glomerular growth, and progression of renal diseases. *Kidney International*. 2000;57:S15-S21. doi:10.1046/j.1523-1755.2000.07505.x
35. Jefferson JA, Shankland SJ. The Pathogenesis of Focal Segmental Glomerulosclerosis. *Adv Chronic Kidney Dis*. 2014;21(5):408-416. doi:10.1053/j.ackd.2014.05.009
36. Ayo SH, Radnik RA, Garoni JA, Glass WF, Kreisberg JI. High glucose causes an increase in extracellular matrix proteins in cultured mesangial cells. *Am J Pathol*. 1990;136(6):1339-1348.
37. Ayo SH, Radnik RA, Glass WF, et al. Increased extracellular matrix synthesis and mRNA in mesangial cells grown in high-glucose medium. *American Journal of Physiology-Renal Physiology*. 1991;260(2):F185-F191. doi:10.1152/ajprenal.1991.260.2.F185
38. Johnson RJ, Floege J, Yoshimura A, Iida H, Couser WG, Alpers CE. The activated mesangial cell: a glomerular "myofibroblast"? *Journal of the American Society of Nephrology*. 1992;2(10):S190. doi:10.1681/ASN.V210s190
39. Young BA, Johnson RJ, Alpers CE, et al. Cellular events in the evolution of experimental diabetic nephropathy. *Kidney International*. 1995;47(3):935-944. doi:10.1038/ki.1995.139
40. Suzuki H, Kiryluk K, Novak J, et al. The Pathophysiology of IgA Nephropathy. *JASN*. 2011;22(10):1795-1803. doi:10.1681/ASN.2011050464
41. Moroni G, Ponticelli C. Rapidly progressive crescentic glomerulonephritis: Early treatment is a must. *Autoimmunity Reviews*. 2014;13(7):723-729. doi:10.1016/j.autrev.2014.02.007
42. Terasaki M, Brunson JC, Sardi J. Analysis of the three dimensional structure of the kidney glomerulus capillary network. *Sci Rep*. 2020;10(1):20334. doi:10.1038/s41598-020-77211-x
43. Ichimura K, Miyazaki N, Sadayama S, et al. Three-dimensional architecture of podocytes revealed by block-face scanning electron microscopy. *Scientific Reports*. 2015;5:8993. doi:10.1038/srep08993
44. Burghardt T, Hochapfel F, Salecker B, et al. Advanced electron microscopic techniques provide a

deeper insight into the peculiar features of podocytes. *American Journal of Physiology-Renal Physiology*. 2015;309(12):F1082-F1089. doi:10.1152/ajprenal.00338.2015

45. Unnersjö-Jess D, Scott L, Sevilla SZ, Patrakka J, Blom H, Brismar H. Confocal super-resolution imaging of the glomerular filtration barrier enabled by tissue expansion. *Kidney International*. 2018;93(4):1008-1013. doi:10.1016/j.kint.2017.09.019
46. Unnersjö-Jess D, Scott L, Blom H, Brismar H. Super-resolution stimulated emission depletion imaging of slit diaphragm proteins in optically cleared kidney tissue. *Kidney International*. 2016;89(1):243-247. doi:10.1038/ki.2015.308
47. Pullman JM, Nylk J, Campbell EC, Gunn-Moore FJ, Prystowsky MB, Dholakia K. Visualization of podocyte substructure with structured illumination microscopy (SIM): a new approach to nephrotic disease. *Biomed Opt Express, BOE*. 2016;7(2):302-311. doi:10.1364/BOE.7.000302
48. Chozinski TJ, Mao C, Halpern AR, et al. Volumetric, Nanoscale Optical Imaging of Mouse and Human Kidney via Expansion Microscopy. *Scientific Reports*. 2018;8(1). doi:10.1038/s41598-018-28694-2
49. Randles MJ, Collinson S, Starborg T, et al. Three-dimensional electron microscopy reveals the evolution of glomerular barrier injury. *Sci Rep*. 2016;6(1):35068. doi:10.1038/srep35068
50. Galbraith CG, Galbraith JA. Super-resolution microscopy at a glance. *Journal of Cell Science*. 2011;124(10):1607-1611. doi:10.1242/jcs.080085
51. Schermelleh L, Ferrand A, Huser T, et al. Super-resolution microscopy demystified. *Nat Cell Biol*. 2019;21(1):72-84. doi:10.1038/s41556-018-0251-8
52. Coltharp C, Xiao J. Superresolution microscopy for microbiology. *Cellular Microbiology*. 2012;14(12):1808-1818. doi:10.1111/cmi.12024
53. Seeing beyond the limit: A guide to choosing the right super-resolution microscopy technique | Elsevier Enhanced Reader. doi:10.1016/j.jbc.2021.100791
54. Faulkner EL, Thomas SG, Neely RK. An introduction to the methodology of expansion microscopy. *The International Journal of Biochemistry & Cell Biology*. 2020;124:105764.

doi:10.1016/j.biocel.2020.105764

55. Wassie AT, Zhao Y, Boyden ES. Expansion microscopy: principles and uses in biological research. *Nat Methods*. 2019;16(1):33-41. doi:10.1038/s41592-018-0219-4
56. Chen F, Tillberg PW, Boyden ES. Optical imaging. Expansion microscopy. *Science*. 2015;347(6221):543-548. doi:10.1126/science.1260088
57. Woo J, Seo JM, Lee M, et al. A Modified Magnified Analysis of Proteome (MAP) Method for Super-Resolution Cell Imaging that Retains Fluorescence. *Sci Rep*. 2020;10(1):4186. doi:10.1038/s41598-020-61156-2
58. Chozinski TJ, Halpern AR, Okawa H, et al. Expansion microscopy with conventional antibodies and fluorescent proteins. *Nature Methods*. 2016;13(6):485-488. doi:10.1038/nmeth.3833
59. Fogo AB. Minimal change disease and focal segmental glomerulosclerosis. *Nephrol Dial Transplant*. 2001;16(suppl 6):74-76. doi:10.1093/ndt/16.suppl_6.74
60. Vivarelli M, Massella L, Ruggiero B, Emma F. Minimal Change Disease. *CJASN*. 2017;12(2):332-345. doi:10.2215/CJN.05000516
61. Minimal Change Disease. UNC Kidney Center. Accessed May 9, 2022. https://unckidneycenter.org/kidneyhealthlibrary/glomerular-disease/minimal-change-disease/
62. Honda K, Takaki T, Kang D. Recent advances in electron microscopy for the diagnosis and research of glomerular diseases. *Kidney Res Clin Pract*. 2023;42(2):155-165. doi:10.23876/j.krcp.21.270
63. Gagliardini E, Conti S, Benigni A, Remuzzi G, Remuzzi A. Imaging of the Porous Ultrastructure of the Glomerular Epithelial Filtration Slit. *Journal of the American Society of Nephrology*. 2010;21(12):2081. doi:10.1681/ASN.2010020199
64. Suvarna KS, Layton C, Bancroft JD, eds. *Theory and Practice of Histological Techniques*. 7. ed. Elsevier Churchill Livingston; 2013.
65. Titford M. The long history of hematoxylin. *Biotech Histochem*. 2005;80(2):73-78. doi:10.1080/10520290500138372
66. Bonsib SM. Differential Diagnosis in Nephropathology: An Immunofluorescence-Driven Approach.

Advances in Anatomic Pathology. 2002;9(2):101-114.

67. Nasr SH, Fidler ME, Said SM. Paraffin Immunofluorescence: A Valuable Ancillary Technique in Renal Pathology. *Kidney International Reports*. 2018;3(6):1260-1266. doi:10.1016/j.ekir.2018.07.008
68. Unnersjo-Jess D. *High-Resolution Imaging of Cleared and Expanded Kidney Tissue Samples*. KTH Royal Institute of Technology; 2019. https://www.diva-portal.org/smash/get/diva2:1097792/FULLTEXT01.pdf
69. Siegerist F, Ribback S, Dombrowski F, et al. Structured illumination microscopy and automatized image processing as a rapid diagnostic tool for podocyte effacement. *Sci Rep*. 2017;7(1):11473. doi:10.1038/s41598-017-11553-x
70. Suleiman H, Zhang L, Roth R, et al. Nanoscale protein architecture of the kidney glomerular basement membrane. *eLife*. 2013;2:e01149. doi:10.7554/eLife.01149
71. Francisco-Cruz A, Parra ER, Tetzlaff MT, Wistuba II. Multiplex Immunofluorescence Assays. *Methods Mol Biol*. 2020;2055:467-495. doi:10.1007/978-1-4939-9773-2_22
72. Chen K, Yan R, Xiang L, Xu K. Excitation spectral microscopy for highly multiplexed fluorescence imaging and quantitative biosensing. *Light Sci Appl*. 2021;10(1):97. doi:10.1038/s41377-021-00536-3
73. Guo Z, Poudel C, Sarfatis MC, et al. Highly multiplexed fluorescence microscopy with spectrally tunable semiconducting polymer dots. *Science Advances*. 2024;10(50):eadk8829. doi:10.1126/sciadv.adk8829
74. Mao C, Lee MY, Jhan JR, et al. Feature-rich covalent stains for super-resolution and cleared tissue fluorescence microscopy. *Sci Adv*. 2020;6(22):eaba4542. doi:10.1126/sciadv.aba4542
75. Lee MY, Mao C, Glaser AK, et al. Fluorescent labeling of abundant reactive entities (FLARE) for cleared-tissue and super-resolution microscopy. *Nat Protoc*. 2022;17(3):819-846. doi:10.1038/s41596-021-00667-2
76. Burghardt T, Hochapfel F, Salecker B, et al. Advanced electron microscopic techniques provide a deeper insight into the peculiar features of podocytes. *American Journal of Physiology-Renal*

Physiology. 2015;309(12):F1082-F1089. doi:10.1152/ajprenal.00338.2015

Chapter 2

Super-resolved Optical Imaging, Reconstruction, and Spatial Analysis of Whole Mouse Renal Glomeruli via GloMAP

2.1 Preface

As discussed in Chapter 1, kidney disease poses significant challenges to the public health system. Light microscopy and electron microscopy have long served as primary tools for understanding kidney morphology and pathological alterations. While powerful, each of these techniques comes with their own limitations. Prior work on studying the basic filtration unit of the kidney, the glomerulus, have largely focused on thin 2D sections and/or localized 3D sub-regions. However, the global relationships and spatial coordination among different glomerular compartments remain underexplored in the field.

In this chapter, I will present a novel pipeline that enables 3D imaging of the whole mouse renal glomeruli, segmentation and reconstruction of distinct glomerular components at nanometer resolution, and visualization and quantitative spatial analysis of the global structural relationships and alterations among them.

This was an ambitious project that began as a random idea and evolved into an entirely brand new area of research in our lab. I led these efforts from the beginning, including developing the pipelines for sample preparation, imaging, image segmentation, and analysis. Many members of the Vaughan group contributed to the segmentation effort, including Siying Chen, Tingxuan Liu, Pedro Vasquez, and Ziyu Guo. In the later stages, we collaborated with the

research group of Prof. Sheng Wang (UW Department of Computer Science and Engineering) who developed a machine learning model to generate initial segmentation predictions from our initial fully manual image segmentations, and this machine learning model provided good initial guesses that we could refine in ~10% the time it took for the fully manual segmentations. Yvonne Guan, a talented undergraduate student in the Vaughan group, and I developed a powerful algorithm to measure the basement membrane thickness on a global scale, an analysis that, to our knowledge, has never been achieved before. All authors listed below either reviewed or edited the manuscript.

This long journey, although challenging, has been incredibly rewarding, and I'm truly excited to see how a once-random idea has gradually matured into a fruitful and impactful project.

The following material in this chapter is reproduced with permission from:

Adilijiang Ali[1], Zixuan Liu[2], Kenan Ye[2], Yun Guan[1], Siying Chen[1], Tingxuan Liu[1], Ziyu Guo[1], Madeline K. Wong[1], Pedro Vasquez[1], Chetan Poudel[1], Benjamin C. Mustonen[1], Diana G. Eng[3], Jeffrey W. Pippin[3], Stuart J. Shankland[3], Sheng Wang[2], Joshua C. Vaughan[1,4]

1 Department of Chemistry, University of Washington, Seattle, Washington, USA

2 Paul G. Allen School of Computer Science & Engineering, University of Washington, Seattle, Washington, USA

3 Division of Nephrology, University of Washington, Seattle, Washington, USA

4 Department of Neurobiology and Biophysics, University of Washington, Seattle, Washington, USA

This work has been submitted for publication and is currently under review at *Kidney International* as:

Ali et al. "Super-resolved Optical Imaging, Reconstruction, and Spatial Analysis of Whole Mouse Renal Glomeruli via GloMAP."

All material in this chapter has been reformatted to conform to the style of this thesis.

2.2 Abstract

Renal glomeruli have traditionally been studied by micrometer-scale optical microscopy to interrogate overall physiology or molecular distributions and by nanoscale electron microscopy to interrogate ultrastructure. However, these techniques are limited by their focus on thin sections and specific regions, thereby restricting their capacity to evaluate whole glomeruli as holistic 3D functional units. To overcome this limitation, we developed a novel pipeline called GloMAP (Glomerulus Mapping and Analysis Pipeline) that combines super-resolution optical microscopy and computational analysis to create high-resolution (~100 nm) 3D models of whole mouse glomeruli. GloMAP integrates both manual and machine-learning-assisted segmentation to precisely annotate and quantify glomerular structures, including compartmental volumes, surface areas, membrane thickness distribution, and cellular morphometric properties. We demonstrated the versatility of this method by analyzing 24 glomeruli from healthy adult, aged, and model diseased mice. The pipeline's compatibility with commonly available optical microscopes and its potential to integrate molecular labeling and other super-resolution

techniques make it a scalable and versatile tool for advancing structural and molecular studies of whole intact glomeruli. GloMAP provides a foundation for broader adoption with other methods to study global compartmental relationships and pathological alterations in unprecedented detail.

2.3 Introduction

The primary function of renal glomeruli is to filter the blood, a task that requires an anatomically complex structure, including capillary loops, specialized resident cell types, and basement membranes. With age and disease, glomerular function declines, leading to impaired kidney function and broader health concerns. Our understanding of glomeruli and the kidney overall derives from microscopy studies in two distinct regimes. Optical microscopy provides micron-scale snapshots of overall physiology and distributions of key molecules (e.g., immune complexes) [1–9], and electron microscopy (EM) provides detailed nanometer-scale views of glomerular ultrastructure [10–14]. These traditional methods, while powerful, have faced several shortcomings. First, they are, by necessity, technically performed using different pieces of tissue and fixatives, preventing each method from being directly correlated. This has the potential to produce contradictory results. Second, high-resolution measurements of glomeruli are generally recorded using EM to measure two-dimensional thin sections at random angles or three-dimensional analysis of subregions (e.g., serial block face EM). This can create challenges with interpretation and sometimes overlook critical details. These limitations have constrained research and clinical practice to focus on specific subsets of structures or small regions of the glomerulus, rather than allowing for a comprehensive study of the entire glomerulus as a functioning unit.

To address these technical and knowledge gaps, we developed a novel pipeline called GloMAP (Glomerulus Mapping and Analysis Pipeline) that combines super-resolution optical microscopy and computational analysis to create high-resolution (~100 nm) 3D models of whole mouse glomeruli. GloMAP has two major advantages. First, it enables comprehensive annotation and quantification of all major structural components of glomeruli and renal corpuscle (i.e., Bowman's capsule basement membrane (BCBM), glomerular basement membrane (GBM), capillary lumen, and Bowman's space) as well as cell number and locations for all primary glomerular cell types (podocytes, mesangial cells (MCs), glomerular endothelial cells (GEnCs), and parietal epithelial cells (PECs)). Second, it provides a comprehensive workflow that enables a deeper understanding of global compartmental relationships and pathological alterations at a whole-glomerulus level, while being accessible for use in any laboratory without the need for specialized instruments or writing new, custom software.

2.4 Methods

All methods are detailed in **Chapter 3,** including mouse models, expansion microscopy, chemical and immunolabeling, optical imaging, segmentation, image registration, and analytical methods (expansion distortion analysis, membrane thickness analysis, cell type validation)

2.5 Data Sharing Statement

All imaging, model datasets, and detailed handling instructions are available on the SharePoint repository:

https://uwnetid.sharepoint.com/:f:/s/mouse_glomerulus_repository/EtSJNi1PmudNrhZMUdFtBD8BHWRcrg3x0NwSs7AZXTOJKA?e=NyKA9O

2.6 Results

2.6.1 Super-resolution, 3D fluorescence imaging of whole glomeruli

The key steps in GloMAP for whole glomerulus analysis are shown in **Figure 2.1**, including ~100 nm resolution imaging, segmentation, and analysis. The pipeline is based on expansion microscopy (ExM), a super-resolution microscopy technique that physically expands biological specimens with a swellable polymer so they can be imaged at high spatial resolution on a conventional microscope [15–17], and also employs a recently developed tri-color fluorescent stain called FLARE to label kidney structure. FLARE is a fluorescent analog of a combined hematoxylin and eosin (H&E) and periodic acid Schiff (PAS) stain [18,19] that labels nuclei (DNA), proteins (primary amines), and carbohydrates. Confocal microscopy was used to acquire three-channel data stacks of whole glomeruli within expanded mouse kidney tissue sections.

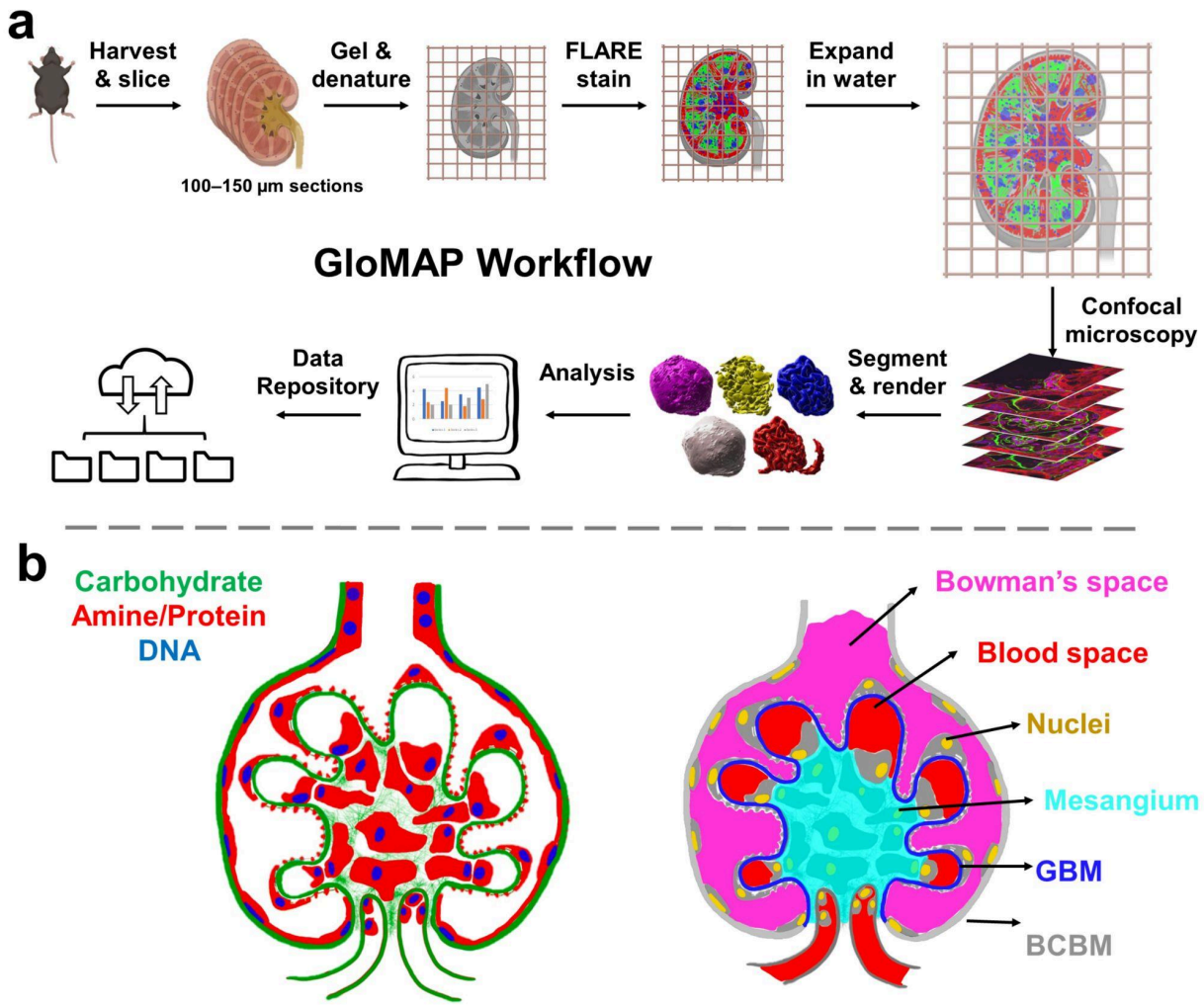

Figure 2.1. Schematic illustration of *a) the project workflow and b) segmented glomerular structures. In b), the left half shows an illustration of a FLARE-stained glomerulus, while the right half demonstrates how glomerular structures are represented based on the FLARE-stained sample. Bowman's space and the blood space are defined as empty spaces where there is no FLARE signal, with Bowman's space outside the GBM but within the Bowman's capsule and blood space inside the GBM. The BCBM and GBM are differentiated at the point where the carbohydrate signal at the periphery invaginates towards the inner glomerular space. The color schemes in b) are consistent with all raw data and segmented & reconstructed volumes in this report.*

The resulting serial optical sections of a FLARE-stained and expanded mouse glomerulus revealed diverse glomerular structures, including the carbohydrate-rich BCBM, GBM (**Figure 2.2a-h, Supplementary Movie 3.3.1-3**). Furthermore, finer structures, such as interdigitated podocyte foot processes (**Figure 2.2 i**), and nuclear chromatin organization (**Figure 2.2j**) were clearly visible.

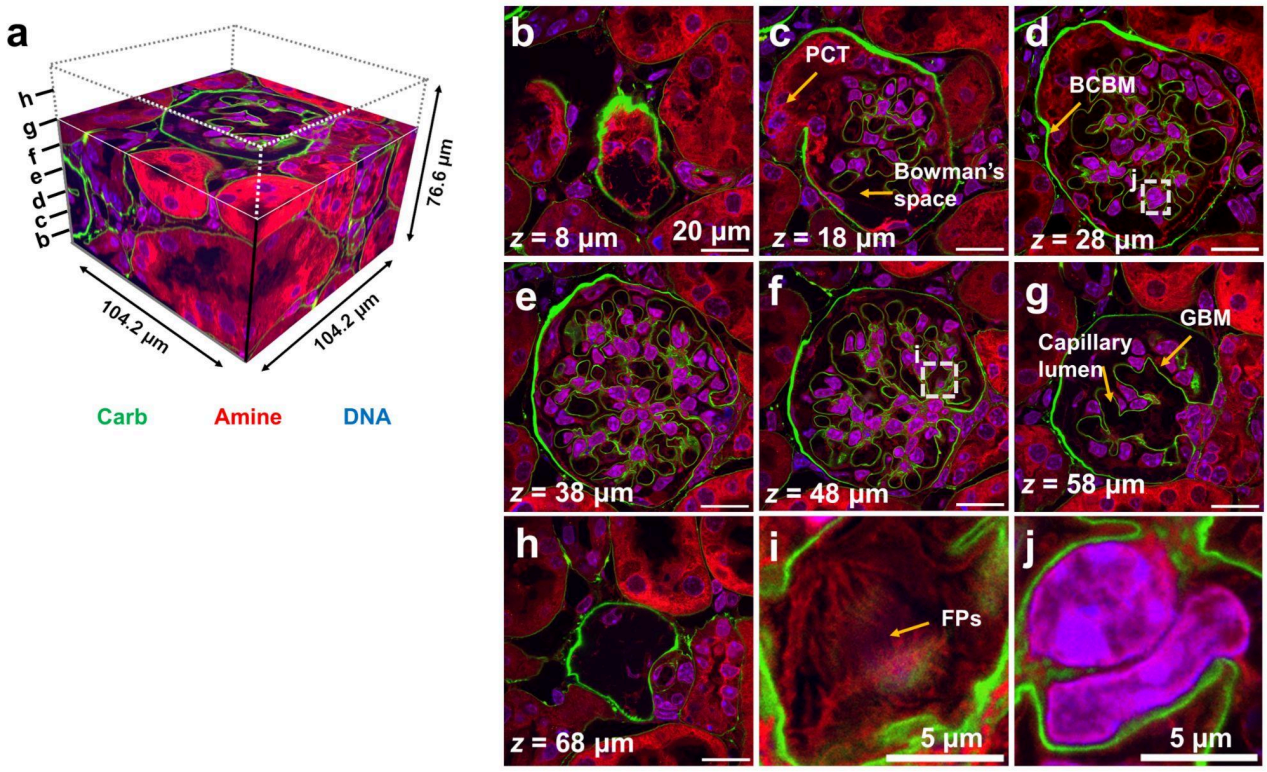

Figure 2.2. A FLARE-stained, hydrogel-expanded healthy adult cortical glomerulus. *a) Volumetric view and b–h) individual sections. Zoom-in views illustrate the level of detail attained, including resolving i) interdigitated podocyte foot processes and j) a pair of closely spaced nuclei within the mesangium. The z-position indicates the position of the optical section within the data stack. PCT = proximal convoluted tubule, FPs = foot processes. Green=carbohydrates; red=amine/protein, blue=nuclei. Scale bars and z-positions are in pre-expansion units.*

2.6.2 Segmentation and reconstruction of mouse glomeruli

The bulk of the labor of GloMAP was devoted to computational analysis of the confocal microscopy data to segment out the six key structural components from the volumetric data, including the BCBM, GBM, blood space, mesangium, Bowman's space, and four primary types of cell nuclei. Five initial glomeruli were manually segmented (~3–4 weeks each), and these segmentations were used to train a machine learning algorithm (**Supplementary Figure 3,1.1**) to make initial predictions for the six main structural components. Subsequent data sets were initially segmented using the trained model and then manually reviewed and corrected (**Supplementary Figure 3.1.2)**. This hybrid approach required considerably fewer human hours, at ~3 days per glomerulus, while achieving highly accurate and fully annotated datasets.

Each of the six structural components of the glomerulus was defined as illustrated in **Figure 2.1b** and segmented following the procedure detailed in the **Supplementary Methods**. Segmentation results for an example glomerulus are displayed in **Figure 2.3** and were subsequently processed for 3D reconstruction using Imaris. The representation of a single healthy adult cortical glomerulus is shown in **Figure 2.4**. The complete dataset, including both cortical and juxtamedullary glomeruli, is provided in **Supplementary Figure 3.1.3**.

Using the holistic models obtained by GloMAP, morphometric measurements such as the volumes, relative volume proportions, and the intact surface area of all key glomerular structures can be easily obtained (**Supplementary Figure 3.1.4, Supplementary Table 3.2.1, 3.2.2**).

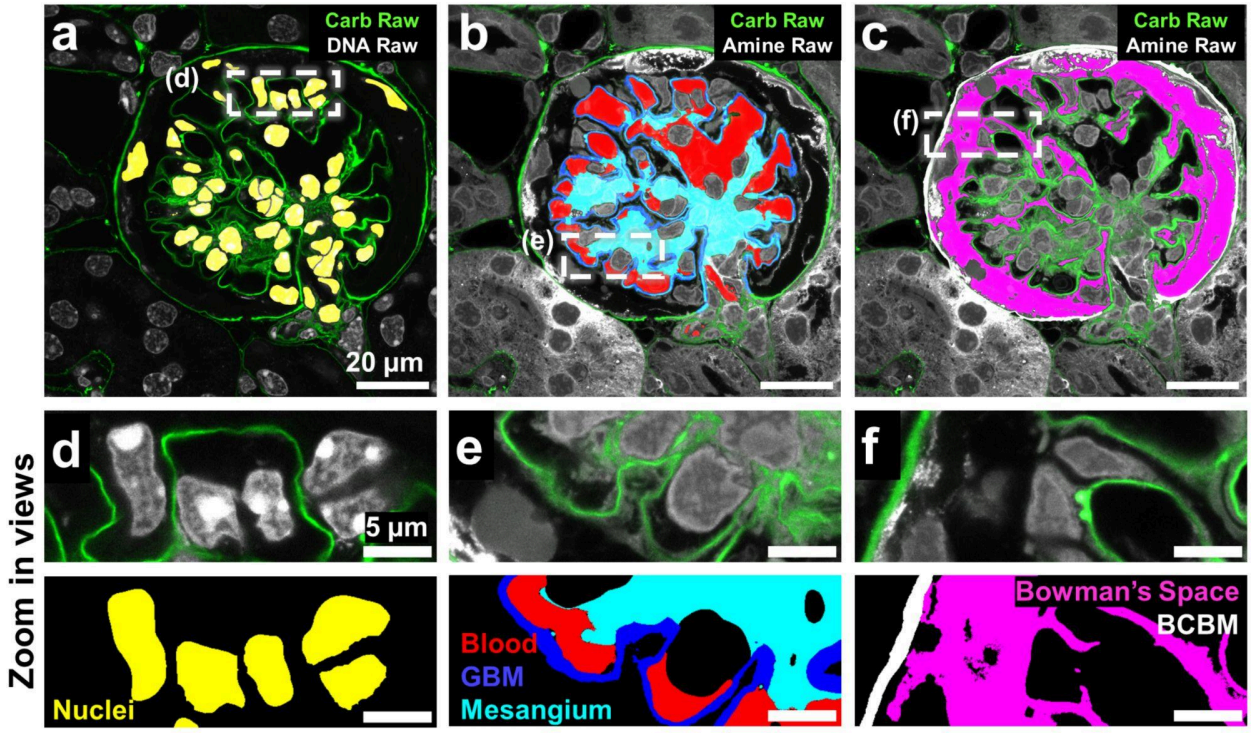

Figure 2.3. Segmentation of glomerulus data for a representative plane of data showing overlays of raw data with segmented structures for *a) Nuclei, b) Blood space, GBM, and mesangium, and c) BCBM and Bowman's space with zoom-in views of selected regions in d–f), illustrating the segmentation results. All scale bars are in pre-expansion units.*

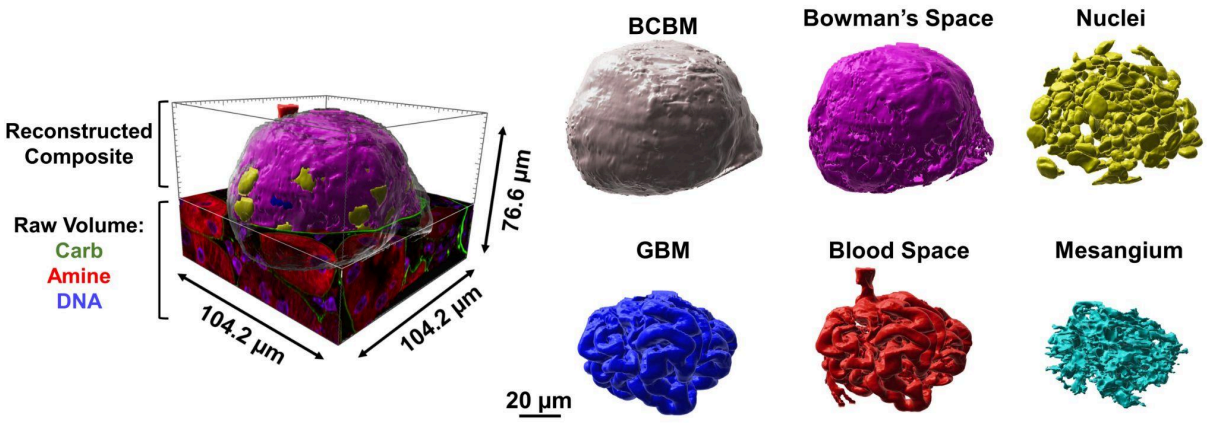

Figure 2.4. *An example 3D reconstruction of segmented structures for a cortical glomerulus from a healthy adult mouse. The scale bar and distances are in pre-expansion units.*

2.6.3 Glomerular cell type classification and cell morphometry

Detailed high-resolution views of the whole glomeruli enabled manual classification of all four principal glomerular cell types (PECs, podocytes, GEnCs, MCs) based on their nuclear shape and position relative to other glomerular structures **(Figure 2.5c, Supplementary Figure 3.1.5, Supplementary Movie 3.3.4**). Example data showing nucleus classification for all four cell types is presented in **Figure 2.5a-b.** e performed independent validation experiments using established cell-type-specific antibodies[20–25] against each cell type (**Figure 2.5d**, **Supplementary Figure 3.1.6**) and determined that the cell classification procedure was highly accurate for all cell types, with F1 scores of 0.92-0.99 (**Supplementary Table 3.2.3**). Although some immune

cells are also expected, the number was evidently small. By this means, detailed maps of all cell nucleus positions within the glomeruli were obtained. As a result, the numbers of individual cell types were quantified (**Table 2.1**), and morphological metrics such as nuclear volumes, density, and sphericity were measured (**Supplementary Figure 3.1.4, Supplementary Table 3.2.1, 3.2.2**).

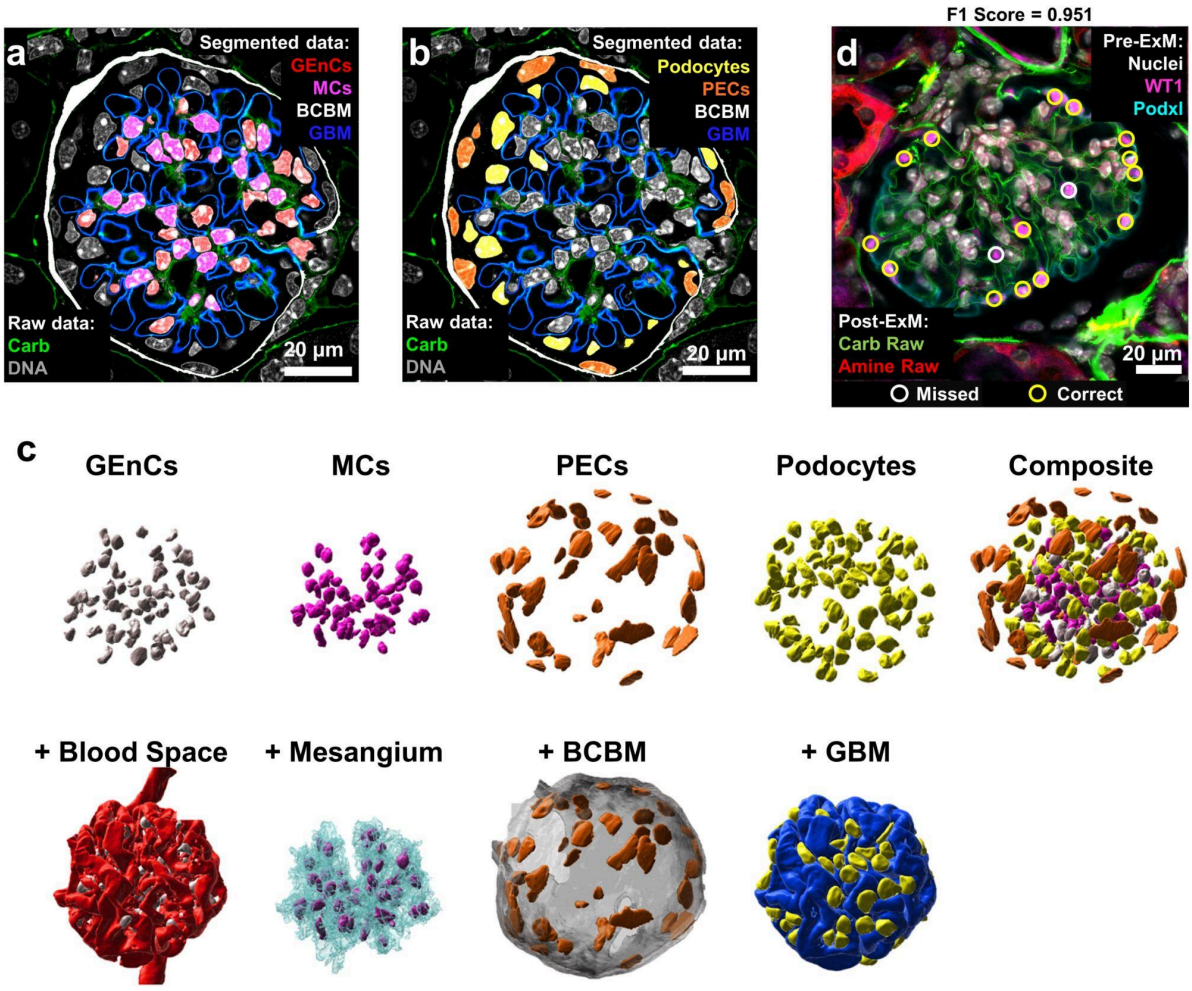

Figure 2.5. Cell type classification and validation. a-b) *Segmented GBM (blue) and BCBM (white) overlaid on raw carbohydrate channel (green) and raw nuclear channel (grey). Nuclei were designated as PEC, podocyte, GEnC, or MC after examining the 3D data near each nucleus, although they are often less clear in single-plane views. In a), GEnC and MC nuclei are shown positioned on the inner side of the GBM (blue), but GEnC nuclei (red) have substantial proximity to blood space, while MC nuclei are nearly surrounded by the carbohydrate signal (green) or GBM (blue). In b), PEC nuclei (orange) are flat nuclei at the BCBM inner surface (grey), whereas the podocyte nuclei (yellow) reside just outside the GBM (blue), facing the urinary space.* ***c)*** *An example healthy adult cortical glomerulus with reconstructed nuclei (top row) relative to key glomerular compartments (bottom row).* ***d)*** *Example cell type validation result for podocytes using pre- and post-ExM image registration (see also* ***Supplementary Figure S6****). Scale bars are shown in pre-expansion units.*

Table 2.1. The number & relative fraction of glomerular cell types are indicated as mean (± standard deviation).

	Adult (2-10 m.o.) ***n*=16**		**Aged (27-29 m.o.)** ***n*=3**		**D14 FSGS (3-3.5 m.o.)** ***n*=5**	
	Count	Fraction	Count	Fraction	Count	Fraction
Glomerular Endothelial Cell	98 (±30)	28.2% (±3.5%)	152 (±53)	35.2% (±6.1%)	89 (±19)	28.8% (±1.3%)
Mesangial Cell	85 (±36)	24.1% (±3.6%)	133 (±44)	31.0% (±5.4%)	82 (±19)	26.9% (±5.3%)
Podocyte	99 (±21)	29.4% (±5.7%)	91 (±15)	22.5% (±7.1%)	46 (±31)	13.8% (±7.4%)
Parietal Epithelial Cell	63 (±19)	18.3% (±4.0)	46 (±2)	11.3% (±2.4%)	95 (±24)	30.5% (±5.0%)
Total	345 (±90)	100%	423 (±87)	100%	312 (±70)	100%

2.6.4 Limitations of 2D and the necessity of 3D

The reconstruction of whole glomeruli enabled a comprehensive analysis of glomerular properties, overcoming the limitations of traditional approaches that rely on sampling small regions or thin sections at random angles. These methods often suffer from the loss of critical spatial information (**Figure 2.6a**), particularly when identifying pathological alterations. Depending on the slicing position, the same glomerulus can exhibit a range of morphologies, from normal to severely damaged (**Figure 2.6b, c**), potentially leading to misclassification of its diseased state.

This limitation underscores the necessity of a 3D reconstruction pipeline capable of capturing the full spatial complexity of glomerular structures, ensuring accurate characterization and analysis across diverse pathological conditions.

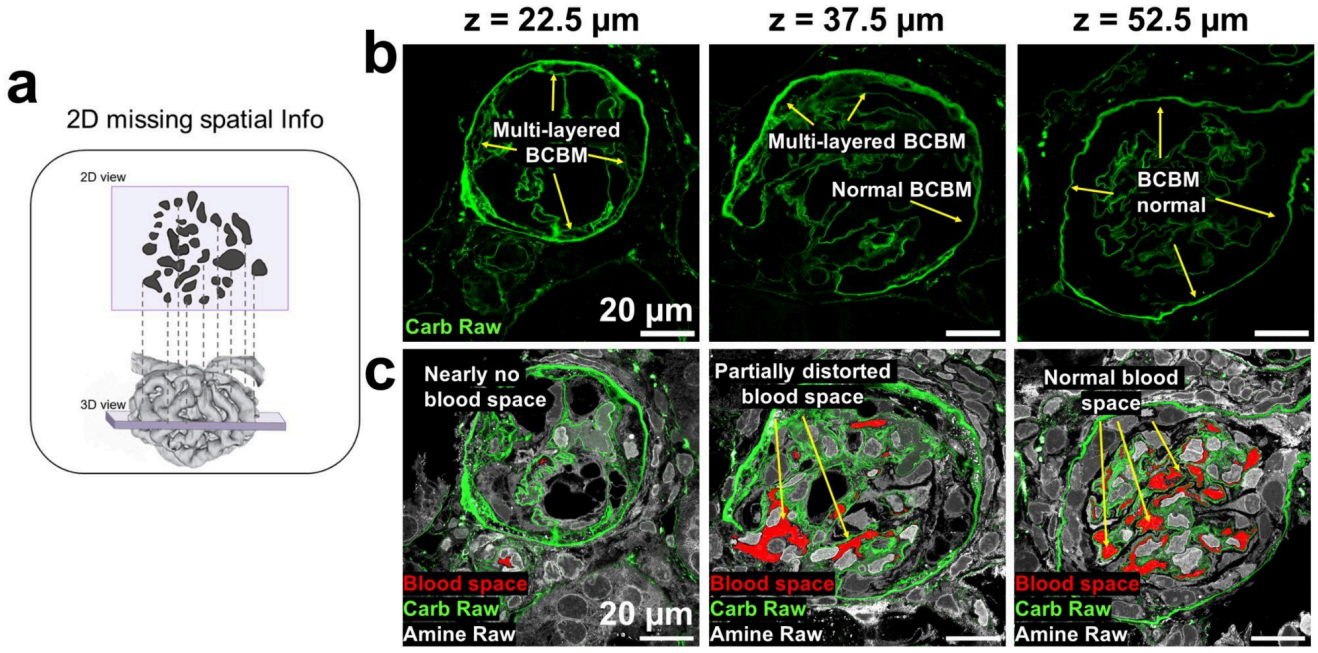

Figure 2.6. The effect of slicing position on determining the pathological state of a glomerulus with FSGS. ***a)*** *An illustrative diagram comparing 2D and 3D views, showing how spatial information of capillary space is lost when viewing individual 2D slices instead of an intact 3D view.* ***b)*** *Different frames from the same glomerulus, equally spaced along the z-axis, showing how the appearance of the BCBM varies across slices. Depending on the slicing position, the BCBM exhibits different pathological patterns, even within the same glomerulus.* ***c)*** *Frames from the same glomerulus and same z-axis positions, demonstrating how slicing positions can have different pathological patterns of the glomerular blood space. All scale bars are in pre-expansion units.*

2.6.5 Advancing from 2D to 3D: comprehensive 3D analysis of glomerular structures

2D methods often fail to capture spatial and segmental variations (**Figure 2.6**), and we used GloMAP on aged and experimental focal segmental glomerulosclerosis (FSGS) mice as a technical (not biological) proof of concept (**Supplementary Figure 3.1.3**).

In a representative glomerulus with FSGS, one region exhibits multilayered basement membrane formation, while the opposing region remains monolayered, illustrating localized basement membrane remodeling (**Figure 2.7a**). This segmental pathology was further reflected in the distortion of blood spaces on the affected side, in contrast to the relatively intact architecture on the unaffected side (**Figure 2.7b**). The mesangium also displayed region-specific alterations, appearing enlarged and swollen in the pathological region compared to the more jagged and branched structure elsewhere (**Figure 2.7c**). Segmental differences extend to cell-type-specific changes. Podocytes show a higher density observed on the side with basement membrane distortion (**Figure 2.7d**), and PECs are positioned further from the basement membrane, migrating toward the inner glomerular space in these regions (**Figure 2.7e**). These findings highlight the value of 3D reconstructions for comprehensive analysis of glomerular pathology, enabling the identification of subtle, localized structural differences that could be missed using traditional 2D approaches.

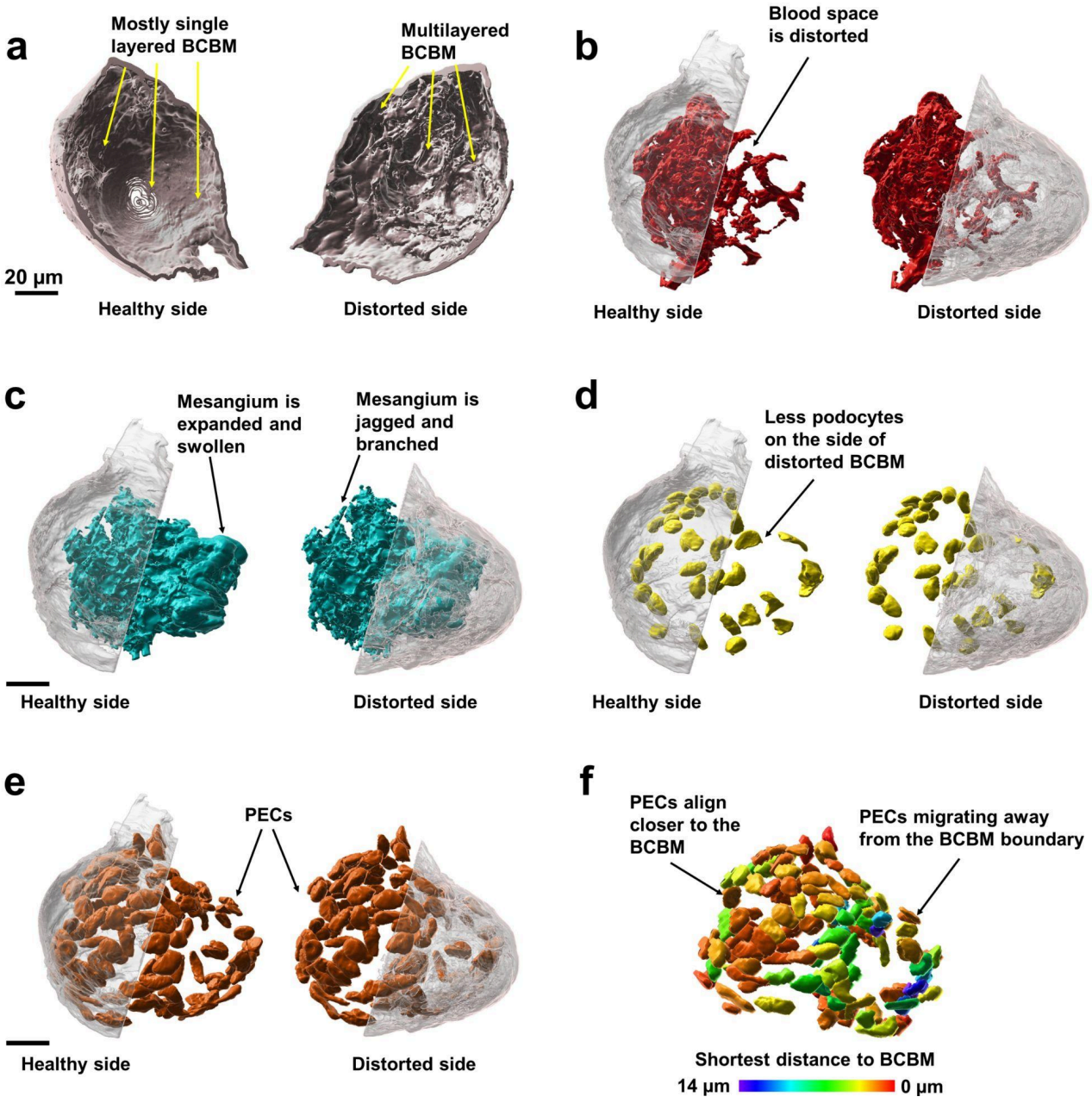
a
Mostly single layered BCBM
Multilayered BCBM
20 µm
Healthy side
Distorted side
b
Blood space is distorted
Healthy side
Distorted side
c
Mesangium is expanded and swollen
Mesangium is jagged and branched
Healthy side
Distorted side
d
Less podocytes on the side of distorted BCBM
Healthy side
Distorted side
e
PECs
Healthy side
Distorted side
f
PECs align closer to the BCBM
PECs migrating away from the BCBM boundary
Shortest distance to BCBM
14 µm
0 µm

Figure 2.7. Complete 3D models reveal segmental pathological patterns in the same glomerulus with FSGS, as Figure 6b-c. *a) The BCBM 3D model highlights distinct pathological features: one half exhibits multilayered basement membrane formation, while the other half remains monolayered. b) Blood volume is significantly lower on the side of the glomerulus with the multilayered BCBM, whereas the opposite side remains relatively intact. c) The mesangium shows segmental changes, appearing enlarged and blobby on the side with the distorted BCBM, in contrast to the branch-like structure on the unaffected side. (d) A higher density of podocytes is detected on the side with the distorted BCBM, reflecting segmental differences in podocyte distribution. e) PECs are positioned further from the BCBM on the distorted side, indicating migration towards the inner glomerular space. f) Measurement of the distance between the PECs to the BCBM. Distances are measured as the shortest distance of the nuclei to the outer boundary of the BCBM. All scale bars and color bars are presented in pre-expansion units*

2.6.6 Pathological alterations in aging, and experimental FSGS

Next, we used aged and FSGS glomeruli to demonstrate the sensitivity of GloMAP to detect subtle structural and cellular changes. These well-defined models provide an accurate representation of glomerular morphology, capturing trends such as mesangial volume expansion in aged kidneys, accompanied by reduced blood and Bowman's space (**Supplementary Figure 3.1.4**), consistent with prior reports[26].

Pathological features such as increased BCBM volume, surface area, and PEC activation (**Figure 2.7e, f**) in FSGS were observed, aligning with established disease mechanisms. Our validated cell type analysis revealed changes in cell count in aged and FSGS mice (**Table 2.1**)as well as an increase in average podocyte nuclear volume, consistent with podocyte hypertrophy in settings of reduced podocyte counts[26] (**Table 2.1**, **Supplementary Figure 3.1.4f**). Interestingly, the nuclear volumes of all four cell types were also substantially larger in aged samples compared to young healthy kidneys.

We used our super-resolution reconstructions to perform a global analysis of the thickness distribution of both the BCBM and the GBM for the first time in whole glomeruli. Although both the BCBM and GBM became thicker for aged or FSGS glomeruli, the BCBM tended to thicken in distinct patches (sclerotic regions), while the GBM thickened more globally and without an obvious pattern (**Figure 2.8**).

A full list of quantified measurements is provided in **Supplementary Figure 3.1.4 and Tables 3.1 and 3.2**. While further validation with larger and more controlled sample sizes is necessary, these findings highlight the robustness of our pipeline in detecting even slight structural variations across conditions, providing a more holistic understanding of the progression of pathological changes in glomeruli.

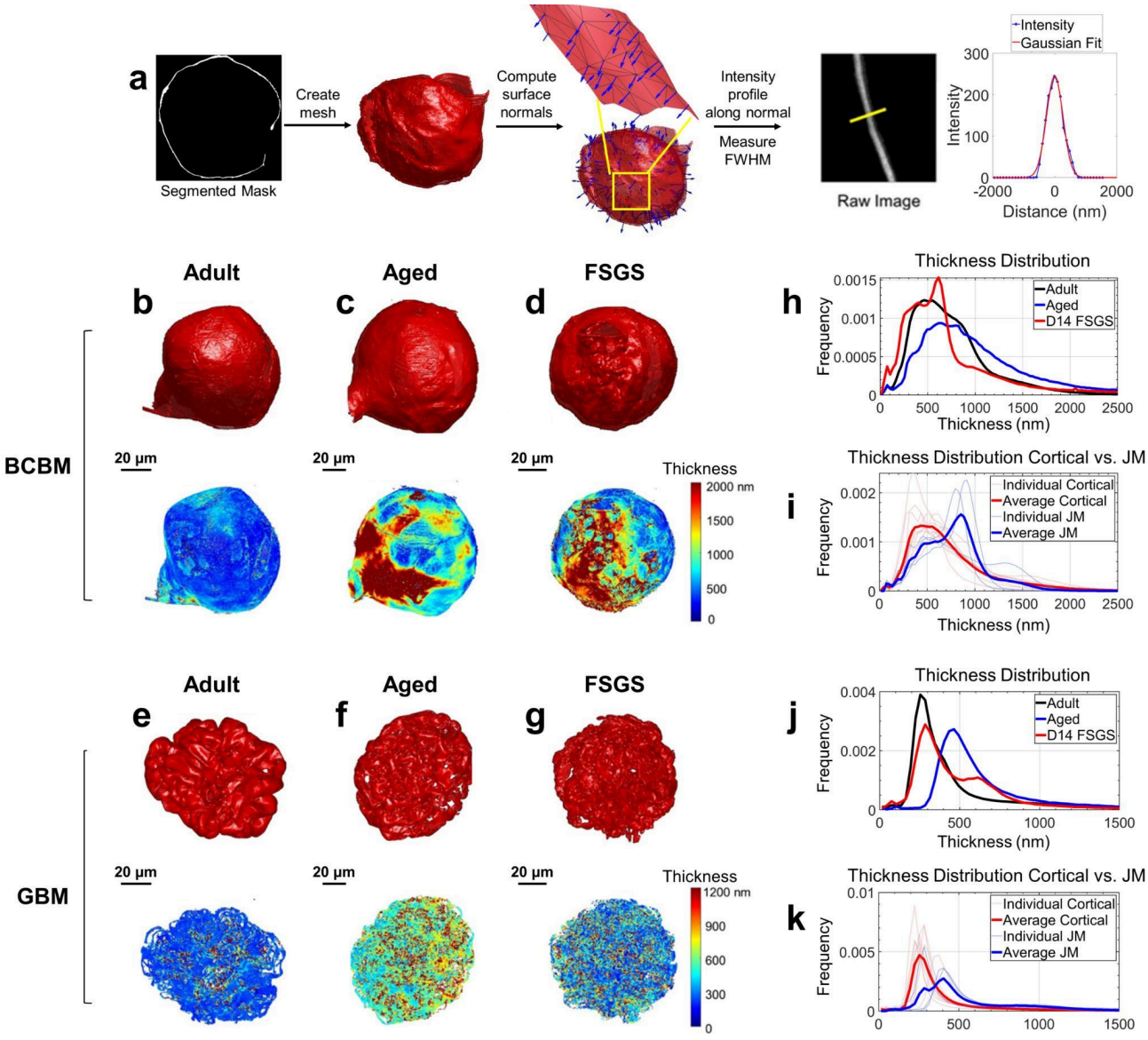
a
Segmented Mask
Create mesh
Compute surface normals
Intensity profile along normal
Measure FWHM
Raw Image
Intensity
Gaussian Fit
Intensity
Distance (nm)
Adult
Aged
FSGS
b
c
d
BCBM
20 µm
Thickness
2000 nm
1500
1000
500
0
h
Thickness Distribution
Frequency
Thickness (nm)
Adult
Aged
D14 FSGS
i
Thickness Distribution Cortical vs. JM
Individual Cortical
Average Cortical
Individual JM
Average JM
e
f
g
GBM
1200 nm
900
600
300
j
k

Figure 2.8. Thickness distribution analysis of the Bowman's capsule basement membrane (BCBM) and glomerular basement membrane (GBM). *a) Schematic illustration of the thickness analysis process: Meshes were generated from segmented masks of the BCBM and GBM. Surface normal vectors were calculated for each mesh face, and intensity profiles were extracted along these normal vectors from the raw image data. A Gaussian function was fitted to each profile, and thickness was estimated using the full width at half maximum (FWHM) of the Gaussian curve.* ***b-d)*** *3D meshes and corresponding thickness maps of BCBM of:* ***b)*** *adult (2–10 m.o.),* ***c)*** *aged (27–29 m.o.), and* ***d)*** *D14 FSGS (3-3.5 m.o.) glomerulus. In aged mice, BCBM is thickened in patches near the junction of the Bowman's capsule and proximal convoluted tubule. In FSGS mice, BCBM displayed notably thicker regions at sites of pathological changes, where PECs formed a layered BCBM.* ***e)*** *Line profiles of the thickness distribution of BCBM for adult (n=12), aged (n=3), and D14 FSGS (n=5) glomeruli. The average thickness of the BCBM in healthy adult, aged, and experimental FSGS glomeruli was 689 ± 113 nm, 938 ± 142 nm, and 518 ± 89 nm, respectively.* ***f)*** *Average and individual thickness distributions of adult cortical vs. JM BCBM, showing variability observed among individual glomeruli and their location within the kidney.* ***g-i)*** *3D meshes and corresponding thickness maps of GBM:* ***g)*** *adult,* ***h)*** *aged, and* ***i)*** *D14 FSGS glomerulus.* ***j)*** *Line profiles of the thickness distributions of GBM for adult, aged, and D14 FSGS glomeruli. No clear patterns of variation in GBM thickness were observed across the aged or experimental FSGS glomeruli.* ***k)*** *Average and individual thickness distributions of adult cortical vs. JM BCBM, showing variability observed among individual glomeruli and their location within the kidney. The GBM thickness measurements were restricted to points that had surface normal <10 degrees deviating from the xy plane (****Supplementary Figure S7****). The distributions in* ***e, f, j,*** *and* ***k*** *are normalized to have the same area under the curve. All scale bars*

and distances are shown in pre-expansion units.

2.7 Discussion

We developed a novel pipeline called GloMAP for super-resolution 3D imaging, reconstruction, and analysis of whole glomeruli, enabling comprehensive characterization of glomerular compartments in healthy young adults, aged, and experimental FSGS mice. In the current methodological study, we did not address biological questions as this was beyond the scope of the project. Our approach included classification of cell types, quantification of compartmental volumes, surface areas, and relative fractions, as well as detailed morphometric analyses of glomerular cells that included volume, sphericity, and density. Notably, we measured GBM and BCBM thicknesses across whole glomeruli for the first time, rather than in selective regions. This analysis uncovered distinctive BCBM thickening patterns in aged and experimental FSGS mice.

GloMAP provides a unique approach for reconstructing and analyzing whole glomeruli in 3D to comprehensively characterize compartments and cells. In contrast to methods such as NIPOKA PEMP analysis[6] and other super-resolution studies focused on podocyte foot process or slit diaphragms[2], GloMAP is able to capture global relationships among all glomerular compartments, which is crucial in segmental pathological alterations. Electron microscopy (EM) array tomography, as demonstrated by Miyaki et al.[27], offers exquisite ultrastructural detail at even higher spatial resolution for whole-glomeruli but requires lengthy sample processing and highly specialized expertise. GloMAP achieves ~100 nm resolution with simpler and more

accessible protocols. Furthermore, we have produced publicly accessible 3D models for 24 glomeruli, and we include novel analyses such as whole-glomerulus studies of GBM and Bowman's capsule thickness patterns. Future studies will be expanded to include global foot process distributions by incorporating immunofluorescence labeling of podocin, further bridging the gap between structural and molecular insights.

The current study was not intended to address specific biological questions, but rather to report a novel method called GloMAP. We recognize some weaknesses in the current study. First, the higher cell counts observed compared to previous reports may, at least in part, reflect our limited sampling that doesn't capture the extent of glomerular heterogeneity across the entire kidney, although the higher spatial resolution of GloMAP may do a better job at distinguishing closely positioned nuclei. Second, we did not focus on the presence of immune cells. Third, because the tissue section thickness (100–150 μm) used was only slightly larger than the typical size of the glomeruli (70–80 μm), it is possible that we may have biased toward imaging smaller glomeruli; future biologically-focused studies would benefit from using thicker sections to minimize this potential bias. Fourth, producing these unique whole-glomerulus models is labor-intensive at present, requiring around 3 days of human effort per glomerulus even with machine-learning assistance. Future improvements in GloMAP, such as developing a refined algorithm trained on larger datasets, would expedite this process, and spatial analysis focused on specific compartments or cell types could also be performed in a much shorter time than the full analysis.

In summary, we introduce GloMAP as a novel pipeline to image, reconstruct, and

quantify the glomeruli as functional units. By enabling whole-glomerulus 3D analysis, our approach provides a novel tool for capturing the full structural complexity and functional relationship within the glomerulus, providing insights into both normal and pathological conditions without the need for specialized instruments. Furthermore, GloMAP opens doors for integration with other modeling approaches, such as running realistic fluid mechanics simulations or bioprinting physiologically accurate artificial glomeruli. By providing a detailed framework, GloMAP will enable avenues for a deeper understanding of glomerular structure and biology and will drive innovations in nephrology.

2.8 Reference

1. Unnersjö-Jess D, Scott L, Sevilla SZ, Patrakka J, Blom H, Brismar H. Confocal super-resolution imaging of the glomerular filtration barrier enabled by tissue expansion. *Kidney International*. 2018;93(4):1008-1013. doi:10.1016/j.kint.2017.09.019
2. Unnersjö-Jess D, Scott L, Blom H, Brismar H. Super-resolution stimulated emission depletion imaging of slit diaphragm proteins in optically cleared kidney tissue. *Kidney International*. 2016;89(1):243-247. doi:10.1038/ki.2015.308
3. Pullman JM, Nylk J, Campbell EC, Gunn-Moore FJ, Prystowsky MB, Dholakia K. Visualization of podocyte substructure with structured illumination microscopy (SIM): a new approach to nephrotic disease. *Biomed Opt Express, BOE*. 2016;7(2):302-311. doi:10.1364/BOE.7.000302
4. Chozinski TJ, Mao C, Halpern AR, et al. Volumetric, Nanoscale Optical Imaging of Mouse and Human Kidney via Expansion Microscopy. *Scientific Reports*. 2018;8(1). doi:10.1038/s41598-018-28694-2
5. Klingberg A, Hasenberg A, Ludwig-Portugall I, et al. Fully Automated Evaluation of Total Glomerular Number and Capillary Tuft Size in Nephritic Kidneys Using Lightsheet Microscopy. *Journal of the American Society of Nephrology*. 2017;28(2):452-459. doi:10.1681/ASN.2016020232
6. Siegerist F, Ribback S, Dombrowski F, et al. Structured illumination microscopy and automatized image processing as a rapid diagnostic tool for podocyte effacement. *Sci Rep*. 2017;7(1):11473. doi:10.1038/s41598-017-11553-x
7. Suleiman H, Zhang L, Roth R, et al. Nanoscale protein architecture of the kidney glomerular basement membrane. McNeill H, ed. *eLife*. 2013;2:e01149. doi:10.7554/eLife.01149
8. Østergaard MV, Sembach FE, Skytte JL, et al. Automated Image Analyses of Glomerular Hypertrophy in a Mouse Model of Diabetic Nephropathy. *Kidney360*. 2020;1(6):469-479.

doi:10.34067/KID.0001272019

9. Puelles VG, Wolde JW van der, Schulze KE, et al. Validation of a Three-Dimensional Method for Counting and Sizing Podocytes in Whole Glomeruli. *JASN*. 2016;27(10):3093-3104. doi:10.1681/ASN.2015121340
10. Terasaki M, Brunson JC, Sardi J. Analysis of the three dimensional structure of the kidney glomerulus capillary network. *Sci Rep*. 2020;10(1):20334. doi:10.1038/s41598-020-77211-x
11. Ichimura K, Miyazaki N, Sadayama S, et al. Three-dimensional architecture of podocytes revealed by block-face scanning electron microscopy. *Sci Rep*. 2015;5(1):8993. doi:10.1038/srep08993
12. Burghardt T, Hochapfel F, Salecker B, et al. Advanced electron microscopic techniques provide a deeper insight into the peculiar features of podocytes. *American Journal of Physiology-Renal Physiology*. 2015;309(12):F1082-F1089. doi:10.1152/ajprenal.00338.2015
13. Randles MJ, Collinson S, Starborg T, et al. Three-dimensional electron microscopy reveals the evolution of glomerular barrier injury. *Sci Rep*. 2016;6(1):35068. doi:10.1038/srep35068
14. Honda K, Takaki T, Kang D. Recent advances in electron microscopy for the diagnosis and research of glomerular diseases. *Kidney Res Clin Pract*. 2023;42(2):155-165. doi:10.23876/j.krcp.21.270
15. Chen F, Tillberg PW, Boyden ES. Expansion microscopy. *Science*. 2015;347(6221):543-548. doi:10.1126/science.1260088
16. Chozinski TJ, Halpern AR, Okawa H, et al. Expansion microscopy with conventional antibodies and fluorescent proteins. *Nature Methods*. 2016;13(6):485-488. doi:10.1038/nmeth.3833
17. Ku T, Swaney J, Park JY, et al. Multiplexed and scalable super-resolution imaging of three-dimensional protein localization in size-adjustable tissues. *Nature Biotechnology*. 2016;34:973-981. doi:10.1038/nbt.3641
18. Mao C, Lee MY, Jhan JR, et al. Feature-rich covalent stains for super-resolution and cleared

tissue fluorescence microscopy. *Sci Adv*. 2020;6(22):eaba4542. doi:10.1126/sciadv.aba4542

19. Lee MY, Mao C, Glaser AK, et al. Fluorescent labeling of abundant reactive entities (FLARE) for cleared-tissue and super-resolution microscopy. *Nat Protoc*. 2022;17(3):819-846. doi:10.1038/s41596-021-00667-2
20. Zimmerman SE, Hiremath C, Tsunezumi J, Yang Z, Finney B, Marciano DK. Nephronectin Regulates Mesangial Cell Adhesion and Behavior in Glomeruli. *Journal of the American Society of Nephrology*. 2018;29(4):1128-1140. doi:10.1681/ASN.2017070752
21. Steglich A, Kessel F, Hickmann L, et al. Renin cells with defective Gsα/cAMP signaling contribute to renal endothelial damage. *Pflugers Arch - Eur J Physiol*. 2019;471(9):1205-1217. doi:10.1007/s00424-019-02298-9
22. Ohse T, Chang AM, Pippin JW, et al. A new function for parietal epithelial cells: a second glomerular barrier. *American Journal of Physiology-Renal Physiology*. 2009;297(6):F1566-F1574. doi:10.1152/ajprenal.00214.2009
23. Roeder SS, Barnes TJ, Lee JS, et al. Activated ERK1/2 increases CD44 in glomerular parietal epithelial cells leading to matrix expansion. *Kidney International*. 2017;91(4):896-913. doi:10.1016/j.kint.2016.10.015
24. Kaverina NV, Eng DG, Largent AD, et al. WT1 Is Necessary for the Proliferation and Migration of Cells of Renin Lineage Following Kidney Podocyte Depletion. *Stem Cell Reports*. 2017;9(4):1152-1166. doi:10.1016/j.stemcr.2017.08.020
25. Kaverina NV, Kadoya H, Eng DG, et al. Tracking the stochastic fate of cells of the renin lineage after podocyte depletion using multicolor reporters and intravital imaging. Dryer SE, ed. *PLOS ONE*. 2017;12(3):e0173891. doi:10.1371/journal.pone.0173891
26. Hodgin JB, Bitzer M, Wickman L, et al. Glomerular Aging and Focal Global Glomerulosclerosis: A Podometric Perspective. *Journal of the American Society of Nephrology*. 2015;26(12):3162. doi:10.1681/ASN.2014080752

27. Miyaki T, Honma N, Kawasaki Y, et al. Ultrastructural analysis of whole glomerulus using array tomography. *Journal of Cell Science*. Published online August 22, 2024:jcs.262154. doi:10.1242/jcs.262154

Chapter 3

Supplementary Materials for Chapter 2

Super-resolution Optical Imaging, Reconstruction, and Spatial Analysis of Whole Mouse Glomeruli via GloMAP

Adilijiang Ali[1], Zixuan Liu[2], Kenan Ye[2], Yun Guan[1], Siying Chen[1], Tingxuan Liu[1], Ziyu Guo[1], Madeline K. Wong[1], Pedro Vasquez[1], Chetan Poudel[1], Benjamin C. Mustonen[1], Diana G. Eng[3], Jeffrey W. Pippin[3], Stuart J. Shankland[3], Sheng Wang[2], Joshua C. Vaughan[1,4]

1 Department of Chemistry, University of Washington, Seattle, Washington, USA

2 Paul G. Allen School of Computer Science & Engineering, University of Washington, Seattle, Washington, USA

3 Division of Nephrology, University of Washington, Seattle, Washington, USA

4 Department of Neurobiology and Biophysics, University of Washington, Seattle, Washington, USA

*Corresponding authors. Email: jcv2@uw.edu.

This Chapter includes:

Supplementary Figure 3.1.1-7

Supplementary Tables 3.2.1-3

Supplementary Movie 3.3.1-4

Supplementary Methods

Supplementary References

3.1 Supplementary Figures

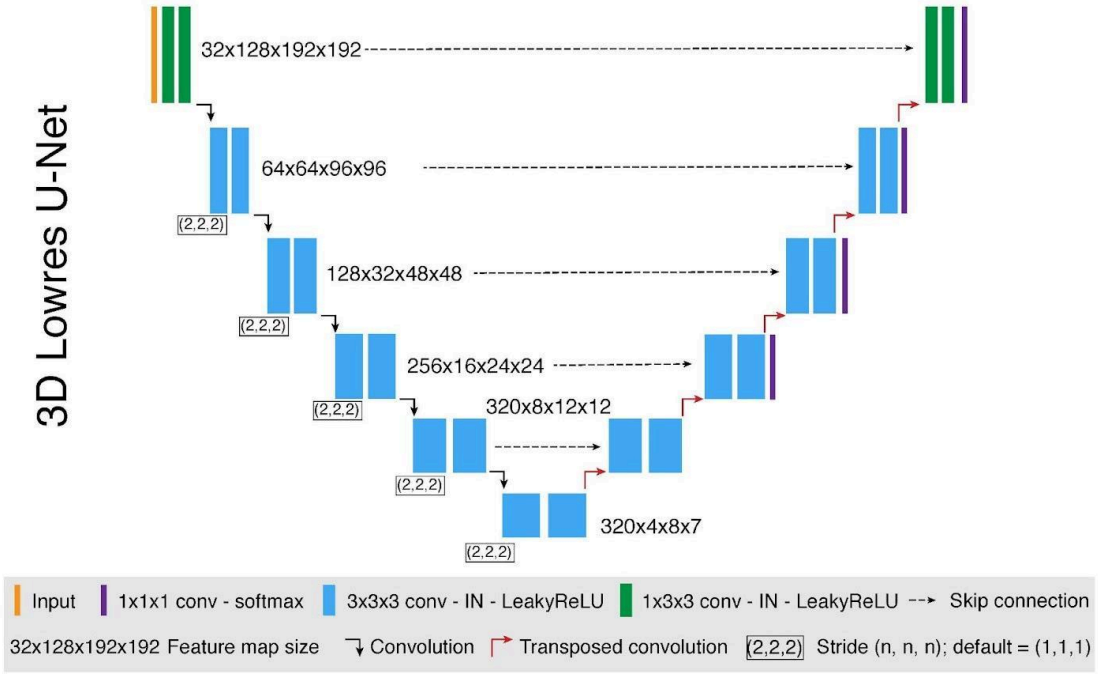

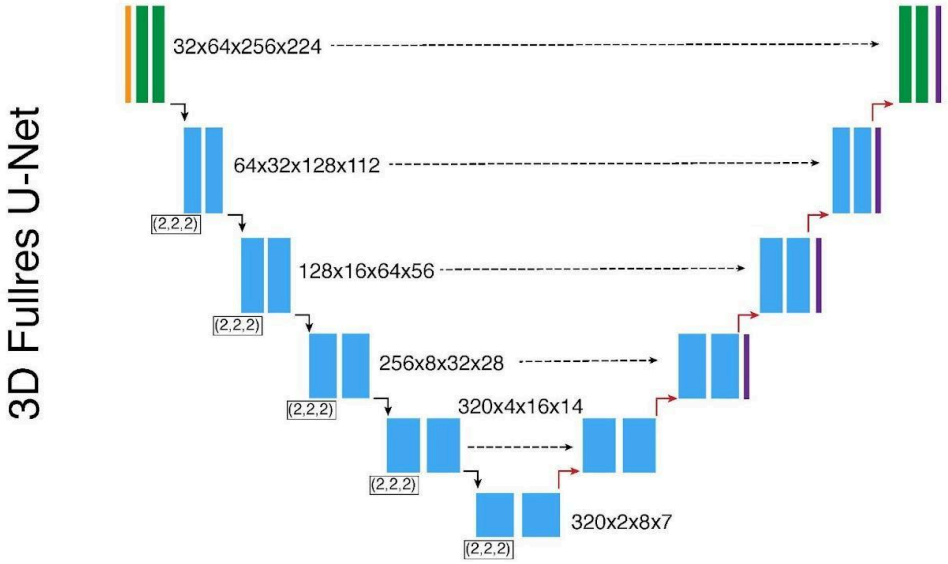

Supplementary Figure 3.1.1 Illustration of deep learning-based semi-automated neural network structure. *The deep learning framework is composed of a low-resolution 3D CNN-based U-Net and a full-resolution 3D CNN-based U-Net. The low-resolution network takes downsampled glomerular volumes as input to efficiently capture global contextual information and output coarse predicted segmentation masks. The full-resolution network then takes both the full-sized glomerular volumes and the coarse segmentation masks as input and outputs the refined predicted segmentation masks.*

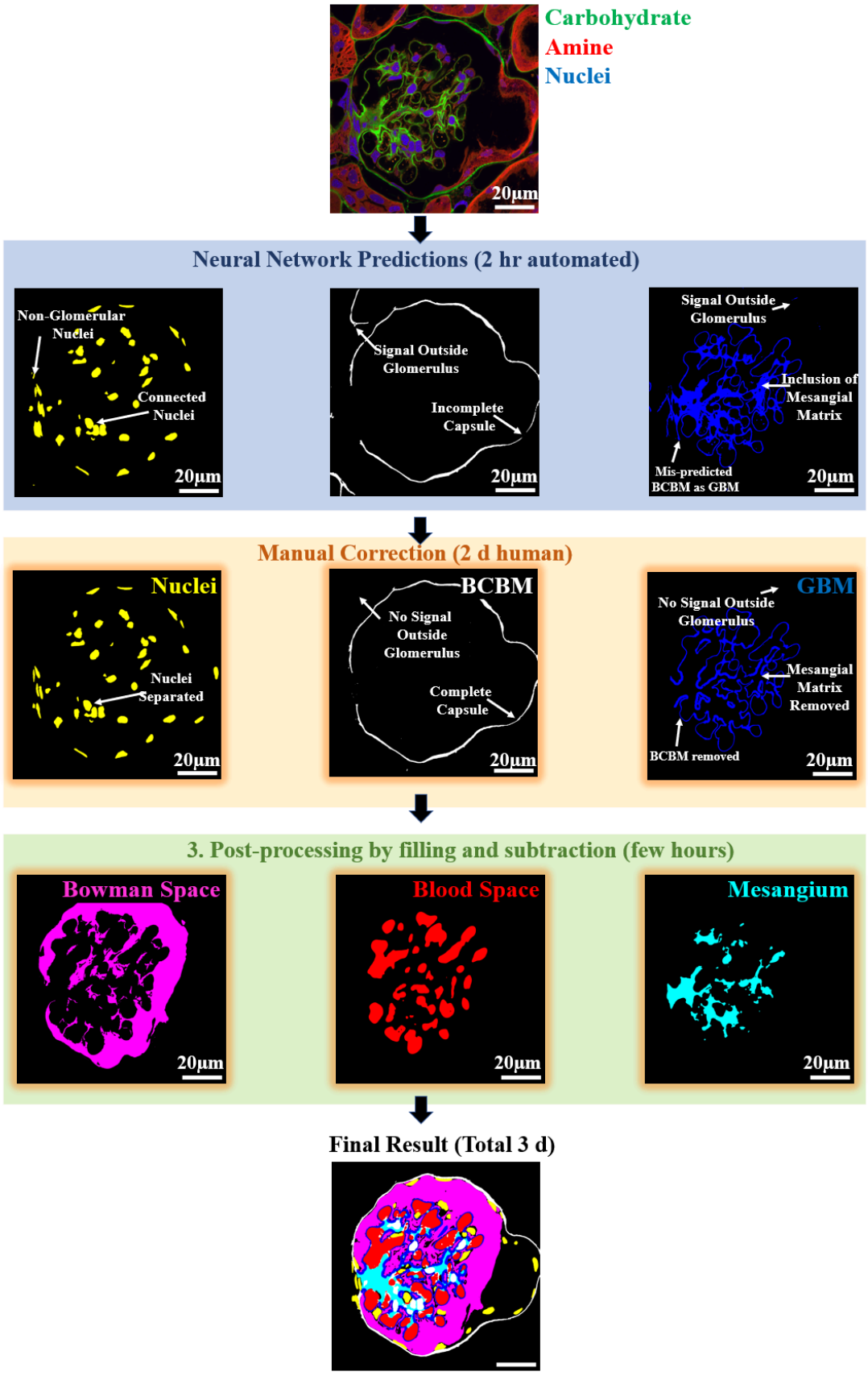
Carbohydrate
Amine
Nuclei
20µm
Neural Network Predictions (2 hr automated)
Non-Glomerular Nuclei
Connected Nuclei
20µm
Signal Outside Glomerulus
Incomplete Capsule
20µm
Signal Outside Glomerulus
Inclusion of Mesangial Matrix
Mis-predicted BCBM as GBM
20µm
Manual Correction (2 d human)
Nuclei
Nuclei Separated
20µm
BCBM
No Signal Outside Glomerulus
Complete Capsule
20µm
GBM
No Signal Outside Glomerulus
Mesangial Matrix Removed
BCBM removed
20µm
3. Post-processing by filling and subtraction (few hours)
Bowman Space
20µm
Blood Space
20µm
Mesangium
20µm
Final Result (Total 3 d)

Supplementary Figure 3.1.2. Workflow for semiautomated glomerular structure segmentation using our pipeline. *Step 1) Initial Prediction: Neural networks generate preliminary predictions for nuclei, BCBM, and GBM. Step 2) Manual Correction: manually refine any inaccuracies identified in Step 1. Step 3) Post-processing: Bowman's space, blood space, and the mesangium are segmented using simple filling and subtraction operations in ImageJ. Detailed procedures are provided in the Supplementary Methods. All scale bars are presented in pre-expansion units.*

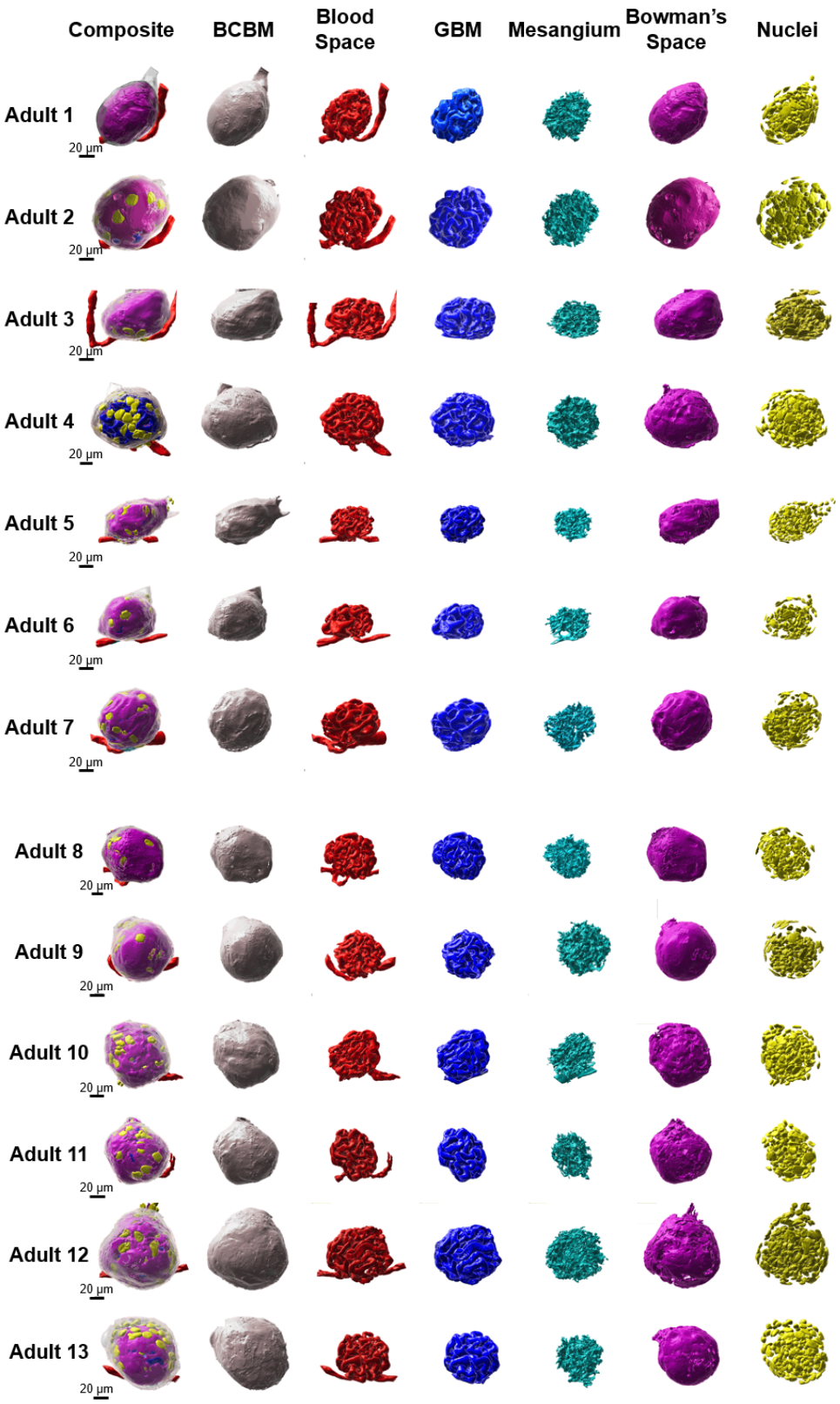
Composite
BCBM
Blood Space
GBM
Mesangium
Bowman's Space
Nuclei
Adult 1
Adult 2
Adult 3
Adult 4
Adult 5
Adult 6
Adult 7
Adult 8
Adult 9
Adult 10
Adult 11
Adult 12
Adult 13
20 µm

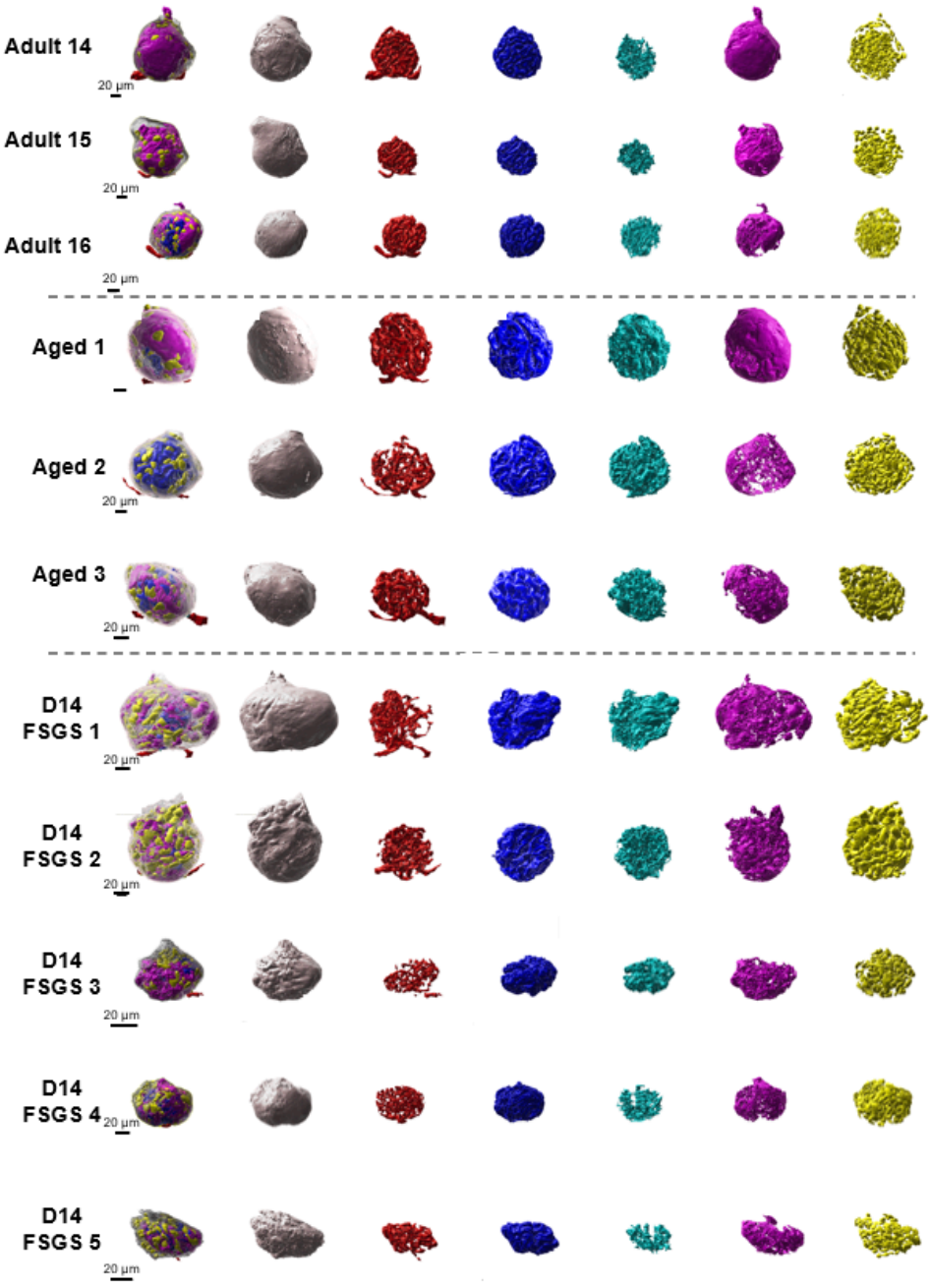
Adult 14
20 µm
Adult 15
20 µm
Adult 16
20 µm
Aged 1
Aged 2
20 µm
Aged 3
20 µm
D14
FSGS 1
20 µm
D14
FSGS 2
20 µm
D14
FSGS 3
20 µm
D14
FSGS 4
20 µm
D14
FSGS 5
20 µm

Supplementary Figure 3.1.3. Collection of all reconstructed healthy adult, aged, and FSGS mouse glomeruli from this work. *All the glomeruli are oriented such that the capillary pole is at the bottom and the urinary pole is at the top. BCBM = grey, Blood space = red, GBM = blue, Mesangium = cyan, Bowman's Space = magenta, Nuclei = yellow. Scale bars are shown in pre-expansion units.*

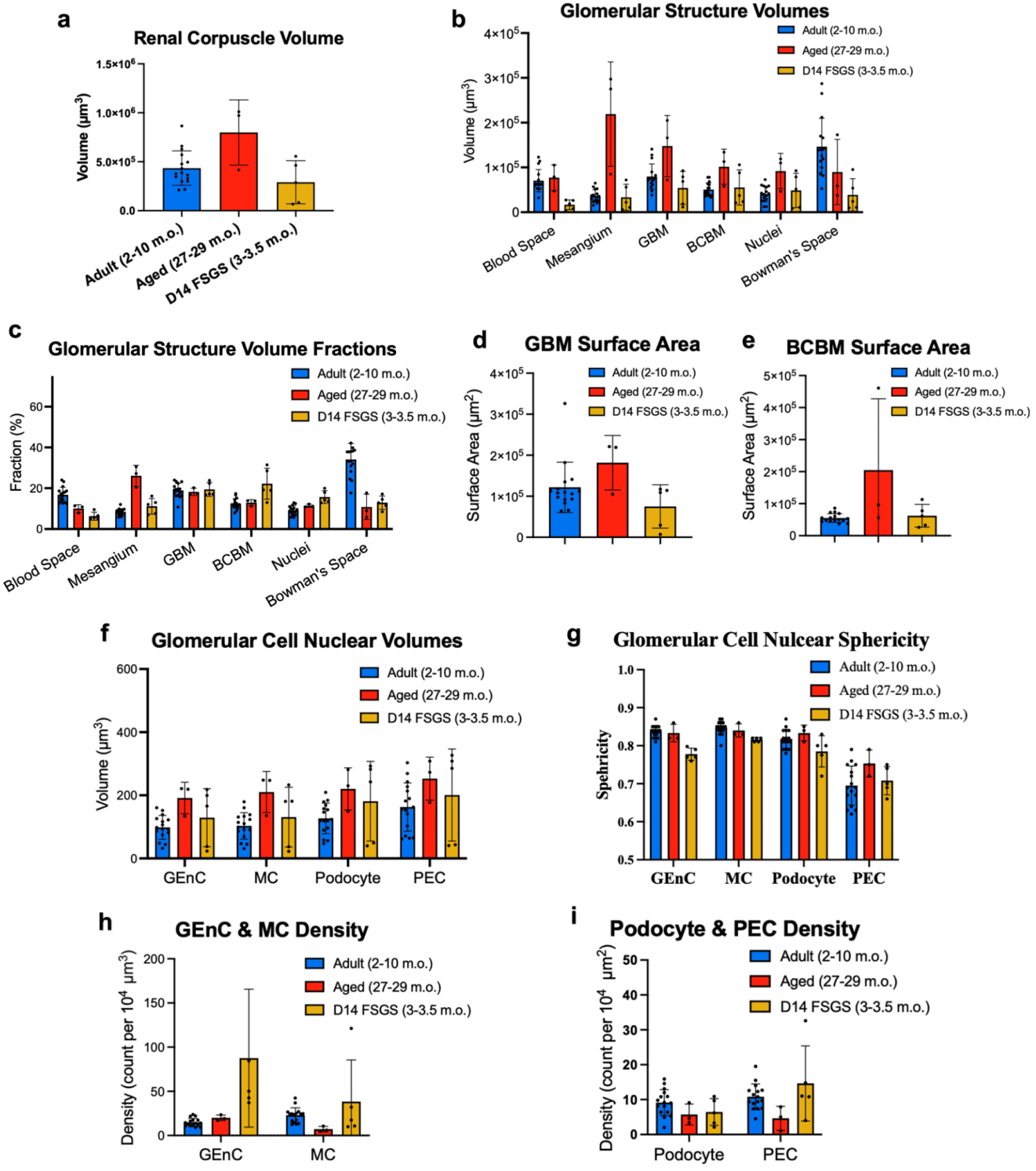
a
Renal Corpuscle Volume
Volume (µm³)
1.5×10⁶
1.0×10⁶
5.0×10⁵
0.0
Adult (2-10 m.o.)
Aged (27-29 m.o.)
D14 FSGS (3-3.5 m.o.)
b
Glomerular Structure Volumes
Volume (µm³)
4×10⁵
3×10⁵
2×10⁵
1×10⁵
0
Adult (2-10 m.o.)
Aged (27-29 m.o.)
D14 FSGS (3-3.5 m.o.)
Blood Space
Mesangium
GBM
BCBM
Nuclei
Bowman's Space
c
Glomerular Structure Volume Fractions
Fraction (%)
60
40
20
0
Adult (2-10 m.o.)
Aged (27-29 m.o.)
D14 FSGS (3-3.5 m.o.)
Blood Space
Mesangium
GBM
BCBM
Nuclei
Bowman's Space
d
GBM Surface Area
Surface Area (µm²)
4×10⁵
3×10⁵
2×10⁵
1×10⁵
0
Adult (2-10 m.o.)
Aged (27-29 m.o.)
D14 FSGS (3-3.5 m.o.)
e
BCBM Surface Area
Surface Area (µm²)
5×10⁵
4×10⁵
3×10⁵
2×10⁵
1×10⁵
0
Adult (2-10 m.o.)
Aged (27-29 m.o.)
D14 FSGS (3-3.5 m.o.)
f
Glomerular Cell Nuclear Volumes
Volume (µm³)
600
400
200
0
Adult (2-10 m.o.)
Aged (27-29 m.o.)
D14 FSGS (3-3.5 m.o.)
GEnC
MC
Podocyte
PEC
g
Glomerular Cell Nulcear Sphericity
Spehricity
1.0
0.9
0.8
0.7
0.6
0.5
Adult (2-10 m.o.)
Aged (27-29 m.o.)
D14 FSGS (3-3.5 m.o.)
GEnC
MC
Podocyte
PEC
h
GEnC & MC Density
Density (count per 10⁴ µm³)
200
150
100
50
0
Adult (2-10 m.o.)
Aged (27-29 m.o.)
D14 FSGS (3-3.5 m.o.)
GEnC
MC
i
Podocyte & PEC Density
Density (count per 10⁴ µm²)
50
40
30
20
10
0
Adult (2-10 m.o.)
Aged (27-29 m.o.)
D14 FSGS (3-3.5 m.o.)
Podocyte
PEC

Supplementary Figure 3.1.4. Whole glomerulus level quantitation of glomerular structures. *a) Renal corpuscle volumes. b) volumes of individual structures. c) Relative proportions of glomerular structure volume to the renal corpuscle volume. d) GBM surface area. e) BCBM surface area. All the measurements are in pre-expansion units. In all panels, n=16 for adults, n=3 for aged, and n=5 for d14 FSGS.*

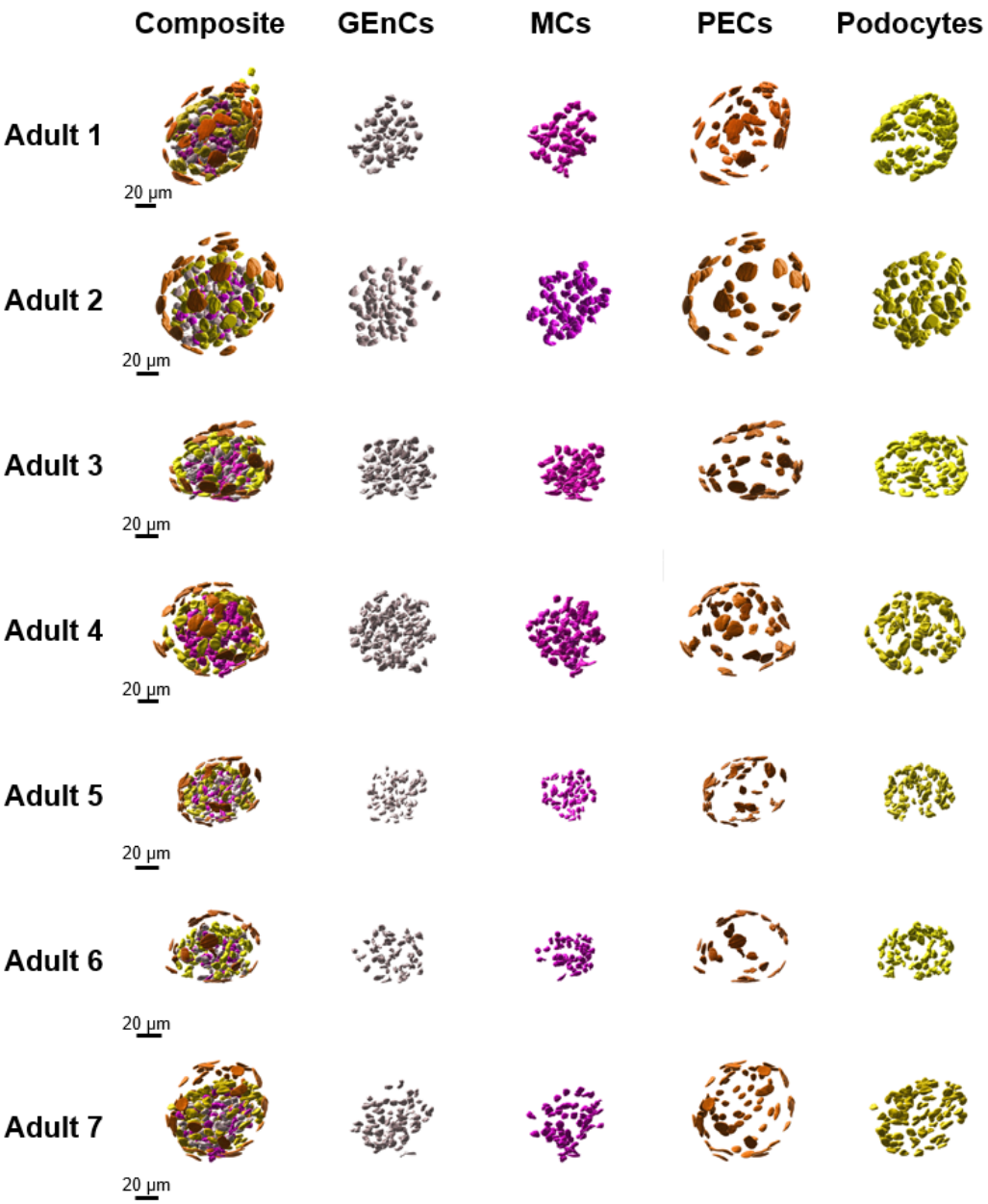
Composite
GEnCs
MCs
PECs
Podocytes
Adult 1
Adult 2
Adult 3
Adult 4
Adult 5
Adult 6
Adult 7
20 µm

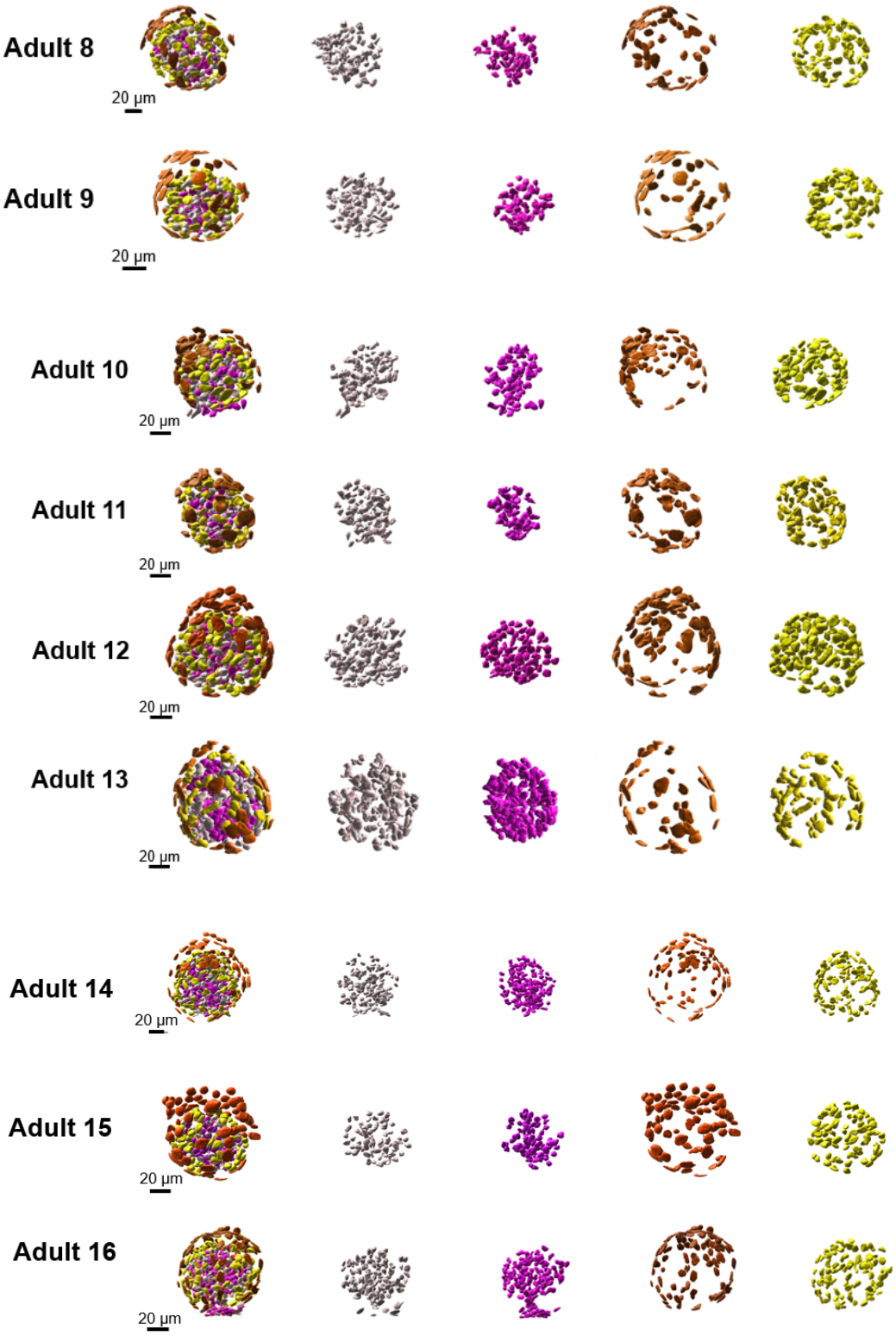
Adult 8
20 µm
Adult 9
20 µm
Adult 10
20 µm
Adult 11
20 µm
Adult 12
20 µm
Adult 13
20 µm
Adult 14
20 µm
Adult 15
20 µm
Adult 16
20 µm

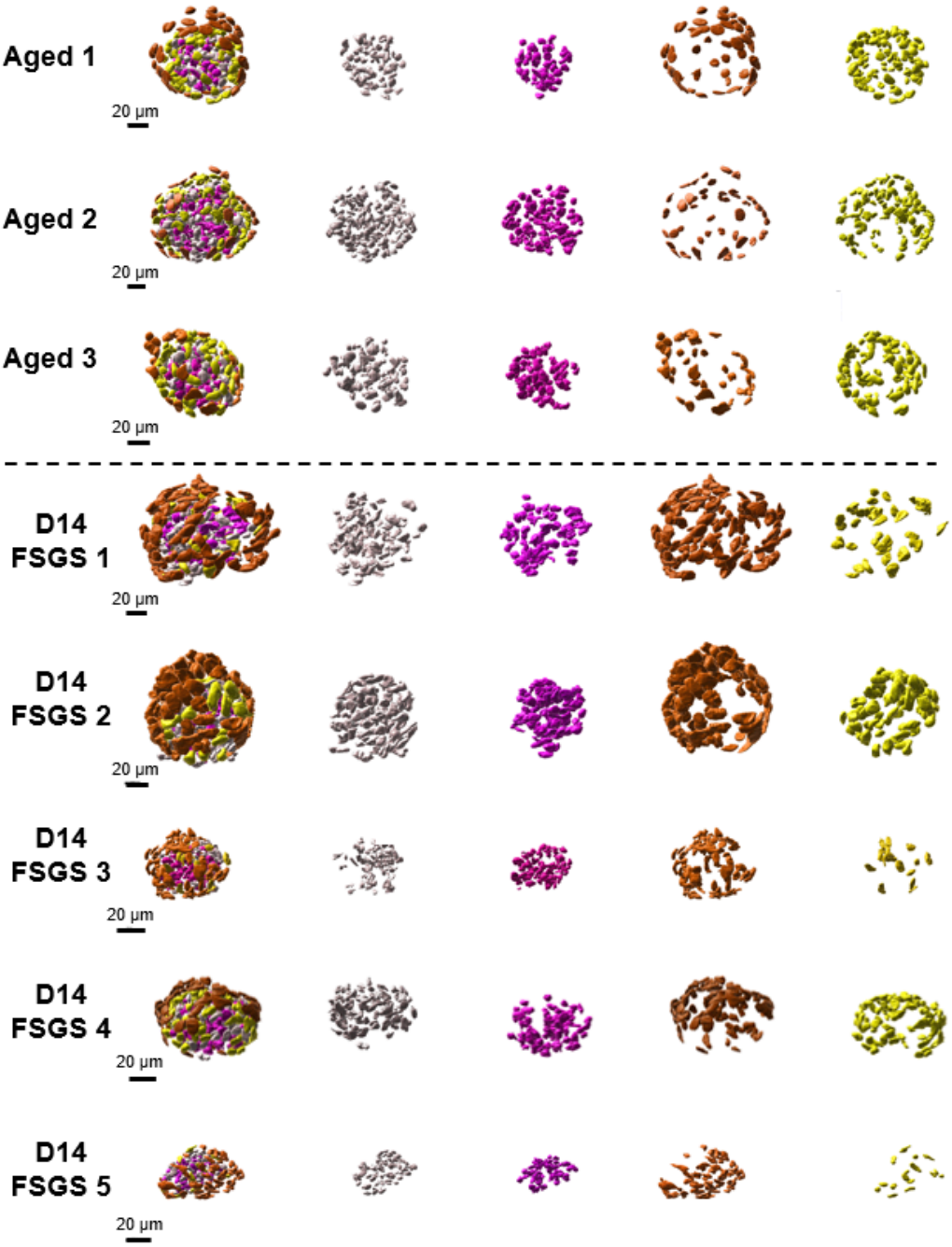

Supplementary Figure 3.1.5. Collection of all reconstructed and classified cell nuclei for healthy adult, aged, and FSGS mouse glomeruli. *All the images are positioned in the exact same orientation as the glomerular structures in Supplementary Figure 4. GEnCs = grey, MCs = magenta, PECs = blue, Podocytes = yellow. Scale bars are shown in pre-expansion units.*

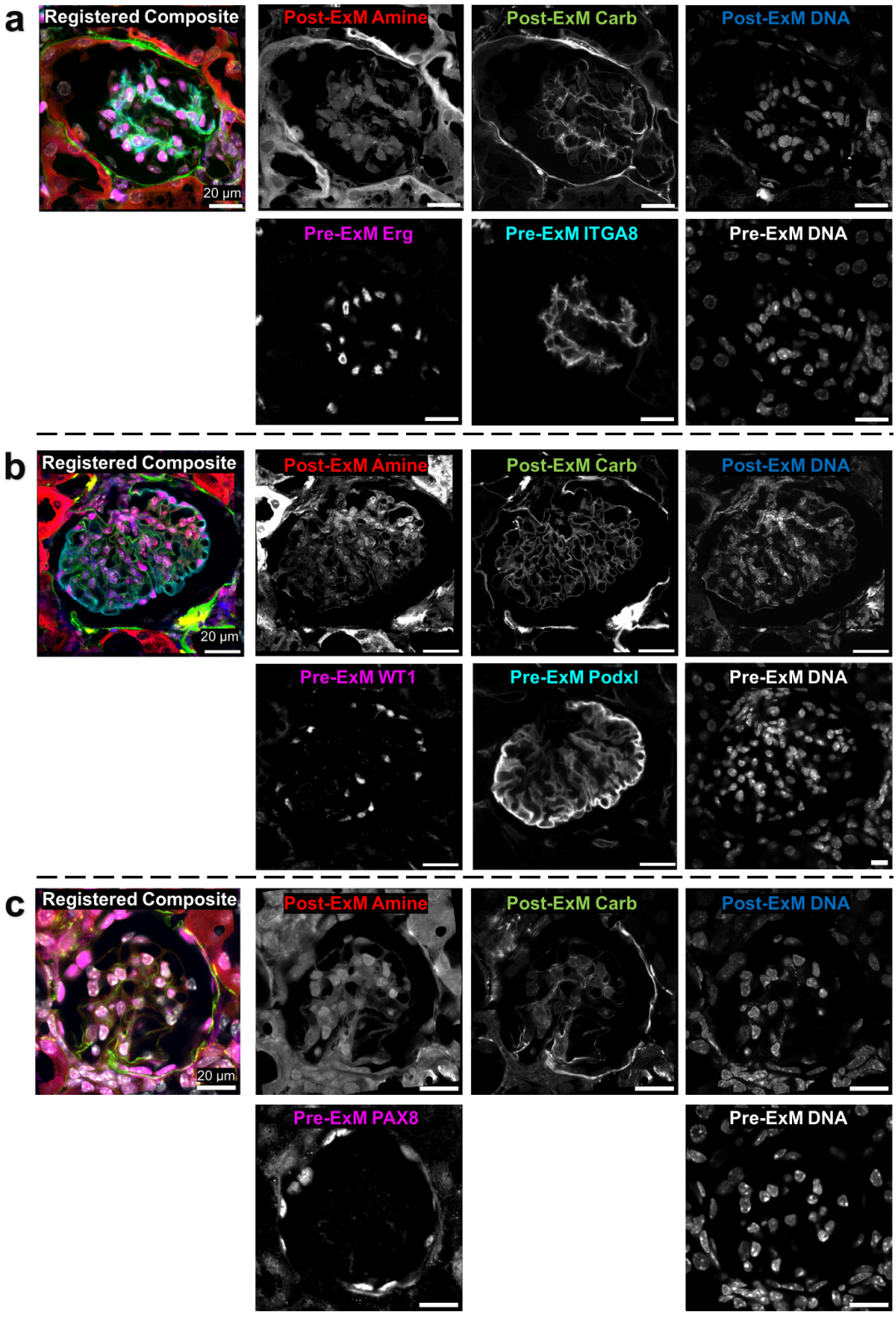
a
Registered Composite
20 µm
Post-ExM Amine
Post-ExM Carb
Post-ExM DNA
Pre-ExM Erg
Pre-ExM ITGA8
Pre-ExM DNA
b
Registered Composite
20 µm
Post-ExM Amine
Post-ExM Carb
Post-ExM DNA
Pre-ExM WT1
Pre-ExM Podxl
Pre-ExM DNA
c
Registered Composite
20 µm
Post-ExM Amine
Post-ExM Carb
Post-ExM DNA
Pre-ExM PAX8
Pre-ExM DNA

Supplementary Figure 3.1.6. Validation of cell type classification using pre-ExM immunostains and post-ExM FLARE stains. *Mouse kidney tissue sections were initially stained with markers for specific cell types: a) glomerular endothelial cells (Erg) and mesangial cells (ITGA8), b) podocytes (WT1, Podxl), and c) parietal epithelial cells (PAX8). Glomeruli in the unexpanded sections were imaged in a first round. The sections were then processed with expansion microscopy and FLARE staining (which chemically bleaches the prior immunostain signals), and then the same glomeruli were imaged in a second round. Finally, the two rounds of images were registered to produce a single composite data set. Based on this validation methodology, the precision and recall for ExM/FLARE-based cell type classification were determined to be 91-100% (see also* ***Supplementary Table 3.2.3****). All scale bars are shown in pre-expansion units.*

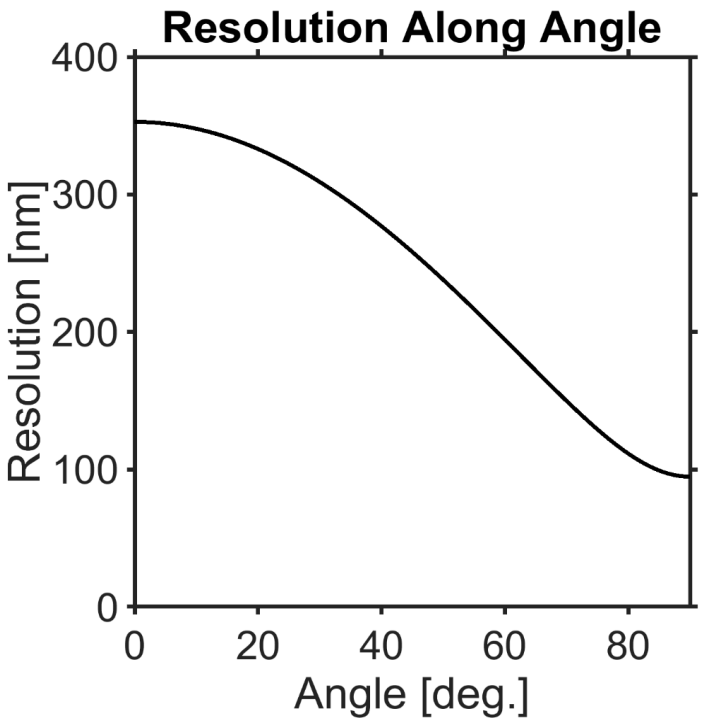

Supplementary Figure 3.1.7. Simulation of spatial resolution as a function of angle relative to the ± z dimension. *The angle ranges from 0 to 90 degrees, where 90 degrees represents alignment parallel to the xy-plane, where the expansion-corrected lateral spatial resolution is ~100 nm, and 0 degrees represents alignment along the ± z-axis, where the expansion-corrected axial spatial resolution is ~350 nm. The plot illustrates how the spatial resolution varies between the lateral and axial dimensions due to anisotropy in the point spread function (PSF).*

3.2 Supplementary Tables

Supplementary Table 3.2.1. Average measurements of individual glomerular structures and cell types. All volumes or surface areas are presented in pre-expansion units. Values are presented as mean ± standard deviation. Adult: n=16, Aged: n=3, D14 FSGS n=5.

	Adult (2-10 m.o.)	Aged (27-29 m.o.)	D14 FSGS (3-3.5 m.o.)
$V_{Blood}(\times 10^4\ \mu m^3)$	7.19 (±2.69)	7.73 (±2.91)	1.67 (±1.07)
$V_{Mesangium}(\times 10^4\ \mu m^3)$	3.68 (±1.47)	21.9 (±11.7)	3.33 (±2.91)
$V_{GBM}\ (\times 10^4\ \mu m^3)$	8.12 (±3.08)	14.8 (±6.84)	5.41(±3.68)
$V_{BCBM}\ (\times 10^4\ \mu m^3)$	5.20 (±1.71)	10.1 (±3.92)	5.52 (±3.93)
$V_{Nuclei}\ (\times 10^4\ \mu m^3)$	4.16 (±1.88)	9.19 (±3.95)	4.86 (±3.83)
$V_{bowman's\ Space}\ (\times 10^4\ \mu m^3)$	15.0 (±6.92)	8.97 (±7.28)	3.87 (±3.63)
$V_{renal\ Corpuscle}\ (\times 10^4\ \mu m^3)$	44.6 (±19.9)	79.8 (±33.3)	29.1 (±22.0)
% V_{Blood}	16.8 (±3.7)	10.0 (±1.9)	6.3 (±2.0)
% $V_{Mesangium}$	8.4 (±1.6)	26.1 (±5.2)	11.2 (±3.9)
% V_{GBM}	18.9 (±3.5)	18.3 (±1.8)	19.5 (±3.4)
% V_{BCBM}	12.3 (±2.6)	13.0 (±1.5)	22.2 (±7.6)
% V_{Nuclei}	9.2 (±2.2)	11.5 (±0.7)	15.7 (±3.1)
% $V_{Bowman's\ Space}$	34.1 (±7.9)	10.9 (±6.2)	12.9(±3.3)
$S_{BCBM}\ (\times 10^4\ \mu m^2)$	5.61 (±1.55)	20.5 (±22.3)	6.23 (±3.54)
$S_{GBM}\ (\times 10^4\ \mu m^2)$	11.8 (±4.82)	30.0 (±2.44)	7.83 (±4.81)
Total Cell Count	345 (±90)	423 (±87)	312 (±70)
GEnC Count	98 (±30)	152 (±53)	89 (±19)
MC Count	85 (±36)	133 (±44)	82 (±12)
Podocyte Count	99 (±21)	91 (±15)	46 (±31)
PEC Count	63 (±19)	46 (±2)	95 (±24)
GEnC%	28.2 (±3.5)	35.2 (±6.1)	28.8 (±1.3)
MC%	24.1 (±3.6)	31.0 (±5.4)	26.9 (±5.3)
Podocyte%	29.4 (±5.7)	22.5 (±7.1)	13.8 (±7.4)
PEC%	18.3 (±4.0)	11.3 (±2.4)	30.5 (±5.0)
Nuclear $V_{GEnCs}\ (\mu m^3)$	100.2 (±38.3)	191.4 (±50.0)	112.8 (±74.7)
Nuclear $V_{MCs}\ (\mu m^3)$	105.0 (±42.8)	210.3 (±65.1)	113.3 (±74.0)
Nuclear $V_{Podocytes}\ (\mu m^3)$	129.2 (±50.3)	220.2 (±66.7)	164.2 (±118.0)
Nuclear $V_{PECs}\ (\mu m^3)$	166.5 (±81.3)	252.7 (±68.0)	176.5 (±123.7)

Supplementary Table 3.2.2 Collective measurements of individual glomerular structures and cell types. All volume and surface area measurements are presented in pre-expansion units.

	Adult																Aged		FSGS			
Glom	**1**	**2**	**3**	**4**	**5**	**6**	**7**	**8**	**9**	**10**	**11**	**12**	**13**	**14**	**15**	**16**	**1**	**2**	**3**	**1**	**2**	**3**	**4**	**5**
Sex	M	M	F	F	M	M	M	F	F	M	M	M	M	M	M	F	F	F	M	M	M	F	M	F
Mouse #	1	1	2	2	3	3	3	4	5	6	6	6	7	7	7	8	9	9	10	11	11	12	13	12
Age	6 m	6 m	10 m	10 m	6 m	6 m	6 m	2 m	4.5 m	4.5 m	4.5 m	4.5 m	4 m	4 m	4 m	3 m	29 m	29 m	27 m	3.5 m	3.5 m	3 m	3 m	3 m
Expansion Factor	4.0	4.0	3.7	3.6	3.9	3.9	3.9	3.3	4.0	3.8	3.9	3.9	3.9	3.9	3.9	3.6	3.5	3.5	3.7	4.0	3.9	3.1	3.5	3.1
V_{Blood} ($\times 10^4$ µm^3)	5.2	6.2	6.2	12.3	3.2	5.2	8.5	10.9	6.3	6.2	5.3	6.3	6.0	12.8	8.2	6.2	10.5	7.9	4.7	2.7	2.6	0.3	1.9	0.8
$V_{Mesangium}$ ($\times 10^4$ µm^3)	3.7	5.2	2.9	6.5	1.6	2.0	2.5	5.7	2.4	3.6	2.7	4.1	3.8	5.8	3.8	2.4	29.7	27.5	8.5	7.2	5.6	1.1	2.2	0.6
V_{GBM} ($\times 10^4$ µm^3)	7.4	7.6	6.5	12.8	4.7	3.8	7.6	12.1	5.7	9.0	7.0	8.2	7.5	15.9	6.9	7.1	16.6	20.5	7.2	9.3	7.9	1.2	6.9	1.8
V_{BCBM} ($\times 10^4$ µm^3)	6.3	5.4	3.9	7.8	3.7	3.3	4.3	6.8	3.5	4.6	3.9	5.4	3.8	8.8	7.2	4.3	13.4	11.3	5.8	10.6	8.8	2.1	3.7	2.4
V_{Nuclei} ($\times 10^4$ µm^3)	3.3	4.2	4.3	7.3	1.2	1.3	2.6	5.6	2.9	4.0	3.7	5.9	4.6	6.8	6.6	2.5	11.9	11.0	4.7	7.9	9.3	0.9	5.2	1.1
$V_{Bowman's\ Space}$ ($\times 10^4$ µm^3)	14.3	16.6	12.6	21.2	8.2	8.7	13.8	26.5	17.0	11.9	10.0	14.0	11.4	32.4	15.8	5.3	17.3	5.9	3.7	9.5	5.4	1.0	2.4	1.1
$V_{Renal\ Corpuscle}$ ($\times 10^4$ µm^3)	37.8	43.2	33.1	65.9	21.1	21.7	36.4	62.9	34.5	38.6	30.0	49.6	47.7	97.6	64.4	29.8	97.2	100.8	41.5	55.5	46.3	6.7	28.7	8.3
% V_{Blood}	13.7	14.5	18.7	18.7	15.2	24.1	23.3	17.3	18.1	16.2	17.7	12.6	12.6	13.1	12.7	20.9	10.9	7.9	11.4	4.9	5.6	4.9	6.6	9.6
% $V_{Mesangium}$	9.9	12.1	8.9	9.8	7.4	9.4	7.0	9.0	6.9	9.2	9.0	8.3	8.0	6.0	5.9	8.2	30.6	27.3	20.5	13.0	12.1	16.2	7.7	7.0
% V_{GBM}	19.7	17.6	19.5	19.5	22.5	17.7	20.9	19.2	16.4	23.3	23.4	16.6	15.8	16.3	10.8	24.0	17.1	20.3	17.4	16.7	17.1	17.3	23.9	22.4
% V_{BCBM}	16.8	12.6	11.8	11.8	17.4	15.3	12.0	10.9	10.3	12.0	12.9	10.8	7.9	9.0	10.8	14.3	13.8	11.2	13.9	19.2	19.0	31.5	13.0	28.6
% V_{Nuclei}	8.6	9.6	12.9	11.0	5.8	5.8	7.0	8.9	8.3	10.3	12.5	11.8	9.6	7.0	10.2	8.4	12.3	10.9	11.2	14.2	20.0	12.9	18.0	13.5
% $V_{Bowman's\ Space}$	37.9	38.3	38.1	32.1	38.7	39.9	37.9	42.2	49.3	30.9	33.4	28.3	23.8	33.2	24.6	17.7	17.8	5.8	9.0	17.2	11.6	14.6	8.5	12.9
$S_{Capsule}$ ($\times 10^4$ µm^2)	5.0	5.6	4.7	7.4	3.7	3.8	4.8	7.3	4.7	5.3	4.6	6.0	5.6	9.3	7.5	4.4	46.1	9.7	5.7	11.3	7.8	2.6	6.2	3.3
S_{GBM} ($\times 10^4$ µm^2)	10.8	10.6	11.2	18.2	6.4	6.6	9.8	13.5	8.4	9.3	9.2	14.1	11.8	26.3	12.2	11.0	21.9	22.1	10.5	10.9	11.4	2.2	11.7	2.9
Total Cell Count	282	264	294	378	291	234	301	312	310	383	317	466	317	572	322	479	479	467	322	333	395	246	353	232
GEnC Count	67	66	86	140	76	57	77	98	102	108	93	139	87	159	82	135	180	186	91	101	111	73	95	67
MC Count	63	70	74	94	66	55	62	73	63	88	66	101	68	191	80	146	178	130	90	71	98	85	84	70
Podocyte Count	105	86	92	89	102	86	88	87	54	112	100	152	108	129	90	103	75	103	96	36	71	19	87	18
PEC Count	47	42	42	55	47	36	74	54	91	75	58	74	54	93	70	95	46	48	45	125	115	69	87	77
GEnC %	24	25	29	37	26	24	26	31	33	28	29	30	27	28	25	28	38	40	28	30	28	30	26.9	28.9
MC%	22	27	25	25	23	24	21	23	20	23	21	22	21	33	25	30	37	28	28	21	25	35	23.8	30.2
Podocyte%	37	33	31	24	35	37	29	28	17	29	32	33	34	23	28	22	16	22	30	11	18	8	24.6	7.8
PEC%	17	16	14	15	16	15	25	17	29	20	18	16	17	16	22	20	10	10	14	38	29	28	24.6	33.2
Nuclear V_{GEnCs} (µm^3)	93.3	138.9	125.9	160.5	32.4	48.0	74.4	152.2	81.8	86.8	98.0	106.6	116.9	104.9	137.7	44.1	221.4	219.2	133.7	166.0	199.5	27.9	125.6	45.0
Nuclear V_{MCs} (µm^3)	98.8	133.5	131.3	179.4	31.2	44.9	69.4	160.7	85.8	91.6	110.2	114.0	123.7	102.5	156.1	47.0	248.2	247.5	135.1	180.8	181.2	26.7	133.9	44.0
Nuclear $V_{Podocytes}$ (µm^3)	118.8	157.6	154.1	209.4	47.7	56.2	90.0	184.2	168.9	96.1	119.0	123.6	146.6	134.3	202.3	58.7	281.4	230.1	149.1	292.7	282.1	47.7	139.7	58.9
Nuclear V_{PECs} (µm^3)	162.8	227.2	189.7	269.1	61.7	71.2	103.1	243.0	64.2	152.9	156.0	181.9	213.7	159.6	342.0	65.0	308.5	272.7	177.0	308.5	285.2	48.8	188.1	51.8

Supplementary Table 3.2.3. Validation result for classification of glomerular cell type. Precision = (True positive)/(True positive + false positive). Recall = (True positive)/(True positive + False negative).

	Glomerular Endothelial Cell	Mesangial Cell	Podocyte	Parietal Epithelial Cell
True Positive	**192**	**139**	**127**	**130**
False Positive	**17**	**11**	**2**	**1**
False Negative	**18**	**0**	**11**	**2**
Precision	**91.9%**	**92.7%**	**98.4%**	**99.2%**
Recall	**91.4%**	**100.0%**	**92.0%**	**98.5%**
F1 Score	**0.916**	**.962**	**0.951**	**0.988**

3.3 Supplementary Movies

Supplementary Movie 3.3.1. *Image stack data (first half of movie) and segmented rendering (second half of movie) for the same adult glomerulus as shown in Figure 2.2a. Some white colors in segmented nuclei are due to the overlap between yellow (nuclei) and cyan (mesangium). Scale bars: 20 µm in pre-expansion units.*

Supplementary Movie 3.3.2. *Image stack data (first half of movie) and segmented rendering (second half of movie) for the same aged glomerulus as shown in Figure 2.2b. Some white colors in segmented nuclei are due to the overlap between yellow (nuclei) and cyan (mesangium). Scale bars: 20 µm in pre-expansion units.*

Supplementary Movie 3.3.3. *Image stack data (first half of movie) and segmented rendering (second half of movie) for the same D14 FSGS glomerulus as shown in Figure 2.2c. Some white colors in segmented nuclei are due to the overlap between yellow (nuclei) and cyan (mesangium). Scale bars: 20 µm in pre-expansion units.*

Supplementary Movie 3.3.4. *3D view of the same reconstructed nuclei of individual cell types and corresponding glomerular compartments as shown in Figure 2.5a. Note that the efferent arteriole exceeds the field of view and was partly truncated. Scale bars: 20 µm in pre-expansion units.*

3.4 Supplementary Methods

3.4.1 Mouse tissue

C57BL/6 mice were used for healthy, aged, and D14 FSGS mouse models. Aged mice from 27-29 m.o. (~75+ years old human) were acquired from the National Institute of Aging. For the podocyte depletion FSGS model, mice were given 2 consecutive doses of anti-podocyte antibody at 10mg/20gbw and euthanized after 14 days. Anesthetized adult mice were cardiac perfused with PBS/Azide (phosphate buffered saline containing 3 mM sodium azide) and 4% paraformaldehyde (PFA), each for 4.5 minutes. Both kidneys were harvested, and the renal capsules were removed. Each kidney was then fixed in 10 ml of the 4% PBS/PFA solution for 1 hour. All animal protocols (4442-01, 2968-04) were approved by the University of Washington Institutional Animal Care and Use Committee (IACUC). After fixation, the kidney was embedded in 4% (w/v) agarose in 1× PBS/Azide and then sliced into 100 μm sections using a vibratome.

3.4.2 Reagents

Reagents for hydrogel polymerization, based on the Magnified Analyais of the Proteome (MAP)[1] hydrogel protocol for polymerization, were purchased as follows: 40% (w/v) acrylamide (AA; Bio-Rad Laboratories, cat. no. 161-0140), 2% (w/v) bis-acrylamide (BA; Bio-Rad Laboratories, cat. no. 161-0142), Sodium acrylate (SA; Sigma-Aldrich, cat. no. 408220), VA-044 (Thermo Fisher Scientific, cat. no. NC0471397), bovine serum albumin (BSA; Rockland Immunochemicals Inc, item no. BAS-50). Reagents for denaturation were purchased as follows: Sodium dodecyl sulfate (SDS; Sigma-Aldrich, cat. no. L3771), Tris base (Tris; Fisher Scientific, cat. no. BP152-500), Sodium chloride (NaCl; Fisher Scientific, cat. no. 271). Reagents for

FLARE staining were purchased as follows: 10× phosphate-buffered saline, pH 7.4 (PBS; Fisher Bioreagents, cat. no. L-5400), Sodium azide (NaN3; Fisher Scientific, cat. no. S227I), Sodium acetate, anhydrous (NaOAc; Fisher Scientific, cat. no. S209), 4-Morpholineethanesulfonic acid (MES; Sigma-Aldrich, cat. no. M8250), NaIO4 (Sigma-Aldrich, cat. no. 311448), Sodium cyanoborohydride ($NaCNBH_3$; Sigma-Aldrich, cat. no. 156159), ATTO-TEC GmbH, cat. no. AD565, ATTO 647N NHS ester (AT647N-NHS; Sigma-Aldrich, cat. no. 18373), ATTO 565 hydrazide (AT565-$NHNH_2$, Hoechst 33258 (Sigma-Aldrich, cat. no. B2883). Triton X100 (61-2754) and Poly-L-lysine (P8920) were purchased from Sigma-Aldrich. Primary antibodies were purchased as follows: Rabbit anti-Erg (Abcam Inc., cat. no. ab214341), Goat anti-integrin alpha-8 (Fisher Scientific, cat. no. PA5-47572), Rabbit anti-Wilms Tumor Protein antibody (Abcam Inc., cat. no. ab89901), Goat anti-podocalyxin (R&D Systems, cat. no. AF1556), Rabbit anti-Pax8 (Proteintech, cat. no. 10336-1-AP). Secondary antibodies and fluorophores were purchased as follows: Donkey anti-rabbit IgG (Jackson ImmunoResearch Lab Inc, cat. no. 711-005-152), Donkey anti-goat IgG (Jackson Immuno Research Lab Inc, cat. no. 705-005-147), ATTO 488 NHS ester (Millipore Sigma, cat. no. 41698-1MG-F), Alexa Fluor 568 NHS ester (Lumiprobe, cat. no. 44820).

3.4.3 Preparation of fluorophore-conjugated secondary antibodies

Fluorophores were conjugated to secondary antibodies in-lab by first mixing ~40 µl of unconjugated secondary antibodies at (~1.3 mg/ml), 10 µl of 1M sodium bicarbonate (~pH 9.3), and 3 µg of NHS dye from a dye stock in anhydrous DMSO (~2 µg/µl). The bioconjugation reaction was allowed to proceed for 5-10 min at room temperature. After the reaction, a NAP-5

size exclusion column (Fisher Scientific, cat. no. 45-000-152) was used for purification. The column was equilibrated with ~10 ml PBS. The reaction mixture was then loaded onto the column, followed by ~600 µl of PBS. Another 300 µl of PBS was then added to the column, and the eluent was collected. The eluent absorbance was measured by UV/Vis absorption spectroscopy in order to determine the antibody concentration and dye-to-protein ratios (typically 200 µg/ml and 5-8 dye per antibody).

3.4.4 Immunostaining of kidney tissue samples

100 µm thick mouse tissue sections were immunostained using the following protocol. Tissue sections were first incubated in blocking/permeabilization buffer (3% BSA and 0.1% Triton X100 in PBS) overnight at 4°C. The sections were then incubated with primary antibodies at 3 µg/ml diluted in blocking/permeabilization buffer overnight at 4°C. The sections were then washed with blocking/permeabilization buffer three times at room temperature, 10 min each. The sections were then incubated with fluorophore-conjugated secondary antibodies at 5 µg/ml diluted in blocking/permeabilization buffer overnight at 4°C. The sections were then washed with blocking/permeabilization buffer three times at room temperature, 10 min each.

3.4.5 Kidney tissue gelation, denaturation, and expansion

100-150 µm thick kidney sections were first incubated in the MAP monomer solution [20% (w/w) AA, 10% (w/v) SA, 0.05% (w/w) BA, and 4% (v/v) PFA] for 24 hours at 4ºC. The section was then placed on a rectangular #1.5 coverslip and gently spread flat using a paintbrush.

Two stacked smaller pieces of #1.5 coverslips were placed on either end of the sample to act as spacers. A gelation solution was prepared by mixing 99 µl of pre-warmed MAP monomer solution with 1 µl of 10% (w/v) VA-44. A drop of the gelation solution (10-15 µl) was pipetted onto the tissue surface and covered with another piece of rectangular #1.5 coverslip to create a gelation chamber. The gelation chamber is then placed into a glass chamber and purged with sufficient nitrogen gas before closing the lid. Gelation was conducted for 2-2.5 hours at 45ºC. After gelation, the gel is peeled off and placed in a scintillation vial containing denaturation solution [200 mM SDS, 200 mM NaCl, 50 mM Tris]. The denaturation was performed at 70ºC for 18-24 hours and 95ºC for another 18-24 hours. The gel was washed with PBST solution three times, 30 minutes each, and one more wash with 1× PBS/Azide for another 30 minutes.

3.4.6 FLARE staining protocol

Gelled tissue samples were stained in the order of carbohydrates, amines, and DNA. Gelled and denatured samples were first oxidized with 2 ml of 20 mM $NaIO_4$ in NaOAc/NaCl buffer for 1 hour at 37ºC, protected from light with constant shaking, followed by three washes with NaOAc buffer for 10 minutes each. After oxidation, samples were then reacted in 1 mL of 5 µg/mL AT565-Hydrazide in NaOAc for 3 hours at room temperature. The samples were finally reduced by the addition of 20 µl of 5 M NaCNBH4 in NaOAc buffer for 30 minutes at room temperature. For staining amines, the samples were incubated with 2 ml of 5 µg/ml AT647N-NHS in MES buffer at pH 6 for 6 hours at room temperature. For DNA labeling, samples were stained with 1 mL of 5 µg/ml Hoechst 33258 in 1× PBS for 45 minutes at room temperature, followed by sufficient washes with 1× PBS. All the above procedures were

performed under the protection of light with constant shaking. Lastly, the samples were placed in a large quantity of deionized water for complete expansion overnight.

3.4.7 Fluorescence image acquisition

The MAP-FLARE sample was fixed onto a poly-lysine-coated cover glass to prevent drifting during imaging. Next, the sample was imaged using a scanning confocal microscope (Nikon A1R HD25 laser scanning confocal microscope) at the University of Washington Biology Imaging Center. A 40× water immersion objective lens (Apochromat Lambda S LWD 40× water, NA 1.15, WD 0.59–0.61 mm) was used and ~0.7 μm z-steps were taken for the 3-dimensional stack with concurrent measurements of the three FLARE labels. There are roughly 12,000 glomeruli within a mouse kidney[2,3], however, only 3-5 whole, intact glomeruli were accessible per 100 μm kidney section due to both the working distance of the objective and positioning of the glomeruli within the tissue sections. As a result, a compromise on the resolution had to be taken considering the imaging time and the working distance of the objective. The ~300 nm physical lateral resolution of the objective lens coupled with ~4× physical expansion could in principle achieve ~75 nm effective spatial resolution, but due to limitations of the number of pixels accessible to the fast galvo system on the confocal microscope, we opted to use a ~200 nm lateral physical pixel size that could achieve a sufficiently large field of view to capture whole glomeruli. The lateral pixel size, when accounting for ~4× physical expansion, corresponds to ~50 nm pixels in pre-expansion units and achieves an overall Nyquist-limited lateral resolution of ~100 nm. The axial step size of ~700 nm also slightly undersamples the ~1.2 μm physical axial resolution of the objective lens, and together with the ~4× physical expansion achieved an overall axial spatial resolution of ~350 nm. Together, these settings enabled 3-channel detection within a ~1 hour period.

3.4.8 Manual glomerular segmentation

Structure segmentation and identification were all done using ImageJ software using the following methods:

1) Full three-channel FLARE-stained raw data stacks were first split into carbohydrate, amine, and DNA as separate stacks. The noise from the carbohydrate stack was first cleaned up using *Process->Filters->Gaussian Blur 3D* with a sigma of 3. For noisier data sets, a 3D median filter was instead applied using *Process->Filters->Median 3D* with a radius of 3-5 in all directions. These filtering steps eliminated "salt & pepper" noise but retained most of the signal on the capsule. The resulting stack was then binarized using *Process->Binary->Make Binary*. For the binary method, using either "Li" or "mean" gave the best result in keeping most of the capsule signal while minimizing other signals.

2) Careful manual corrections were done along the BCBM to connect disconnected bits along the BCBM using the *Paintbrush Tool*. After correction, the *Paintbrush* tool was then used to erase all the other signals aside from the capsule.

3) The GBM was segmented using the same strategy as the BCBM.

4) Nuclei were segmented by manually tracing all the cell nuclei periphery in the DNA stack using the *Paintbrush* tool and then filled using the *Process->Binary->Fill Holes* tool.

5) The blood space was identified by first filling the segmented GBM using the *Process->Binary->Fill Holes* tool. Then the segmented GBM, nuclei,, and binarized amine channel were subtracted from the filled GBM using the *Process->Image Calculator* tool.

6) Bowman's space was identified by first filling the segmented BCBM using the *Process->Binary->Fill Holes* tool. Then the segmented GBM, BCBM, nuclei, blood space, and binarized amine channel were subtracted from the filled BCBM using *Process->Image Calculator* tool.

7) Lastly, the mesangium was segmented by filling the GBM using the *Process->Binary->Fill Holes* tool. Segmented GBM, blood space, and glomerular endothelial cells were then subtracted from the filled GBM result, using the *Process->Image Calculator* tool.

3.4.9 Semi-automated glomerular segmentation

Initially, we manually segmented five glomeruli as described above. These segmented structures are used as the foundation for training a neural network model.

Using the relatively small set of manually segmented data, we trained a neural network model to assist with the segmentation of structures in additional glomeruli. Although this did not produce a fully automated algorithm for glomerulus segmentation, it significantly reduced the human time required.

To segment the GBM and BCBM, we employed the cascaded nn-UNet 3D framework[4]. This framework consists of two main stages: 3DCNN_lowres and 3DCNN_fullres, which work together to perform both global-level and fine-grained segmentation. 3DCNN_lowres processes the glomerulus at a downsampled resolution to capture global contextual information and outputs

a coarse segmentation mask for further refinement. It is particularly effective at segmenting the GBM and BCBM due to its ability to provide coarse segmentation masks while reducing computational complexity. To refine the coarse segmentation, the 3DCNN_fullrest network operates at full resolution, using the original image along with the upsampled coarse masks. This step ensures that local details are captured (that may have been lost during first step downsampling) and is used to generate the final segmentation predictions. Both networks are based on an encoder-decoder architecture with residual connections[5] and skip connections[6], improving the flow of information through the network and increasing training efficiency. Each network was trained using a combination of cross-entropy loss and Dice loss[7], which optimizes segmentation accuracy by combining voxel-wise classification and overlap-based metrics.

For training, we used the first 5 manually segmented glomerular volumes and trained both networks for 20 epochs, with a batch size of 2. Z-score normalization and pixel-spacing-based downsampling were used as preprocessing steps. The training time was less than 1 hour for 3DCNN_lowres and around 12 hours for 3DCNN_fullres on a 16GB NVIDIA A6000 GPU. After training, the raw glomerulus volume was downsampled and fed into the 3DCNN_lowres model to get the downsampled approximate mask. Then, the approximate mask was upsampled and combined with the raw volume before being fed into the 3DCNN_fullres network to get the final prediction. The code for the training and segmentation model is available at the Zenodo repository (https://doi.org/10.5281/zenodo.13989435)

The overall prediction process for each raw glomerulus data set is less than 30 minutes, and the post-prediction manual refinement took 2-3 days per glomerulus, on average, which is

much less than the original approximate 4 weeks for complete manual segmentation for a glomerulus.

The trained neural network model produced initial predictions with three channels: GBM, BCBM, and nuclei. To ensure the accuracy of these predictions, we manually reviewed and corrected the results for any discrepancies or errors using the manual methods described.

For the segmentation of the remaining glomerular structures—namely, blood space, Bowman's space, and the mesangium- we employed the same manual segmentation methods above.

3.4.10 Glomerular structures reconstruction and analysis

The segmented results were reconstructed using Imaris (RRID: SCR_007370). For specific instructions on the surface creation tool, see the Imaris Reference Manual (https://imaris.oxinst.com/).

3.4.11 Pre- & post-expansion image registration

Correlative registration of pre-expansion immunostain and post-expansion FLARE samples was performed as described previously using Elastix[8]. Briefly, the nuclear channels of pre- and post-expansion images of the same glomerulus were first roughly aligned using a rigid linear similarity transformation. The same transformation parameters were then applied to the post-expansion carbohydrate and amine channels of the same stack. Next, a non-rigid B-spline

transformation was applied to the post-expansion image to match the pre-expansion image. Again, the same transformation parameters were then applied to the other two channels in order to produce a single composite of the pre-expansion immunostains and the post-expansion FLARE signal.

3.4.12 Data reporting

ARRIVE reporting guidelines were followed for all experimental design, data reporting, as well as discussion[9].

3.4.13 Cell type validation

To validate glomerular cell type classification, mouse kidney sections were first immunostained against markers for each individual cell type using the immunostain protocol listed above. An overall map of the stains was imaged using a confocal microscope at ~1.7 μm resolution. Several glomeruli per cell type were imaged at ~0.2 μm resolution, and their positions within the map were noted. The stained and imaged sections were subsequently processed with expansion microscopy and FLARE staining (which bleaches the immunostain fluorophores). The same glomeruli were located on the expanded and FLARE-stained samples and then imaged by confocal microscopy at high spatial resolution (e.g., 100 nm effective lateral spatial resolution). Pre- & post-ExM images were registered as described above. During cell-type validation data analysis, cell types were first assigned manually by only looking at post-ExM FLARE-stained images. These assigned cell types were then validated using the pre-ExM cell-specific immunostains to evaluate the precision and recall of the classification.

Precision and recall are defined as below:

	Immunostain	FLARE
True + (TP)	o	o
False + (FP)	×	o
False – (FN)	o	×

	Precision	Recall
Definition	Of all predicted positives (using FLARE), how many are really positive (using immunostain)	Of all real positive cases (using immunostain), how many are predicted positive (using FLARE)
Mathematical Definition	$\frac{TP}{TP + FP}$	$\frac{TP}{TP + FN}$

3.4.14 Basement membrane thickness analysis

Basement membrane thickness was measured using a custom MATLAB script (https://doi.org/10.5281/zenodo.13146131). In general, segmented masks were first scaled to ensure isotropic voxels. These scaled masks were used to generate surface normal vectors for each vertex. A line centered at each vertex was used to measure the intensity profile of the raw image stack along the direction of the corresponding surface normal vector. A Gaussian function was fitted to each intensity profile, and the thickness was estimated from the FWHM of the fitted Gaussian curve. For the GBM, measurements were restricted to regions of the GBM that are in contact with capillary loops and Bowman's space only. Additionally, we limited our analysis to regions of the GBM where the surface normal vectors were oriented approximately within the xy-plane (i.e., BM surface normal vectors having an angle of 80-90 degrees with respect to the z-axis). This selection ensured that the GBM, which is ≥200 nm thick, would only be measured along the lateral dimensions where the effective resolution of ~100 nm would not appreciably

broaden the measurement. Due to anisotropy in the microscope's point spread function, the effective spatial resolution can be as high as ~350 nm along the axial dimension (**Supplementary Figure S7**). While this orientation criterion excluded parts of the GBM, the large sample size of over 40,000 data points per sample nonetheless covers regions across the entire glomerulus.

3.5 Supplementary References

1. Ku T, Swaney J, Park JY, et al. Multiplexed and scalable super-resolution imaging of three-dimensional protein localization in size-adjustable tissues. *Nature Biotechnology*. 2016;34:973-981. doi:10.1038/nbt.3641
2. Baldelomar EJ, Charlton JR, deRonde KA, Bennett KM. In vivo measurements of kidney glomerular number and size in healthy and Os/+ mice using MRI. *American Journal of Physiology-Renal Physiology*. 2019;317(4):F865-F873. doi:10.1152/ajprenal.00078.2019
3. Hann BD, Baldelomar EJ, Charlton JR, Bennett KM. Measuring the intrarenal distribution of glomerular volumes from histological sections. *Am J Physiol Renal Physiol*. 2016;310(11):F1328-1336. doi:10.1152/ajprenal.00382.2015
4. Isensee F, Jaeger PF, Kohl SAA, Petersen J, Maier-Hein KH. nnU-Net: a self-configuring method for deep learning-based biomedical image segmentation. *Nat Methods*. 2021;18(2):203-211. doi:10.1038/s41592-020-01008-z
5. He K, Zhang X, Ren S, Sun J. Deep Residual Learning for Image Recognition. Published online December 10, 2015. doi:10.48550/arXiv.1512.03385
6. Ronneberger O, Fischer P, Brox T. U-Net: Convolutional Networks for Biomedical Image Segmentation. Published online May 18, 2015. Accessed September 23, 2024. http://arxiv.org/abs/1505.04597
7. Sudre CH, Li W, Vercauteren T, Ourselin S, Cardoso MJ. Generalised Dice overlap as a deep learning loss function for highly unbalanced segmentations. Published online July 14, 2017. doi:10.48550/arXiv.1707.03237
8. Chozinski TJ, Halpern AR, Okawa H, et al. Expansion microscopy with conventional antibodies and fluorescent proteins. *Nature Methods*. 2016;13(6):485-488. doi:10.1038/nmeth.3833
9. Sert NP du, Hurst V, Ahluwalia A, et al. The ARRIVE guidelines 2.0: Updated guidelines for reporting animal research. *British Journal of Pharmacology*. 2020;177(16):3617. doi:10.1111/bph.15193

Chapter 4

4.1 Conclusion and future directions

In this dissertation, I have presented a novel pipeline called GloMAP for super-resolution, 3D imaging, reconstruction, and quantitative analysis of the whole mouse renal glomeruli. This method enables whole-glomerulus analysis at nanoscale resolution and overcomes the limitations in kidney research from relying on thin 2D sections or partial 3D reconstructions. By capturing the glomerulus as a whole functional unit, my pipeline allows for insights into the structural complexity and spatial relationships among glomerular compartments and cell types under physiological and pathological conditions.

A major strength of GloMAP lies in its versatility and accessibility. GloMAP integrates chemical tissue labeling, expansion microscopy, computational segmentation, and reconstruction to generate super-resolution 3D datasets without the need for specialized super-resolution microscopes. The quantitative pipeline developed here, such as volumetric mapping of compartments, cell type classification, and global morphometric analysis in various conditions, offer a foundation for detailed investigation of glomerular structure and its alterations in disease.

Looking forward, this work set the stage for several important future directions:

- **Global structural vs. functional correlation**: The ability to reconstruct and quantify entire glomeruli in 3D opens up opportunities to study how structural components (such as capillary loops, basement membranes, and podocytes) relate to each other across the entire glomerulus. Such global perspectives could reveal organizational patterns, spatial coordination, and progression of pathological changes that are undetectable in

conventional 2D or partial reconstruction methods.

- **Refinement of machine learning models**: The segmentation process, which currently takes 3 days of effort per glomerulus, can be further optimized by refining the neural network model parameters used to predict glomerular structures. Enhancing model performance to achieve more efficient and reliable segmentation outcome with less human supervision would significantly improve scalability and reproducibility. In turn, the method would be much more impactful.

- **Biophysical modeling and simulation**: With accurate 3D reconstructions of capillary networks and surrounding compartments, it becomes possible to use these models to simulate fluid dynamics across the glomerulus. Such modeling could help us better understand how local structural changes affect hemodynamics and filtration efficiency, providing a deeper understanding of glomerular filtration physiology.

- **Correlative basement membrane molecular mapping**: By integrating immunolabeling of GBM-related proteins, one can correlate regional thickness patterns with local protein compositions and organizations. This could shed light on whether structural changes such as GBM thickening are associated with the accumulation or absence of certain proteins, providing insights into disease progression.

- **Morphometry-driven automatic cell classification**: The rich dataset of cell type morphometric features, such as size, shape, and spatial orientation, offers the potential to train new classification models that rely solely on nuclear staining. Such models could enable accurate, automated identification of glomerular cell types in datasets where only a general nuclear stain is available.

- **Translation to synthetic and regenerative systems**: The detailed reconstructions generated in this study can provide a reliable foundation for the design of bioprinted glomeruli or synthetic filtration systems by serving as a realistic structural baseline. These applications could have significant impacts in kidney tissue engineering.

Importantly, the full datasets, including the raw data, segmented labels, as well as reconstructed 3D models, and computational scripts developed during this project ,have been made freely available online to the research community. By sharing this resource, I hope to promote reproducibility, accelerate discovery, and enable others in the field to build upon this work to further advance the field of nephrology.

In conclusion, this thesis not only provides a powerful imaging and analysis pipeline but also builds the foundation for future studies that explore the glomerulus as a dynamic and integrated system. Through continued refinement and application, these tools have the potential to transform our understanding of kidney biology and disease.

Appendix: Publications and Presentations

This appendix highlights my academic accomplishments beyond the main research chapters presented in this dissertation. It includes a list of peer-reviewed publications as well as manuscripts currently in review or preparation, along with a brief summary of my main role and my contribution to each of them. Additionally, it includes an invited oral presentation delivered at a national conference, where I shared my dissertation work with the broader nephrology research community.

These accomplishments demonstrate my active engagement in disseminating research through both written and oral scientific communication and reflect my broader involvement in the scientific community throughout my PhD career.

Publications in Revision/Preparation

1. **Ali, A**., Liu, Z., Ye, K., Guan, Y., Chen, S., Liu, T., *et al.* *Nanoscale Optical Imaging, Reconstruction, and Spatial Analysis of Whole Mouse Glomeruli. Kidney International* [In Revision].
    - Presented in earlier chapters

2. Brenes, D., Han, Q., Bishop, K., **Ali, A**., et al. *An open-top light-sheet (OTLS) microscope for ultra-high-resolution imaging with gel-based tissue expansion* [In Preparation]
    - Prepared expanded mouse and human samples for large volume light sheet microscopy imaging.

- Performed width measurements for podocytes' foot processes to highlight the resolution of the new lightsheet microscopy system

Peer-Reviewed Publications

3. Kaverina, N., Schweickart, R.A., Chan, G.C., Maggiore, J.C., Eng, D.G., Zeng, Y., **Ali, A**., *et al. Inhibiting NLRP3 Signaling in Aging Podocytes Improves Their Life- and Health-Span. Aging*, 2023.
    - Measured basement membrane thickness, podocyte foot processes width and periodicity using super-resolution volumetric images of mouse glomerulus.
    - Quantitatively compared these measurements among young, mid-aged, and treated mouse samples.

4. Lee, M.Y., Mao, C., Glaser, A.K., **Ali, A**., *et al. Fluorescent Labeling of Abundant Reactive Entities (FLARE) for Cleared-Tissue and Super-Resolution Microscopy. Nature Protocols*, 2022.
    - Tested the fluorescent retention time for carbohydrate labeling using oxidized carbohydrate and hydrazide-functionalized fluorophore.
    - Developed alternative carbohydrate labeling chemistry that required no toxic reduction agents

5. Rahmati, M., Stötzel, S., El Khassawna, T., Mao, C., **Ali, A**., *et al. Intrinsically Disordered Peptides Enhance Regenerative Capacities of Bone Composite Xenografts. Materials Today*, 2022.

- Validated the effect of proline-rich disordered peptides on bio-mineralization of bones,
- Observed that carbohydrates are rich in mineralized regions and proteins are rich in non-mineralized regions.

Conference Presentations

- **Kidney Week, American Society of Nephrology, Philadelphia, PA, November 1–5, 2023**

  Oral presentation: *"Nanoscale Optical Imaging, Reconstruction, and Spatial Analysis of Whole Mouse Glomeruli"* Delivered in front of leading international experts in nephrology.